RECONSTRUCTION OF THE ELECTRON DISTRIBUTION FUNCTION DURING ECRH/ECCD AND MAGNETIC RECONNECTION EVENTS IN A TOKAMAK PLASMA

THÈSE N^{O} 3432 (2005)

PRÉSENTÉE À LA FACULTÉ SCIENCES DE BASE

CRPP Association Euratom

SECTION DE PHYSIQUE

ÉCOLE POLYTECHNIQUE FÉDÉRALE DE LAUSANNE

POUR L'OBTENTION DU GRADE DE DOCTEUR ÈS SCIENCES

PAR

Igor KLIMANOV

ingénieur-physicien, Institut National d'Ingénierie et de Physique, Moscou, Russie
et de nationalité russe

acceptée sur proposition du jury:

Prof. A. Fasoli, directeur de thèse
Prof. R. Chawla, rapporteur
Dr E. De La Luna, rapporteur
Dr T. P. Goodman, rapporteur
Dr P. V. Savrukhin, rapporteur

Lausanne, EPFL
2006

Version abrégée

Les performances d'un tokamak sont habituellement décrites en termes de température, densité et temps de confinement du plasma. La notion de température implique que le plasma est à l'équilibre thermique et ses particules possèdent une distribution Maxwellienne (normale) des vitesses. Cependant, sous certaines conditions, le nombre de particules dont l'énergie cinétique vaut plusieurs fois l'énergie cinétique moyenne du plasma peut largement excéder celui que l'on aurait dans le cas d'une distribution Maxwellienne des vitesses. Ces particules de haute énergie cinétique sont appelées particules rapides. Au cours de cette thèse les différents méchanismes de production et les propriétés des électrons rapides observés dans le Tokamak à Configuration Variable (TCV) de Lausanne ont été analysés.

Cette thèse est constituée de trois parties. La première partie décrit la conception, la construction et l'installation d'un radiomètre à 24 canaux permettant d'analyser l'Emission Cyclotronique Electronique (ECE). Ce nouveau radiomètre observe le plasma depuis le côté bas champ magnétique, dans la gamme de fréquences 65-100 GHz. Il complète ainsi les informations fournies par le radiomètre existant, qui observe le plasma depuis le côté haut champ, dans la gamme de fréquences 78-114 GHz. Les deux radiomètres ECE sont les diagnostiques principaux utilisés pour l'analyse des populations d'électrons rapides effectuée dans cette thèse.

Dans la deuxième partie, une méthode permettant de reconstruire la fonction de distribution des électrons, à partir de mesures de l'ECE effectuées depuis les côtés haut et bas champ, est exposée. La méthode est essentiellement basée sur un code numérique développé dans le cadre de cette thèse et permettant de simuler les signaux de l'ECE à partir d'une fonction de distribution définie numériquement. Le code utilise l'approximation WKB et calcule les signaux de l'ECE en résolvant l'équation du transport de rayonnement.

La troisième partie discute les données expérimentales obtenues sur TCV. L'existence d'une population d'électrons rapides permet d'expliquer quantitativement l'absorption inhabituellement élevée des ondes de chauffage cyclotronique électronique à 118 GHz, observée dans les régimes exploitant la génération de courant par ondes cyclotroniques électroniques. Globalement, l'énergie des électrons rapides ne représente que 2 % de l'énergie totale du

plasma.

Une analyse de la fonction de distribution pendant l'instabilité de dent de scie prouve que des électrons suprathermiques peuvent être produits dans des plasmas ohmiques, ainsi qu'en présence de chauffage et de génération de courant par ondes cyclotroniques électroniques. Dans les plasmas avec chauffage par ondes, les énergies et les densités typiques de la population d'électrons rapides créés pendant l'effondrement de dent de scie sont $E = 15 - 30$ keV et $n_{st} = 2 \cdot 10^{17}$ m^{-3}, respectivement. 30-40 % de l'énergie perdue pendant l'effondrement, l'est sous forme d'électrons rapides, ce qui montre que l'accélération des électrons est un mécanisme important pour la dissipation de l'énergie libérée pendant la reconnexion magnétique dans le plasma du tokamak. La dynamique des électrons rapides observée suggère une diffusion radiale élevée dans le plasma ($D_{st} = 25$ m^2/s) pendant et juste après l'effondrement des dents de scie, qui domine le processus de ralentissement classique, par collision, des électrons rapides avec le reste du plasma.

Abstract

The performance of tokamaks is usually described in terms of plasma temperature, density and confinement time. The term temperature implies that the plasma is in thermal equilibrium and its particles have maxwellian (normal) velocity distribution. However, in several conditions, the plasma contains a significant number of suprathermal or 'fast' particles, whose energy is several times higher than thermal energy. The number of such particles can be significantly higher than that corresponding to the maxwellian distribution. Such electrons produced by different acceleration mechanisms in the TCV tokamak have been analyzed in the course of this thesis.

This thesis consists of three parts. The first part describes the design, construction and implementation of a new 24-channel Electron Cyclotron Emission (ECE) radiometer, viewing the plasma from the Low Field Side (LFS) in the frequency range 65-100 GHz. The new LFS ECE radiometer, together with the existing 24-channel ECE radiometer viewing the plasma from the High Field Side (HFS) in the frequency range 78-114 GHz are the main diagnostics used in the analysis.

The second part includes the development of a numerical code to simulate the ECE signals. The code is based on the WKB approach and solves the equation of radiation transport to calculate ECE signals using a numerically defined Electron Distribution Function (EDF). A method to reconstruct EDF from HFS and LFS ECE, based on the ECE code, is presented.

The third part discusses the experimental data obtained on the TCV tokamak. In regimes with Electron Cyclotron Current Drive (ECCD), a quantitative explanation of the anomalously high absorption of the RF power at 118 GHz and a validation of the power balance analysis based on Thomson scattering measurements are provided. An analysis of the EDF during sawtooth instability shows that suprathermal electrons are generated in ohmic, Electron Cyclotron Heated (ECH) and ECCD plasmas. In ECH plasmas, typical energies and densities are found to be $E = 15-30$ keV and $n_{st} = 2 \cdot 10^{17}$ m^{-3}. This corresponds to 30-40 % of the energy lost during the crash, which proves that acceleration of electrons is an important mechanism for the dissipation of energy released during magnetic reconnection in a tokamak plasma. The observed fast electron dynamics suggests a high radial diffusion in the plasma during and just after the sawtooth crash ($D_{st} = 25$ m^2/s), which dominates over the classical slowing down process.

Contents

Chapter 1

Introduction

In this chapter we briefly define the main basic concept and physical quantities that are essential for this thesis work. For a detailed description, see for example [1], [2].

1.1 Plasma

The term plasma, introduced by Irving Langmuir in 1928, is usually used to describe an ionized gas with a high electric conductivity. A more strict definition implies the quasi-neutrality (total charge is zero) and that the Debye length λ_D is much shorter than the characteristic length scale of the system: $\lambda_D << L$. The Debye length for the plasma in a thermodynamic equilibrium can be calculated as follows:

$$\lambda_D = \sqrt{\frac{\epsilon_0 k_B / e^2}{n_e/T_e + \sum_{ij} j^2 n_{ij}/T_i}}, \tag{1.1}$$

where the index "e" denotes electrons, "ij" denoted ions of i species with a charge $j \cdot e$, n is the density and T is the temperature.

The Debye length corresponds to the distance at which charge separation can occur. The electric field arising from the charge separation prevent further increase of the distance. Another illustration to the Debye length is the situation, where a test charge is placed inside the plasma. The test charge would attract charges of opposite sign and therefore it would be shielded or screened from the rest of the plasma. The Debye length is the characteristic length for such screening. Therefore one can say that on a length scale larger

than Debye length the collective effects dominate the individual interactions between the particles.

In principle, the term plasma can be applied to overdense gases ($n > 10^{26}\mathrm{m}^{-3}$) or even to solid state materials, which contain free charge carriers, such as electrons in metals. In this case two more conditions should be verified: the collision frequency of the charged particles with neutrals should not dominate oscillations of the charged particles due to electromagnetic interactions and the number of particles in a sphere with a radius equal to Debye length should be significant, $N_D >> 1$.

In laboratory conditions, the plasma is typically obtained by heating the neutral gas under vacuum. The degree of ionization can be estimated using the Saha equation:

$$\frac{n_{i+1}n_e}{n_i} = \frac{2}{\Lambda^3}\frac{g_{i+1}}{g_i}exp\left(-\frac{\epsilon_{i+1}-\epsilon_i}{k_BT}\right) \tag{1.2}$$

where index "i" denotes the ionization level, $i = 0$ corresponds to a neutral atom. ϵ is the ionization potential, g is the degeneracy of states, Λ is the thermal de Broglie wavelength of an electron. Further in this thesis, when we refer to the term plasma, we mean high temperature plasma, i.e. $T >> \epsilon_1$, therefore a fully ionized plasma.

1.2 Thermonuclear fusion

One of the main applications of plasma physics and potentially the most important one is thermonuclear fusion. The goal is to release nuclear energy from the isotopes of hydrogen, one of which (deuterium) is contained in water, and the other one (tritium) can be regenerated inside a thermonuclear reactor. Now with historically high oil prices of 70 $ per barrel it looks more attractive than ever.

$$D + T \rightarrow {}^4He + n + 17.6 \text{ MeV} \tag{1.3}$$

The D-T reaction 1.3 has been realized for the first time with a positive energy outcome in 1952 on a small island in the pacific ocean in a form of

massive explosion. In a half century this reaction has not been realized yet in a controlled way with a positive energy outcome.

In order to have a positive energy outcome, certain conditions have to be satisfied. First, to overcome the Coulomb force of repulsion between positively charged ions and reach the conditions that the produced power exceeds the radiation losses, the plasma temperature has to be very high, at least about 10 keV (∼100 millions °C) for the D-T reaction. Second, the plasma density and the confinement time τ have to be sufficiently high to ensure the possibility to extract energy in a form of heat or electricity. This is the Lawson criterion, which for D-T implies $n\tau > 10^{20}$ m^{-3}s.

There are two different approaches to meet the Lawson criterion. The first approach, somehow similar to the H-bomb experiments, is called inertial confinement. The idea is to heat a frozen D-T pellet target by a laser pulse or relativistic electron beam, and therefore to provoke a microexplosion. In this case we can have $n \sim 10^{32}$ m^{-3} and $\tau \sim 10^{-11}$ s.

The second approach is called magnetic confinement. The idea is to confine charged particles at required temperature by external magnetic fields, so that the fusion reactions can occur in a quasi steady-state regime. Then for the D-T reactions tritium can be regenerated during the operation via the reactions listed below.

$$
\begin{aligned}
D + D &\rightarrow \ {}^3He + n + 3.2 \text{ MeV} \\
D + D &\rightarrow \ T + p + 4.0 \text{ MeV} \\
n + {}^6Li &\rightarrow \ {}^4He + T + 4.8 \text{ MeV}
\end{aligned}
\tag{1.4}
$$

Magnetic confinement has received most attention in the past decades. Many types of magnetic confinement installations has been developed. The most successful are tokamaks, stellarators and pinches. In this case we can have $n \sim \ 10^{20}$ m^{-3} and $\tau \sim 1$ s.

To illustrate the energy capacity of the fusion power, we can give two comparisons. First, a modern H-bomb can be equivalent to one million bombs of

World War II. Second, one liter of water, normally containing only 0.015% of molecules with an atom of D instead of H, is energetically equivalent to 300 liters of gasoline.

1.3 Tokamak

The most successful type of installation for controlled magnetic fusion is the tokamak. The idea of tokamak has been proposed and realized for the first time in Russia (Soviet Union) in the early 1950s. A word "tokamak" was made up at that time, meaning "**TO**roidal **C**h**A**mber with **MA**gnetic **C**oils".

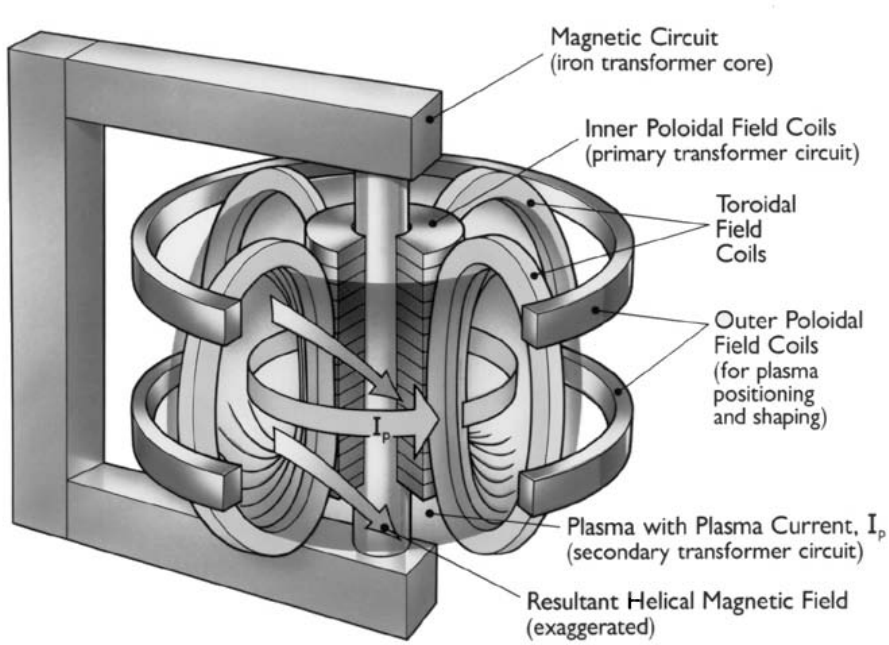

Figure 1.1: *Schematic view of a tokamak.*

The basic ideas behind the tokamak concept (fig. 1.1) can be summarized as follows. A toroidal vacuum tight chamber is surrounded by magnetic coils, providing toroidal magnetic field, preventing, in the first approximation, the radial movement of the charged particles. A transformer provides a change of magnetic flux, which creates a toroidal electric field and drives the current in the plasma.

The sum of the toroidal and poloidal (from the current) magnetic fields is the helical magnetic field. This creates closed magnetic flux surfaces and prevents the drift of the charged particles due to possible charge separation in the absence of the current. Outer poloidal field coils help stabilizing the plasma position and have influence on the plasma shape.

Here we define the safety factor q, a dimensionless quantity, which is widely used in the analysis of the stability of plasmas in tokamaks:

$$q = \frac{d\Phi_{tor}}{d\Phi_{pol}},$$

where Φ_{tor} is toroidal magnetic field flux and Φ_{pol} is the poloidal magnetic field flux.

The current driven by the transformer has many purposes. It creates the plasma in the first place. Than it heats the plasma, providing basic stability. And finally, it helps establishing regimes with a better stability and confinement [2].

1.4 Motivation and outline

Among the main issues in tokamak physics research are plasma confinement and stability, which depend on the plasma heating and current drive. While many experiments have been carried out since 1950 and many important effects have been discovered, empirical scaling laws still play a major role in predicting tokamak performance due to the lack of comprehensive physical models.

The main goal of this thesis is the study of the changes of the electron distribution function on the TCV tokamak. The changes can be caused by the auxiliary heating or by the spontaneous rearrangement of magnetic field structures, known as magnetic reconnection. In the former case a non-maxwellian distribution can exist in a steady-state regime, while in the latter the effect lasts only about 1 ms. The results of the analysis can be important for the physics of current drive or magnetic reconnection, neither of which are yet fully understood.

The study required the construction of a new Electron Cyclotron Emission (ECE) radiometer, which greatly enhanced the ECE diagnostics systems on

TCV. A development of a numerical code to simulate the ECE spectra, which is a key element in the analysis of the ECE data, has been necessary as well.

The thesis is structured as follows. A description of the TCV tokamak, on which the experiments have been performed, together with a description of the main diagnostics used in the analysis, is presented in Chapter 2. Basic elements of the theory of waves in plasma can be found in Chapter 3. The design, the construction of the new ECE radiometer, the tests, the calibrations and the measurements performed in various configurations on TCV are shown in Chapter 4. Chapter 5 describes the development of the ECE code, together with some elements of ECE theory and test examples. Chapters 6 and 7 contain the experimental results. While Chapter 6 is devoted to steady-state scenarios with strong auxiliary heating and current drive, Chapter 7 focuses on the fast changes of the distribution function caused by internal plasma relaxation events. Conclusions and outlook are presented in Chapter 8.

Chapter 2

TCV

2.1 The TCV tokamak

The TCV tokamak (Tokamak à Configuration Variable) is located in Lausanne at the Centre de Recherches en Physique des Plasmas (CRPP) of the Swiss Federal Institute of Technology (EPFL). It has a major radius $R = 0.88$ m, and a minor radius $a = 0.25$ m. The toroidal magnetic field is $B_{tor} < 1.5$ T, the plasma current is $I_p < 1$ MA. A drawing of the TCV tokamak is shown in fig. 2.1.

The design of TCV (highly elongated vessel, variety of poloidal field coils) has been motivated by its main goal, the study of the effects of the plasma shape on the tokamak performance. TCV allows the creation of plasmas with cross-section characterized by a high elongation ($\kappa \leq 3$) and triangularity ($-0.8 < \delta < 0.9$). Examples of different plasma shapes achieved on TCV are presented in fig. 2.2.

2.2 Diagnostics on TCV

TCV is equipped with many diagnostics, some of which are being upgraded. New diagnostics are under development. The TCV diagnostic suite includes the charge exchange recombination spectrometer (CXRS), the diamagnetic loops (DML), the Thomson scattering system (TS), the far infrared interferometer (FIR), the multi-wire proportional x-ray detectors (MPX), the hard x-ray spectrometer (HXR), the visible light spectrometer, the bolometers, the neutral particle analyzer, the diagnostic neutral beam injector (DNBI), electron cyclotron emission radiometers (ECE), magnetic probes, laser ablation, soft x-ray tomography system (X-TOMO), infrared camera (IR) and

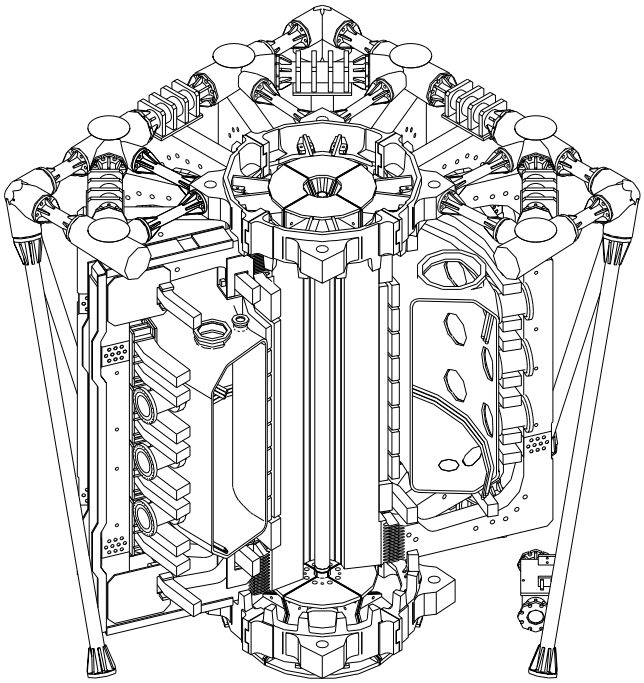

Figure 2.1: *Drawing of the TCV tokamak.*

Langmuir probes. A few diagnostic systems, which have been intensively used in this thesis, are described below.

2.2.1 Thomson Scattering

A laser beam that passes through the plasma interacts with the free plasma electrons, so that a small amount of the laser light is scattered. The spectral broadening due to the Doppler effect contains information on the electron temperature. The total intensity of the scattered radiation is proportional to the electron density.

On TCV, three Nd-Yag lasers (1.06μm) are used for the Thomson scattering. Each laser works at 20 Hz and provides 1J per pulse. There are three sets of wide angle lenses, which are installed on three different ports. This allows 25 chord measurements with a spatial resolution of 4 cm (fig. 2.3). Optical fibre bundles transfer the scattered light into polychromators with 3 or 4

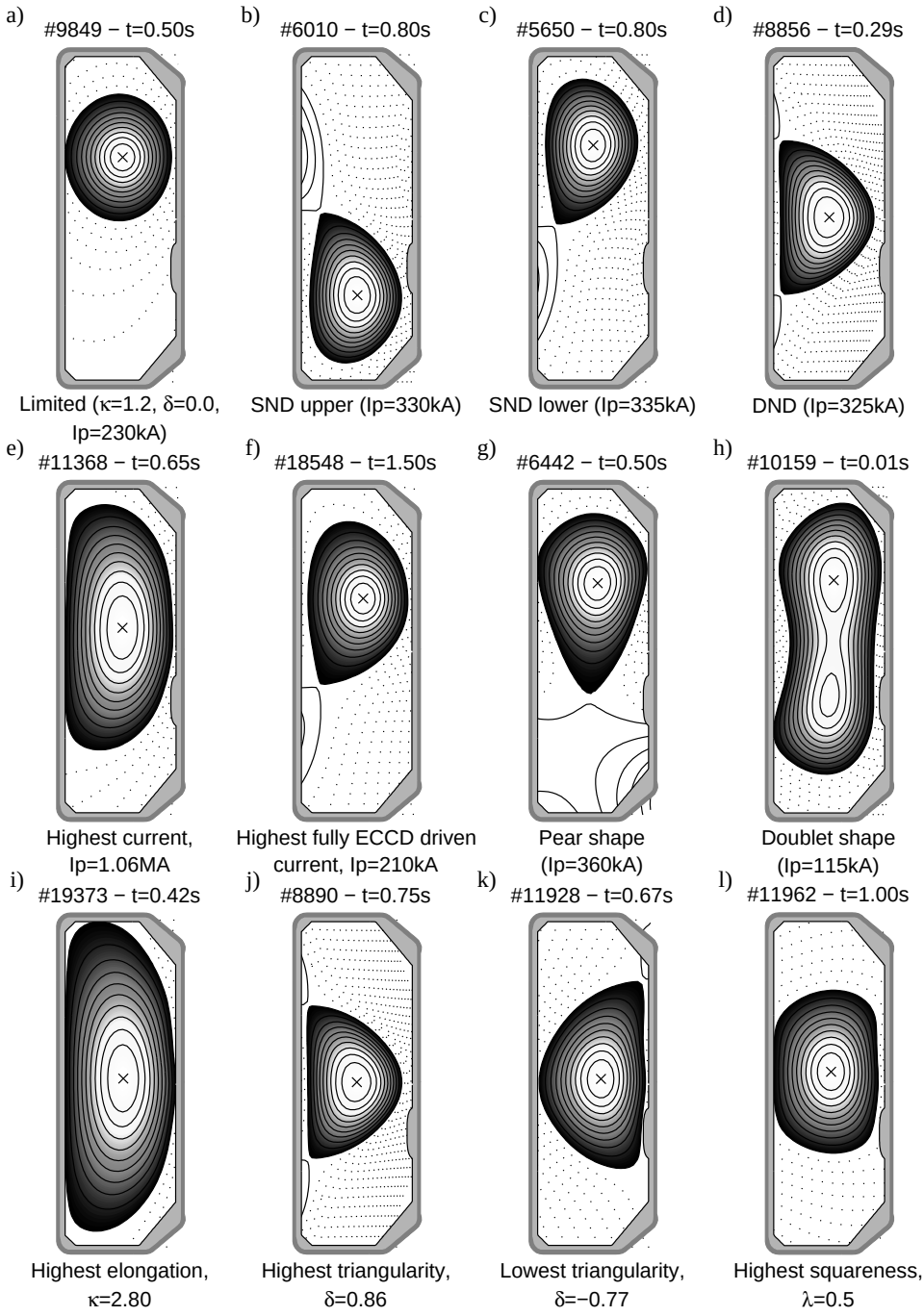

Figure 2.2: *Various plasma shapes realized on TCV.*

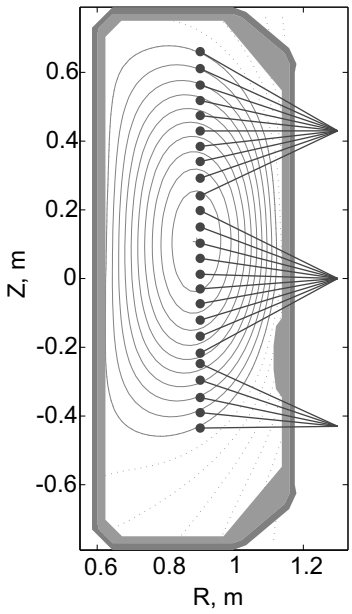

Figure 2.3: *The geometry of the Thomson scattering system.*

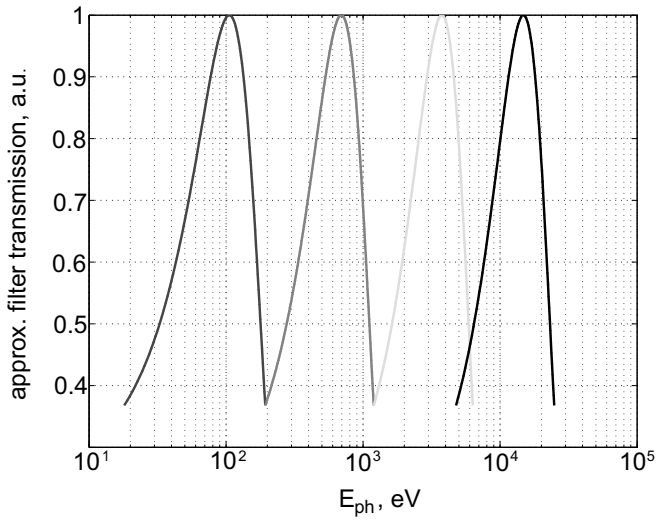

Figure 2.4: *Approximate photon energy transmission characteristics of the filters of the Thomson scattering system. Normally, photons, whose energy do not exceed 6 keV, define the temperature measured by the TS system.*

interference filters. Si-avalanche photodiodes finally measure the scattered light intensity.

Approximate photon energy transmission characteristics of the filters are shown in fig. 2.4. The electron temperature is normally obtained from the ratio between the pair of spectral channels with the highest signal. The fourth filter, despite the largest spectral width, is rarely used, because of the low number of photons scattered in the frequency range corresponding to the energies 5-12 keV. The system is absolutely calibrated using Raman scattering from neutral nitrogen introduced into the TCV vessel.

2.2.2 X-ray diagnostics

The intensity of the x-ray bremsstrahlung radiation from the plasma depends on the plasma density, temperature and impurities charge state: $I_{brem} \sim n_e^2 T_e^{1/2} Z^2$. Several soft x-ray diagnostic systems are installed on TCV. The main x-ray diagnostic is the tomography system, which consists of ten 20-channel pinhole cameras and provides a spatial resolution ~ 3 cm.

MPX

The most recent x-ray system, extensively used in the thesis, is the Multi-wire Proportional X-ray detector (MPX). MPX has 64 channels with a radial resolution of 5 mm and a frequency bandwidth of 50 kHz. The MPX geometry is shown in fig. 2.5.

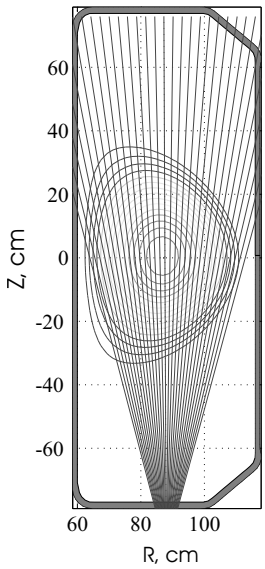

Figure 2.5: *The geometry of the MPX detector.*

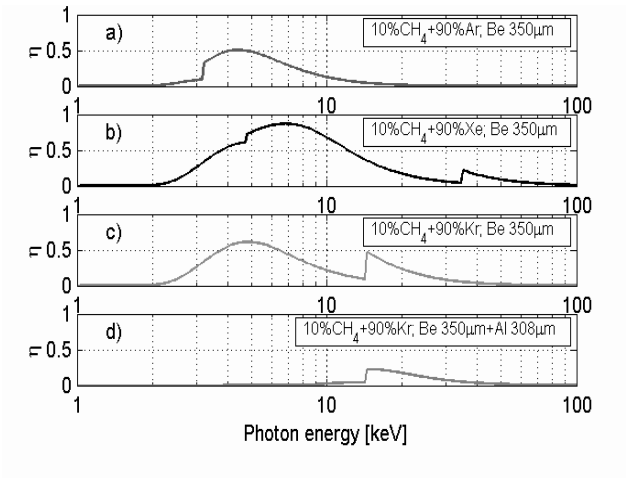

Figure 2.6: *MPX photon detection efficiency for different gas mixtures and absorber foils.*

MPX is equipped with a set of energy filters (aluminium and beryllium foils), which can be changed between tokamak discharges. Its gas chamber can be filled with different gases, resulting in different energy responses. The responses for some typical set-ups are shown in fig. 2.6.

The MPX is useful to detect the horizontal plasma position, positions of the rational surfaces, and to perform the corresponding cross-checks with the ECE system. It also helps in the study of the fast particle dynamics.

HXR

In addition to the soft x-ray diagnostics, typically sensitive to photons in the energy range 1-10 keV, a hard x-ray camera (HXR), with an energy range 10-200 keV, is installed on TCV [3].

The HXR camera has 14 spatial channels shown in fig. 2.7. Each channel has 8 CdTe detectors sensitive to different energy ranges. The temporal resolution depends on the number of photons emitted within the energy range corresponding to the diagnostic set-up. In plasmas with a significant number of suprathermal electrons it can be ∼1 ms.

The HXR camera allows the reconstruction of the radial HXR emissivity profile and emission spectra along a chord. In many regimes, the photon temperature, obtained from the HXR spectrum, is similar to the energy distribution of the suprathermal electrons. The HXR data complements the ECE data and the results of a Fokker-Planck code in cases where high temporal resolution is not required. The HXR camera is on loan from CEA, Cadarache.

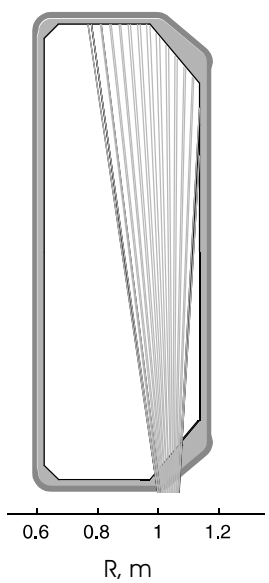

Figure 2.7: *HXR geometry.*

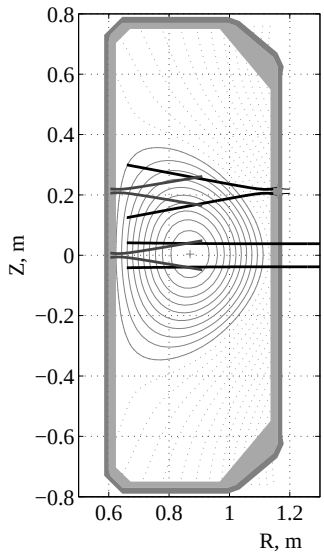

Figure 2.8: *The patterns of the four ECE antennas used for the temperature measurements in TCV.*

2.2.3 ECE radiometers

Electron cyclotron emission (ECE) of a plasma is proportional to the local electron temperature if certain conditions are fulfilled (see Chapter 5 for details). In addition, ECE can provide information about non-thermal electrons. On TCV there are two ECE radiometers. The ECE antenna beams are shown in fig. 2.8.

The first radiometer, developed prior to this work, has 24 channels in the frequency range 78-114 GHz. It views the plasma from the High Field Side (HFS) [4]. The radial resolution is $\Delta\ R \sim$ 1 cm and the temporal resolution is $\Delta t = 25\ \mu$s.

The second radiometer has been developed during this thesis work, and is described in details in Chapter 4. It has 24 channels in the frequency range 65-100 GHz, and it views the plasma from the Low Field Side (LFS). The radial resolution is $\Delta\ R \sim$ 1 cm and the temporal resolution is $\Delta t = 10\ \mu$s.

2.3 Magnetic equilibrium reconstruction

The knowledge of the magnetic field is essential for the calculation of the EC resonance location. The magnetic equilibrium can be reconstructed by solving the Grad-Shafranov equation:

$$R\frac{\partial}{\partial R}\left(\frac{1}{R}\frac{\partial\psi}{\partial R}\right) + \frac{\partial^2\psi}{\partial Z^2} = -\mu_0 R^2 p^{'}(\psi) - F(\psi)F^{'}(\psi) \tag{2.1}$$

where $\psi = \psi_{pol}/2\pi$, ψ_{pol} being poloidal flux. $F(\psi) = RB_{tor}$, p is the plasma pressure. Since the spatial dependence of ψ is not known, the problem is ill posed. An iterative scheme is usually used to find the solution of eq. 2.1.

The reconstruction of the magnetic equilibrium using the data of magnetic probes only is often inaccurate in the plasma core. The knowledge of the plasma pressure and current profiles improves the quality of the reconstruction.

On TCV, the magnetic equilibrium is routinely reconstructed using the Grad-Shafranov solver LIUQE [5]. The magnetic probe data and the energy stored in the plasma measured by the diamagnetic loop are used as basic input parameters. The plasma pressure profile, obtained from the Thomson scattering

measurements, as well as the $q = 1$ position from the x-ray inversion radius, can also be taken into account.

2.4 Gyrotrons on TCV

The TCV tokamak is equipped with nine gyrotrons providing a total power of 4.5 MW. The gyrotrons can be used for auxiliary heating and/or current drive. Six gyrotrons work at 82.7 GHz [6], corresponding to the second harmonic electron cyclotron (EC) resonance. Three gyrotrons work at 118 GHz, corresponding to the third harmonic EC resonance [7], [8]. All gyrotrons can work at full power for at least 2 s.

The gyrotrons launchers allow injection of the microwave power at different toroidal and poloidal angles. The launching geometry is shown in figs. 2.9, 2.10. More details about the gyrotron launchers, which can be used as ECE antennas, can be found in Chapter 4.

The main constraint for the application of the gyrotrons at 82.7 GHz on TCV is the density cut-off (see Chapter 3). Typical cut-off density for TCV is $n_{crit}^{82.7GHz} = 4 \cdot 10^{19}$ m^{-3}. The condition for the gyrotrons at 118 GHz is less strict: $n_{crit}^{118GHz} = 11 \cdot 10^{19}$ m^{-3}. Therefore, in high densities regimes, such as in High confinement mode (H-mode), the gyrotrons at 82.7 GHz cannot be used.

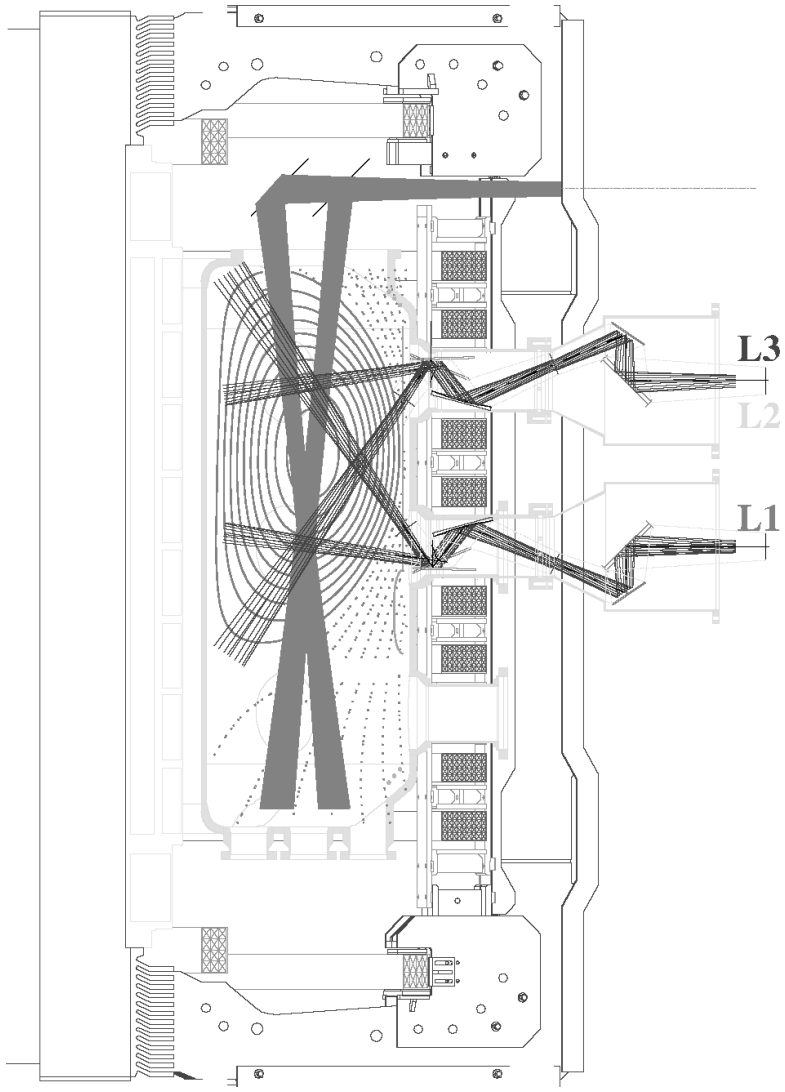

Figure 2.9: *Poloidal cross section of TCV. The ECRH beams are shown. The microwaves at 82.7 GHz are launched from the LFS, while the microwaves at 118 GHz are launched from the top of TCV.*

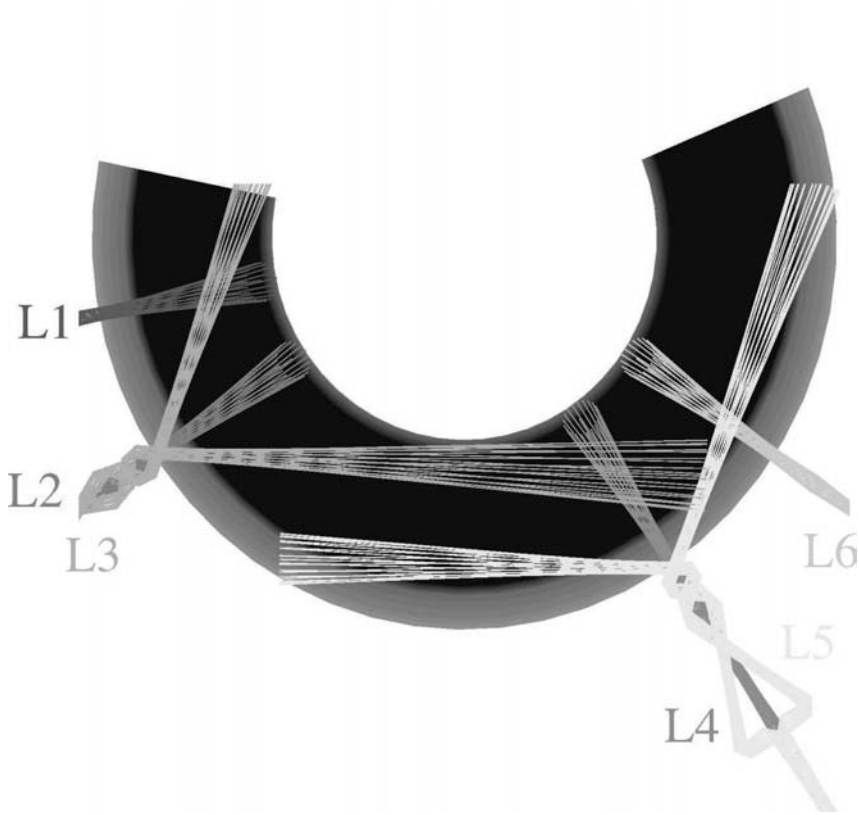

Figure 2.10: *Toroidal cross section of TCV. The RF beams are shown. While the power at the second harmonic can be injected at large toroidal angle, the third harmonic is normally injected perpendicular to the magnetic field.*

Chapter 3

Elements of theory of electromagnetic waves in plasma

In this chapter we introduce the basics of the theory of waves in plasma, which are essential for the understanding of the ECE in tokamaks. More specific developments, such as calculation of the emission and absorption, the transport of radiation and the ray-tracing, will be discussed later in Chapter 5.

3.1 Electromagnetic waves in a cold plasma

Since a general treatment of the electromagnetic waves in plasmas is a very complicated subject, we shall first consider the cold plasma approximation, which includes finite density effects and a plasma anisotropy due to an external magnetic field. The cold plasma approach neglects the thermal motion of the particles and allows their movement only due to an externally applied electromagnetic field, without collisions. Despite the simplicity, the cold plasma model describes many important phenomena, such as hybrid resonances and density cut-offs.

3.1.1 Dielectric tensor in a cold plasma

First we consider the response of the dielectric media to the applied electric field. If $\mathbf{E}$ is the applied electric field and $\mathbf{D}$ is the "induced" field (electric displacement), than $\mathbf{D} = \epsilon_0 \mathbf{E} + \mathbf{P}$, where $\mathbf{P}$ is the electric polarization ($\mathbf{P}$ and $\mathbf{D}$ have the dimension of coulomb/m^2). The electric properties of the

dielectric can be described by the electric susceptibility χ: $\mathbf{P} = \epsilon_0 \chi \mathbf{E}$ or electric permittivity ϵ: $\mathbf{D} = \epsilon_0 \epsilon \mathbf{E}$. The two quantities are related: $\epsilon = 1 + \chi$. For isotropic media ϵ is a scalar, for anisotropic media a tensor ($\hat{\epsilon}$). In terms of current, one can define the source current j_s, the "induced" current j and the total current $j_t = j_s + j$. The induced current can be derived from the polarization $j = \partial P / \partial t$. Therefore we have

$$\frac{\partial \mathbf{D}}{\partial t} = \epsilon_0 \frac{\partial \mathbf{E}}{\partial t} + \mathbf{j}. \tag{3.1}$$

Now we assume that the electric field and the other related quantities vary in time harmonically, i.e. $\sim exp(-i\omega t)$. From the eq. 3.1 using $\mathbf{j} = \sigma \mathbf{E}$ we get:

$$\epsilon = 1 + \frac{\sigma}{i\omega\epsilon_0} \tag{3.2}$$

To calculate the conductivity tensor $\hat{\sigma}$ for the plasma in a static magnetic field we use the equations of motion of charged particles in an electromagnetic field:

$$m_k \frac{d\mathbf{v_k}}{dt} = Z_k e(\mathbf{E} + \mathbf{v_k} \times \mathbf{B}), \tag{3.3}$$

where the k index denotes the particle species. Z_k,m_k and $\mathbf{v_k}$ are the charge, the mass and the velocity of the particle. We can choose the coordinate system such that the z axis is directed along the static magnetic field $\mathbf{B}$ without loss of generality. Projecting eq. 3.3 in case of harmonic electric field, we have:

$$\begin{cases} -i\omega m_k v_{kx} &= Z_k e(E_x + v_{ky} B) \\ -i\omega m_k v_{ky} &= Z_k e(E_y - v_{kx} B) \\ -i\omega m_k v_{kz} &= Z_k e E_z \end{cases} \tag{3.4}$$

The current carried by the particles can be calculated as follows:

$$\mathbf{j} = \sum_k n_k Z_k e \mathbf{v_k} \tag{3.5}$$

Solving the system 3.4 and substituting the components of $\mathbf{v_k}$ into eq. 3.5 we have the conductivity tensor. Finally, using eq. 3.2 we obtain the dielectric tensor for the cold plasma:

$$\hat{\epsilon} = \begin{pmatrix} S & -iD & 0 \\ iD & S & 0 \\ 0 & 0 & P \end{pmatrix} \tag{3.6}$$

$$S = 1 - \sum_k \frac{\omega_{pk}^2}{\omega^2 - \omega_{ck}^2}; \quad D = \sum_k \frac{\omega_{pk}^2 \omega_{ck}}{\omega(\omega^2 - \omega_{ck}^2)}; \quad P = 1 - \sum_k \frac{\omega_{pk}^2}{\omega^2}, \tag{3.7}$$

where the plasma frequency and the cyclotron frequency are:

$$\omega_{pk} = \sqrt{\frac{n_k Z_k^2 e^2}{\epsilon_0 m_k}}; \quad \omega_{ck} = \frac{Z_k e B}{m_k} \tag{3.8}$$

3.1.2 Dispersion relation

Having obtained the dielectric tensor we can solve Maxwell's equations to get the dispersion relation.

$$\nabla \times \mathbf{E} = -\mu_0 \frac{\partial \mathbf{H}}{\partial t} \tag{3.9}$$

$$\nabla \times \mathbf{H} = \epsilon_0 \frac{\partial \mathbf{E}}{\partial t} + \mathbf{j} \tag{3.10}$$

In many cases the radiation field can be represented as a superposition of plane waves. From eqs. 3.9, 3.10 for the plane wave, i.e. $\mathbf{E}(\mathbf{r}, t) = \mathbf{E} exp(i\mathbf{k} \cdot \mathbf{r} - i\omega t)$, where $\mathbf{k}$ is the wave vector, we have the wave equation:

$$\mathbf{k} \times (\mathbf{k} \times \mathbf{E}) + \left(\frac{\omega}{c}\right)^2 \hat{\epsilon}\mathbf{E} = 0 \tag{3.11}$$

Here we introduce the dimensionless vector $\mathbf{N} = \mathbf{k}c/\omega$, whose magnitude N is the refractive index, i.e. the ratio of the velocity of light to the phase velocity. If we assume that $\mathbf{N}$ lies in the xz plane and we call θ the angle between $\mathbf{B}$ and $\mathbf{N}$, then from eqs. 3.11 and 3.6 we have:

$$\begin{pmatrix} S - N^2 cos^2\theta & -iD & N^2 cos\theta sin\theta \\ iD & S - N^2 & 0 \\ N^2 cos\theta sin\theta & 0 & P - N^2 sin^2\theta \end{pmatrix} \begin{pmatrix} E_x \\ E_y \\ E_z \end{pmatrix} = 0 \tag{3.12}$$

In order to have a nontrivial solution, the determinant of the square matrix in eq. 3.12 must be zero. This condition gives the dispersion relation. It can be written as follows:

$$AN^4 - BN^2 + C = 0 \tag{3.13}$$

where

$$\begin{aligned} A &= Ssin^2\theta + Pcos^2\theta \\ B &= (S^2 - D^2)sin^2\theta + PS(1 + cos^2\theta) \\ C &= P(S^2 - D^2) \end{aligned} \tag{3.14}$$

3.1.3 Perpendicular view: X-mode and O-mode

Now we consider particular important case for the ECE diagnostics on tokamaks viewing the plasma perpendicular to the magnetic field. At $\theta = \pi/2$ eq. 3.13 has two solutions:

$$N_\perp^2 = P \tag{3.15}$$

$$N_\perp^2 = \frac{S^2 - D^2}{S} \tag{3.16}$$

The solution 3.15 is called Ordinary mode (O-mode), while the solution 3.16 is called eXtraordinary mode (X-mode). Substituting eq. 3.15 into eq. 3.12 we find that $E_x = E_y = 0$, which means that for the ECE diagnostics on tokamaks, the O-mode electric field is horizontal. Similarly, for the X-mode we find that $E_z = 0$ and therefore the electric field is vertical.

For the oblique view ($\theta \neq \pi/2$), there are usually two modes of propagation, which are solutions of the dispersion relation 3.13. They are elliptically polarized and normally one mode of propagation has much more power than another. Analogously to the case of perpendicular propagation, the higher power mode is often called the X-mode, while the other one is called the O-mode.

3.1.4 Density cut-off

A *cut-off* is defined where N^2 goes to zero. As it can be shown ([9]), it means that the wave cannot propagate and reflection occurs. From eq. 3.13

the condition $N^2 = 0$ is equivalent to the condition $C = 0$. Therefore we have three possibilities:

$$P = 0, \quad (S + D) = 0 \;\; or \;\; (S - D) = 0.$$

The corresponding cut-off frequencies are: the plasma frequency ω_p (eq. 3.8), the right-hand cut-off frequency $\omega_R = \omega_{ce}/2 + \sqrt{(\omega_{ce}/2)^2 + \omega_{pe}^2 + \omega_{ce}\omega_{ci}}$ and the left-hand cut-off frequency $\omega_L = -\omega_{ce}/2 + \sqrt{(\omega_{ce}/2)^2 + \omega_{pe}^2 + \omega_{ce}\omega_{ci}}$.

Since the wave cannot propagate if its frequency is lower than the cut-off frequency, we take the right-hand cut-off frequency to find the critical density. In the limit $\omega_{ci} << \omega_{ce}$, we have $\omega_{pe}^2 = \omega^2 - \omega\omega_{ec}$. For the m-th harmonic of the cyclotron frequency, i.e. $\omega = m\omega_{ce}$ we have

$$n_{crit} = m(m-1)\frac{\epsilon_0 B^2}{m_e} \tag{3.17}$$

For the second harmonic ECE we obtain

$$n_{crit}^{m=2} = 1.94 \times 10^{19} B^2 \quad [m^{-3}] \tag{3.18}$$

For the typical magnetic field on the TCV axis $B = 1.47$ T the critical electron density is $n_{crit}^{m=2} = 4.2 \cdot 10^{19} \quad \mathrm{m}^{-3}$.

3.1.5 Resonances in a cold plasma

A resonance occurs when N^2 goes to infinity. From the cold plasma dispersion (eq. 3.13) we have $A = 0$, therefore $\tan^2\theta = -P/S$, which gives the hybrid resonances. For the perpendicular propagation $\theta = \pi/2$ we have the upper and the lower hybrid resonances

$$\omega_{uh}^2 = \omega_{pe}^2 + \omega_{ce}^2, \qquad \omega_{lh}^2 = \frac{|\omega_{ci}\omega_{ce}|(\omega_{ci}^2 + \omega_{pi}^2)}{|\omega_{ci}\omega_{ce}| + \omega_{ci}^2 + \omega_{pi}^2}.$$

3.2 From cold plasma to real plasma

A relatively easy cold plasma approximation does not provide any information about the cyclotron resonances for perpendicular propagation. To analyze the wave behavior in the vicinity of the cyclotron frequencies the thermal motion of the particles has to be considered [10].

Without going into details about development of the dielectric tensor for the warm plasma, which implies the integration of the linearized Vlasov equation, we write the result for the plane wave [10]. We assume that the distribution function can be represented by a sum of maxwellian distributions, which can be anisotropic:

$$f_k(v_\perp, v_\parallel) = \sum_\nu f_{k\nu}(v_\perp, v_\parallel) = \sum_\nu \frac{exp(-v_\perp^2/\alpha_{\perp\nu}^2)}{\pi\alpha_{\perp\nu}^2} \frac{exp(-v_\parallel^2/\alpha_{\parallel\nu}^2)}{\pi\alpha_{\parallel\nu}^2} \Psi_\nu(v_\perp, v_\parallel) \tag{3.19}$$

where $\alpha_{\parallel\nu}$ and $\alpha_{\perp\nu}$ are mean parallel and perpendicular thermal velocities. Now we introduce dimensionless velocities $w = v_\perp/\alpha_\perp$, $u = v_\parallel/\alpha_\parallel$ and two other dimensionless quantities

$$\mu = \frac{k_\perp \alpha_\perp}{\omega_c}, \qquad x_n = \frac{\omega - n\omega_c}{k_\parallel \alpha_\parallel} \tag{3.20}$$

We also define the following differential operators:

$$L_\perp^n = R(\Psi)\left(1 - \frac{u}{x_0}\right) + \frac{\alpha_\perp^2}{\alpha_\parallel^2}\frac{u}{x_0} Q(\Psi)$$

$$L_\parallel^n = Q(\Psi)\left(1 - \frac{n\omega_{ck}}{\omega}\right) + \frac{\alpha_\parallel^2}{\alpha_\perp^2}\frac{n\omega_{ck}}{\omega} R(\Psi)$$

with

$$R(\Psi) = \Psi - \frac{1}{2w}\frac{\partial\Psi}{\partial w} \qquad Q(\Psi) = \Psi - \frac{1}{2u}\frac{\partial\Psi}{\partial u} \tag{3.21}$$

Now we can write the expression for the non-relativistic dielectric tensor.

$$\hat{\epsilon}_{ij} = \delta_{ij} - \sum_k \frac{\omega_{pk}^2}{\omega^2} \int_{-\infty}^{+\infty} \frac{e^{-u^2}}{\sqrt{\pi}} \left(-x_0 \sum_{n=-\infty}^{+\infty} \frac{\hat{Q}_{ij}^{k,n}}{u - x_n} \right) du \tag{3.22}$$

where

$$\hat{Q}_{xx} = \frac{4n^2}{\mu^2} \int_0^\infty w J_n^2(\mu w) e^{-w^2} L_\perp^n(\Psi) dw$$

$$
\begin{aligned}
\hat{Q}_{xy} &= i\frac{4n}{\mu}\int_0^\infty w^2 J_n(\mu w) J_n^{'}(\mu w) e^{-w^2} L_\perp^n(\Psi) dw \\
\hat{Q}_{xz} &= \frac{\alpha_\perp}{\alpha_\parallel} u \frac{4n}{\mu}\int_0^\infty w J_n^2(\mu w) e^{-w^2} L_\parallel^n(\Psi) dw \\
\hat{Q}_{yx} &= -i\frac{4n}{\mu}\int_0^\infty w^2 J_n(\mu w) J_n^{'}(\mu w) e^{-w^2} L_\perp^n(\Psi) dw \\
\hat{Q}_{yy} &= 4\int_0^\infty w^3 J_n^{'2}(\mu w) e^{-w^2} L_\perp^n(\Psi) dw \\
\hat{Q}_{yz} &= -4i\frac{\alpha_\perp}{\alpha_\parallel} u \int_0^\infty w^2 J_n(\mu w) J_n^{'}(\mu w) e^{-w^2} L_\parallel^n(\Psi) dw \\
\hat{Q}_{zx} &= \frac{\alpha_\parallel}{\alpha_\perp} u \frac{4n}{\mu}\int_0^\infty w J_n^2(\mu w) e^{-w^2} L_\perp^n(\Psi) dw \\
\hat{Q}_{zy} &= 4i\frac{\alpha_\parallel}{\alpha_\perp} u \int_0^\infty w^2 J_n(\mu w) J_n^{'}(\mu w) e^{-w^2} L_\perp^n(\Psi) dw \\
\hat{Q}_{zz} &= 4u\int_0^\infty w J_n^2(\mu w) e^{-w^2} L_\parallel^n(\Psi) dw
\end{aligned}
\tag{3.23}
$$

One can note that even without relativistic effects, which are important in the vicinity of an electron cyclotron resonance, the calculation of the dielectric tensor is not easy. Moreover, since the calculations should be performed for many points in the plasma to obtain the emission or absorption properties even for a single frequency, reasonable simplifications have to be made. One of the possible ways to do so, which has been realized on TCV, is described in Chapter 5.

Chapter 4

Development and implementation of the 65-100 GHz ECE radiometer on TCV

4.1 Motivation

The main objective of the ECE radiometer is the measurement of the electron temperature with high temporal and spatial resolution. Temperature measurements are required for most tokamak plasma studies, namely in the areas of transport, heating and current drive, stability, etc. The main advantage of the ECE method over Thomson Scattering is a much better temporal resolution ($\Delta t_{thomson} \sim 10^{-2}$ s, $\Delta t_{ece} \sim 10^{-5}$ s, see fig. 4.1), which allows one to study fast processes such as heat pulse propagation or MHD modes.

The TCV tokamak has been equipped with a radiometer viewing from the HFS since 2000 [4]. The construction of a radiometer viewing the plasma from the LFS on TCV was motivated by several reasons. First, a LFS radiometer can give information about the plasma bulk temperature even in the presence of a small fraction of non-thermal electrons due to the reabsorption of the non-thermal ECE in the plasma bulk, whereas the HFS ECE spectra would already be non-thermal. Second, there was a possibility to improve the new radiometer sensitivity compared to the HFS radiometer by buying higher quality frontend components. Less noisy receivers can imply better resolution if needed. Third, having two independent radiometers makes the ECE diagnostics system more flexible and reliable, with the possibility to do cross checks or to measure the electron temperature at completely different locations at the same time. Fourth, the LFS radiometer frequency range is

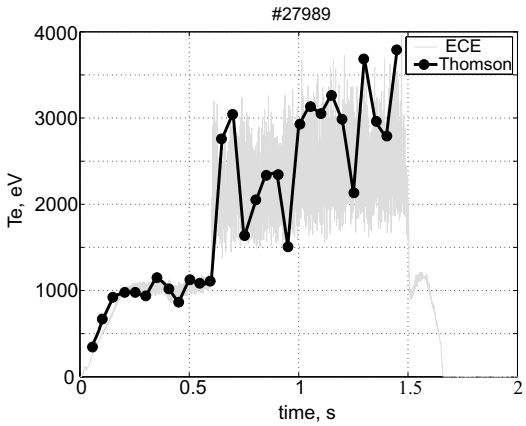

Figure 4.1: *Electron temperature time traces obtained from Thomson scattering and ECE measurements. As one can see, ECE provides much more detailed information due to better time resolution. Large amplitude oscillations during ECRH phase (t=0.6-1.5 s) are due to sawteeth.*

suitable for Electron Bernstein Emission (EBE) studies (later in this chapter), since the upper hybrid resonance where X to B mode conversion takes place is below 100 GHz for densities below $1 \cdot 10^{20}$ m^{-3}.

Here below we describe the development and implementation of the new LFS radiometer, as well of its lines of sight. The tests, noise measurements and calibrations will also be briefly discussed. Typical examples demonstrating the use of the LFS radiometer alone and together with the HFS radiometer will be presented. The unique measurements using a steerable antenna will be shown.

4.2 Definition of the main design parameters

The performance of a radiometer (spatial and temporal resolution, sensitivity) depends on a number of parameters, including the frequency map and the video bandwidth [11], [12]:

$$\Delta T_{min} = T_r \sqrt{\frac{2B_v}{B_{IF}}}. \tag{4.1}$$

Here ΔT_{min} is the smallest change in the source temperature that can be detected, T_r the receiver noise temperature, B_v the video (output signal) bandwidth, and B_{IF} the radiometer channel bandwidth (before detection).

As one can see in eq. 4.1, better temporal (larger B_v) or spatial (narrower B_{IF}) resolution lead to worse sensitivity (higher ΔT_{min}).

The frequency map of the radiometer is the set of RF frequencies to which the radiometer is sensitive. It can be represented as a set of central frequencies and bandwidths for each channel. The frequency map is chosen according to the tokamak magnetic field, to the desired number of channels and radial resolution. In order to reach the best performance, the frequency map should be kept fixed.

The video bandwidth defines the temporal resolution and affects the signal to noise ratio.

In the following we address the design criteria used for the development of the LFS ECE system on TCV.

4.2.1 Choice of harmonic

In principle, in order to measure the electron temperature one can use ECE on every harmonic that is optically thick, provided there are no other restrictions such as the density cut-off. For the same tokamak plasma, the second harmonic X-mode and the first harmonic O-mode have the highest optical depth. The choice between two candidates for TCV is clear, since the first harmonic frequencies will always be cut-off (see Chapter 3 for more details). The optical depth for any other harmonic and polarization is at least an order of magnitude lower. For instance, the third harmonic X-mode, for which the density cut-off value is higher, for most TCV regimes is not optically thick. Therefore, the radiometer was designed to measure ECE at the second harmonic X-mode (ECE-X2). [1]

4.2.2 Radial coverage and frequency range

In some tokamaks the choice of the frequency range of the ECE radiometer is problematic due to large variations of the magnetic field, which make it impossible to cover all the plasma in all regimes. In these cases there are two solutions, either the deployment of several radiometers or the use

[1] See [13] for the formulas to estimate the optical depth for the different harmonics and polarizations.

of quasi-optical instruments, such as Michelson interferometers or grating spectrometers. The drawback of the latter solution is poorer resolution and sensitivity compared to a heterodyne radiometer [12].

In the TCV tokamak the maximum magnetic field is limited to 1.5 T, with the majority of the experiments performed in the range 1.3-1.47 T. Thus, the choice of the frequency range for the ECE radiometer is an easy task.

However, harmonics overlap needs to be taken into account. For a tokamak, there is no overlap between $(n-1)$ and n-harmonic if the aspect ratio $(R/a) > (2n-1)$ [12]. For $n = 3$ in TCV we have $(0.88/0.24) = 3.67 < 5$, so there is an overlap between the second and the third harmonic. This means that for a given frequency that one would normally map on the HFS of the tokamak, there will also be emission on the higher harmonic coming from the LFS. This results in a pollution, which depends on the plasma density and temperature, varying during the shot. In addition, a finite temperature causes the resonance layer for the third harmonic to become wider and to move to the center of the plasma (relativistic downshift). In the presence of fast electrons the measurements may not be representative of the electron temperature.

That is why we decided not to measure at frequencies overlapping with the third harmonic cold resonance emission, and chose 100 GHz as the high frequency limit. The low frequency limit is defined by the LFS edge of the plasma, where the temperature never gets high enough to be measured accurately. In some regimes the lowest frequency channel (at 65 GHz) is even outside the last closed flux surface.

4.2.3 Number of channels

There are several elements to consider in the choice of the number of channels: the cost of the system and its complexity, the signal to noise ratio and the necessity to measure the temperature at many radial points. A radiometer with few channels would be easier, cheaper and more sensitive than one with many channels, because each channel would get a larger part of the signal collected by the antenna and insertion losses for narrow band elements (especially for the mixer and the first amplifier) would be lower. However, such a radiometer would provide incomplete information on radial profiles. Twenty four channels was considered to be a good compromise.

The frequency range and the central frequencies for each channel for both radiometers are shown in fig. 4.2. The radial coverage is calculated for shot #24890 (B=1.445 T). The LFS radiometer covers R from 0.72 m to 1.10 m. The HFS radiometer covers R from 0.62 m (outside the plasma) to 0.92 m. The central frequency of each channel is mapped on a radial location using the second harmonic cold resonance for both radiometers.

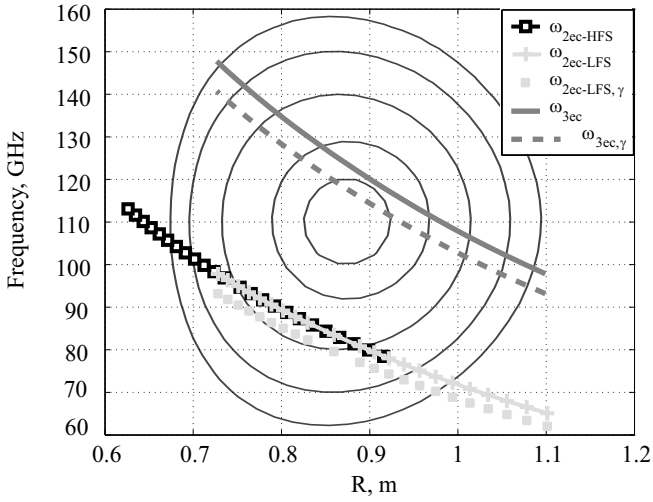

Figure 4.2: *The frequency map and the radial coverage are shown. The third harmonic resonance is also shown. The dotted curve ($\omega_{2ec-LFS,\gamma}$) and the dashed curve ($\omega_{3ec,\gamma}$) show the relativistically downshifted resonance ($\gamma = 1.05$) for the second and the third harmonic.*

4.2.4 Video bandwidth

The video bandwidth, i.e. the pass band of the amplifier after the power detector, defines the temporal resolution and affects the signal to noise ratio. For typical physical problems in tokamak research a temporal resolution of about 10 μs is sufficient (the typical energy confinement time $\tau_E > 10$ ms). A further increase in video bandwidth would degrade the signal to noise ratio, which is $\sim \sqrt{B_v}$ (see eq. 4.1).

4.3 Frontend of the radiometer and the first IF amplifier

Nowadays, most radiometers are based on the heterodyne principle [12]. The input signal in the RF range is mixed in a non-linear device (mixer) with a signal at a known frequency (the local oscillator, LO) to produce the signal at a lower frequency, whose power is proportional to the input power (fig. 4.3). The frequency of the output signal is called intermediate frequency (IF) and normally lies in the 1-20 GHz frequency range.

The signal in the IF range can be filtered and amplified more easily and effectively than the original signal. This frequency down-conversion stage is called radiometer frontend, and is usually followed by the low noise amplifier (LNA). If the LNA gain is sufficient, the contribution to the noise temperature of the diagnostics from the following stages of the radiometer can be negligible [12].

The noise temperature of the diagnostics directly affects its sensitivity, and should be kept as low as possible. That is why we paid more attention to the frontend and the LNA than to the IF and video stages. Below we discuss this part of the radiometer in detail.

4.3.1 RF scheme, description and layout

A scheme of the frontend along with the LNAs is presented in fig. 4.3. At the RF entrance of the radiometer there is a remotely controlled 4-position switch driven by compressed air that connects the radiometer to one of the three antennas or disconnects it for protection. Next, there are two notch filters (-70 dB) [2] to protect the radiometer from excessive microwave power from the gyrotrons in case of low absorption in the plasma (a single gyrotron on TCV generates 500 kW of microwave power, while 1 mW at the entrance of the radiometer would destroy the mixer). One filter rejects waves around 82 GHz that correspond to the gyrotrons heating at the second harmonic, the other does the same at 118 GHz - frequency of the gyrotrons working at the third harmonic. After that, a 3 dB directional coupler splits the power into two branches. The first branch has a Gunn local oscillator (LO) at 63 GHz. The second LO works at 81 GHz. Before the mixers, there are high pass filters (HPF) to reject the image frequencies below LOs'. In the higher frequency (83-100 GHz) branch an isolator prevents leakage of the 81 GHz

[2] definition of dB units commonly used in microwave technique: $A_{dB} = 10log_{10}A$

LO power to the lower frequency branch (65-81 GHz). After the frequency down conversion stage, there is 35 dB LNA working up to 18 GHz. Finally we have two IF signals up to 18 GHz. The layout of the RF part is shown in fig. 4.4.

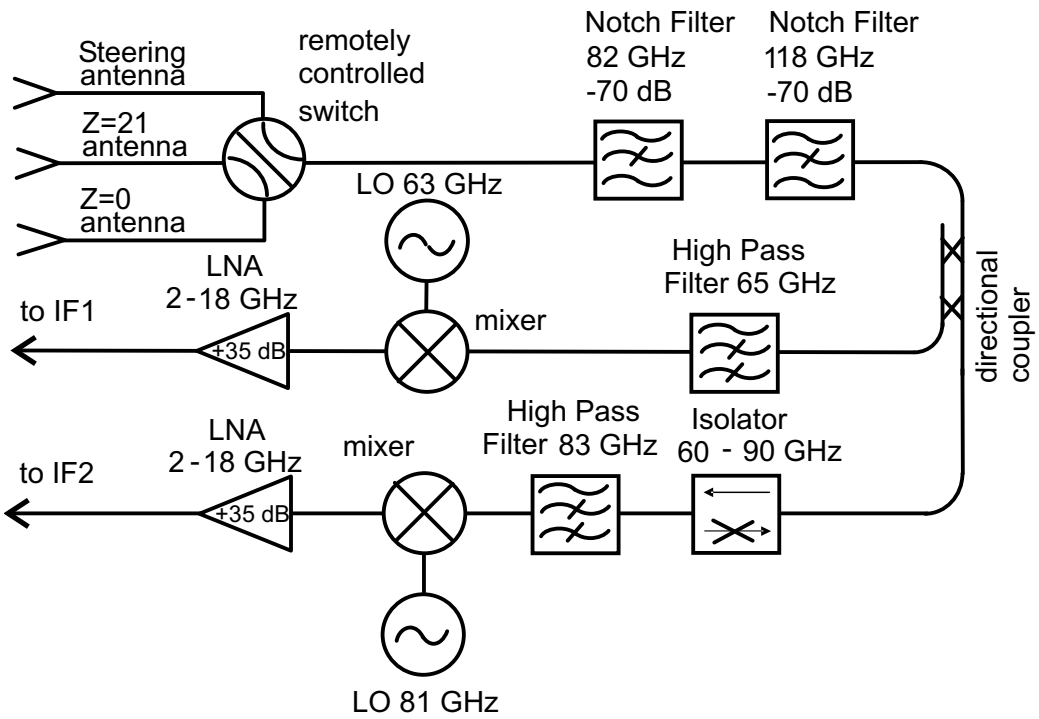

Figure 4.3: *The scheme of the RF part of the radiometer.*

4.3.2 Loss and gain calculation

To estimate the gain needed in the radiometer one should know the RF input power and the losses at different stages. The losses between the plasma and the entrance of the radiometer were estimated to be 10 dB (and later were measured to be 7 dB). Since the waveguides were not built yet at the time of the design of the radiometer, it was hard to provide a more precise estimation. The motorized switch introduces 1 dB loss, the notch filters 2 dB each, the high pass filters from 1.25 to 1.5 dB. The 3-dB directional coupler reduces the power for each branch by 3 dB and causes 1 dB insertion loss. The full band isolator insertion loss is up to 2.5 dB. Mixer conversion losses are from 8.5 to 9 dB. Finally, the low noise amplifier has a gain of 35 dB.

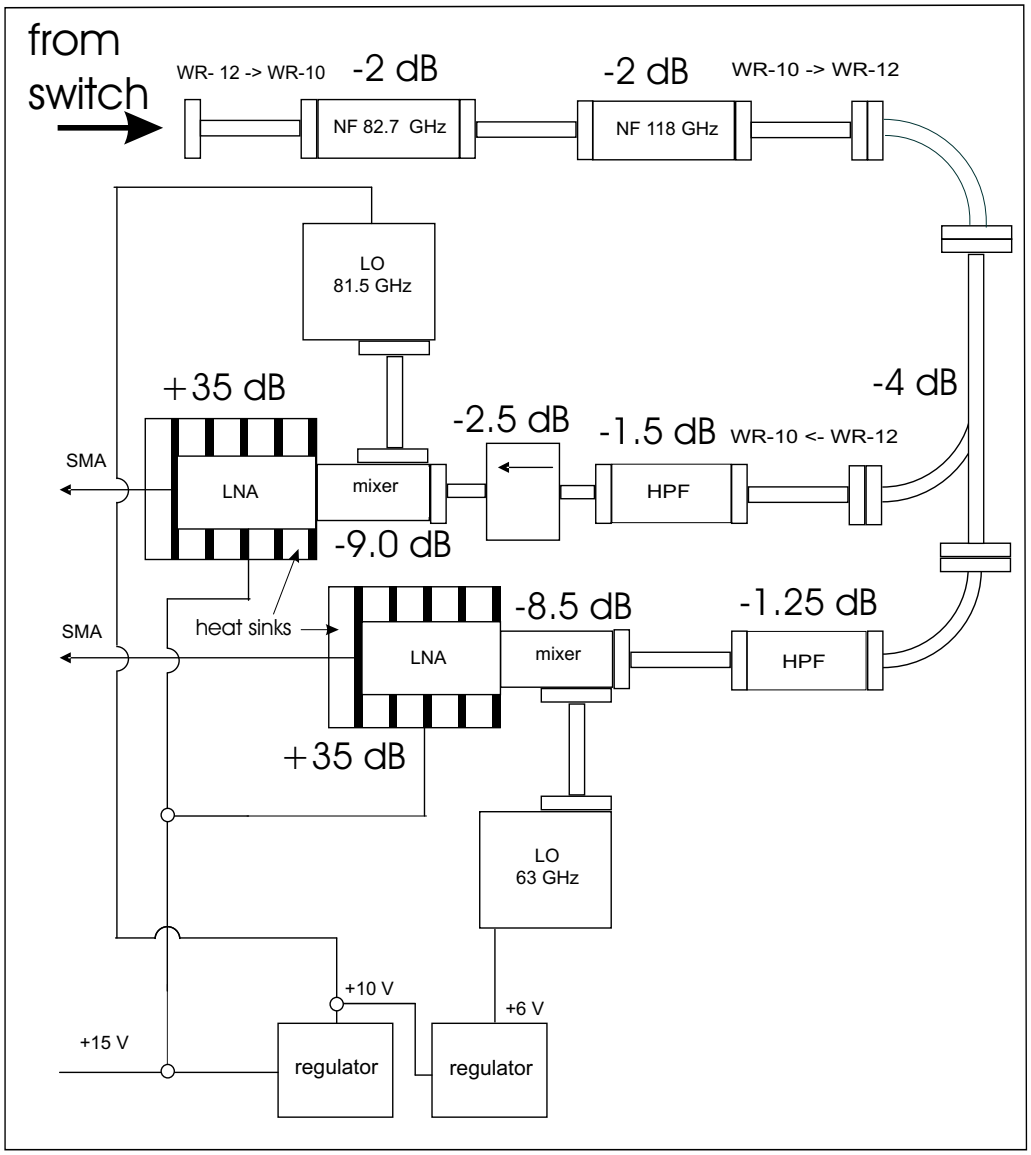

Figure 4.4: *The layout of the RF part of the radiometer. Main losses are indicated. The switch adds 1 dB loss.*

As a result, we should have an overall 6 dB gain for the 65-81 GHz branch (3 dB for the other branch) at the entrance of the IF spectrometer compared to the signal collected by the antenna, which can be calculated in the Rayleigh-Jeans approximation ($hf << k_BT$): $P = k_BTB$, where k_B is the Boltzmann constant, T is the source temperature and B is the receiver bandwidth. The expected plasma temperature range for TCV is 100 eV to 10 keV. The bandwidth of the radiometer is about 35 GHz. Finally, we expect a range 0.5 to 50 μW for the power of the signal collected by the antenna. The expected signal at the entrance of the IF stage should have a power in the range of 2 to 200 μW.

4.3.3 RF Test equipment

The main pieces of equipment used for the series of tests were a HP 70000 spectrum analyzer, a mechanically tunable Gunn diode (70-90 GHz), absolutely calibrated Thomson biased detectors, in addition to sources, detectors and passive components.

4.3.4 Tests of the RF components

All RF components were tested individually. LOs must provide enough power to drive the mixers ($P > 20$ mW), with stable frequencies. The mixers together with LOs should down convert the RF frequency to the IF frequency: $f_{IF} = f_{RF} - f_{LO}$. The output IF power should be proportional to the input RF power, provided the RF power does not saturate the mixer. For $RF\ power <$ 1 mW this condition is satisfied. The LO power must not exceed 100 mW to avoid damaging the mixer.

The passive components were also tested. The 3 dB directional coupler has to split the input RF signal in two equal components in the frequency range of interest (65-100 GHz). The HPFs have to reject the image band (frequencies below LOs'). All the components successfully passed the tests. The notch filters have to provide as much attenuation as possible at the gyrotron frequencies. The maximum attenuation depth declared by the manufacturer is -70 dB. We were only able to verify the attenuation down to -60 dB, which can be considered satisfactory.

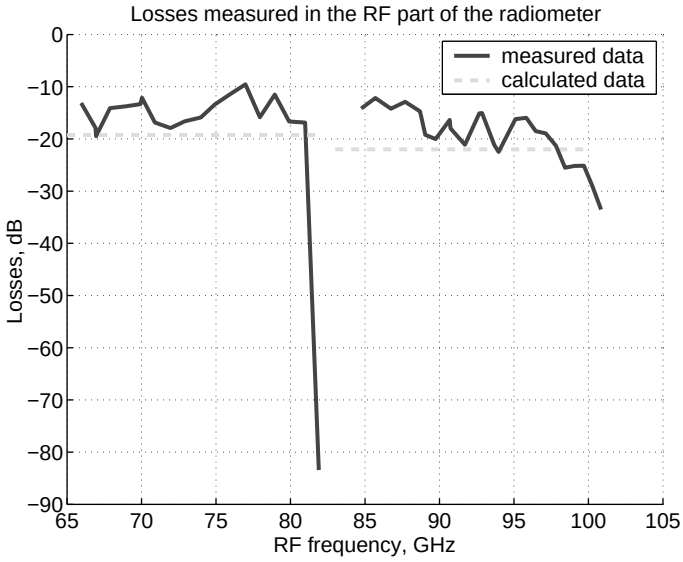

Figure 4.5: *The measured losses compared to calculated ones (based on the data provided by the manufacturers). The sharp drop around 82 GHz is caused by the notch filter. Frequencies higher than 100 GHz are outside the range of interest.*

4.3.5 Loss measurements in the RF part

After these individual tests, the RF components were assembled together according to the scheme shown in fig. 4.4. The losses in the RF part from the switch to the entrance of the LNA were measured and compared with the data provided by the manufacturers, as presented in fig. 4.5.

4.3.6 Spurious signal

It is important to avoid artificial/spurious signal in the measured ECE spectrum. In the preliminary RF assembly in the higher frequency branch, a peak around 4 GHz was found. It did not depend on the input RF signal and had an amplitude comparable to that expected from the plasma. The hypothesis that an overloaded mixer generates the spurious signal was not confirmed. Instead, the observed peak can be explained as follows. The LO at 81.5 GHz works at the second harmonic, thus its fundamental frequency

is 40.75 GHz and higher harmonics, such as the third one at 122.25 GHz, may be generated. Even if the LO power level at the third harmonic is 20-30 dB lower than at the second one, it is still non-negligible compared to the input RF signal from the plasma. The second harmonic of the LO working at 63 GHz - 126 GHz goes back through the HPF and the directional coupler, which is transparent for such frequency. Then it reaches the mixer in the higher frequency branch, where the LO provides not only 81.5 GHz, but also some power at 122.25 GHz. As a result, there is a 3.75 GHz output signal independent of the input RF signal from the plasma.

The easiest solution to this problem was tuning the LO frequency by few hundreds of MHz, so the spurious signal would be in the gap between the IF channels and would not affect the output spectrum. Fortunately, the power level of the spurious signal was not high and did not cause any saturation. The resulting displacement of the channel resonances by a few millimeters in the plasma is negligible. An alternative solution would be one more isolator or additional filter in the RF part, but this would increase the radiometer noise temperature by 2 dB.

4.3.7 LNA heat sink

The main danger for the LNA is overheating. Despite the low power consumption (2 W), the LNA heats up very quickly and needs a heat sink to keep the case temperature below 50-70 ^{0}C. Once the LNAs were properly mounted onto heat sinks, the case temperature did not exceed 40 ^{0}C. The temperature data taken after the LNA switch-on is presented in fig. 4.6.

For more details about RF part of the radiometer see annex A.

4.4 IF part and the backend of the radiometer

Even if the IF stage and the backend do not degrade the sensitivity of the system significantly (eq. 4.2), important issues, such as the dynamic range together with high gain, temperature stability, linearity and isolation between the channels need to be addressed. In addition, the diagnostic should be as flexible as possible, allowing easy interventions for minor modifications or repairs, and remote control.

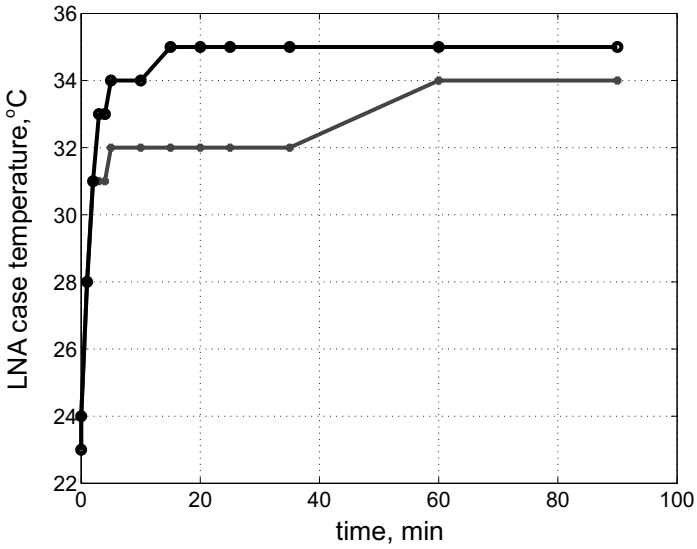

Figure 4.6: *The measured temperature of the LNAs after the switch-on (t=0). Temperatures above 50-70 ^0C would be dangerous.*

$$T_r = T_m + L_c \left(T_{IF}^{LNA} + \frac{T_{IF}^{(2)}}{G_{IF}^{LNA}} \right), \tag{4.2}$$

If we consider the receiver as the mixing stage with the noise temperature T_m and conversion loss L_c, followed by two IF amplifiers, LNA and (2), with noise temperatures T_{IF}^{LNA} and $T_{IF}^{(2)}$, the total receiver noise temperature can be calculated using eq. 4.2. The contribution of the amplifier (2) is decreased by the factor of G_{IF}^{LNA}, which is the gain of the LNA. If there would be a third amplifier, its contribution would be reduced by the factor $G_{IF}^{LNA} G_{IF}^{(2)}$. Therefore the backend of the radiometer should not degrade the sensitivity of the receiver.

4.4.1 The principal scheme and description of the IF stage

The intermediate frequency (IF) stage is presented in fig. 4.7. There are two 12-channel IF spectrometers. The signals up to 18 GHz are split into 12 channels using a power divider. In each channel the signal is amplified, then its frequency is down converted for the second time using transistor based

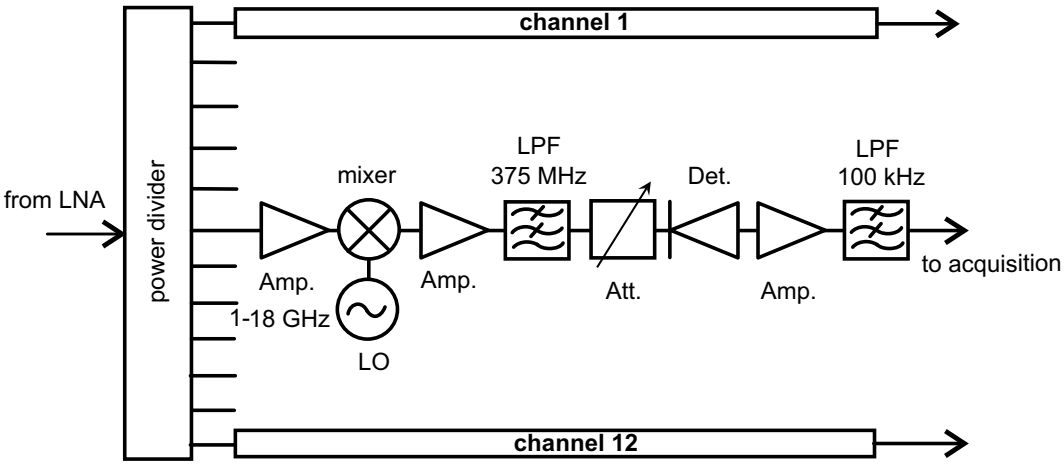

Figure 4.7: *IF scheme.*

LO at fixed frequency and a double-side-band balanced mixer. After the mixing stage there is a 9-pole Chebyshev low-pass filter (LPF) limiting the IF bandwidth to 750MHz. The frequency step between channels is 1.5 GHz, and all of the channels are equally spaced in frequency with the exception of channels near 82.7GHz, which corresponds to the emission frequency of the gyrotrons used on TCV. The channel video bandwidth is 100 kHz, as opposed to 40 kHz for the HFS radiometer. A digitally controlled attenuator with 0.5 dB steps can decrease the signal by up to 20 dB to avoid saturation. Finally, the power is rectified and amplified with a pass band of 100 kHz. The video stage is placed in a temperature controlled volume to ensure stability.

4.4.2 Tests

The isolation between channels in the IF multichannel spectrometer with frequency down conversion has to be verified. Since the frequency selection is done by mixing with LO power at fixed frequency (active selection) and not just by filtering the signal (passive selection), a leakage of the mixture of different harmonics through the power divider is possible. The isolation between channels is defined as the ratio of the output signal of the channel corresponding to the input frequency to the response of any other channel. Note that the test signal bandwidth is narrower than the channel bandwidth.

Isolation of all channels in both IF spectrometers was tested for the frequency range of interest (1-18 GHz). The typical result for most channels was found

to be 30 dB, which is satisfactory.

The gain in the IF part was found to be sufficient. All digitally controlled as well as mechanically tuned attenuators work correctly.

For more details about the IF part of the radiometer see annex B.

4.5 Antennas and waveguides

Before every TCV discharge the LFS radiometer can be connected to one of the three existing lines of sight (fig. 4.8) via a remotely controlled switch.

Each line consists of a focusing element (lens or mirror), an antenna to couple the beam to the waveguide, an oversized waveguide (∼5 m total length) to deliver the RF signal to the radiometer with minimum losses and a short section of fundamental rectangular waveguide (∼30 cm).

The first line of sight is in an equatorial plane (Z=0) and uses a thermoplastic polymethylpentene (TPX) lens as the focusing element. It views the plasma horizontally, perpendicular to the toroidal magnetic field.

The second line of sight also views the plasma horizontally, perpendicular to the magnetic field at Z=+21.2cm. This line includes a small scalar feed horn as an antenna and an elliptical mirror as the focusing element. The mirror, the antenna and some waveguide pieces are inside the vacuum vessel.

These two lines are justified by the fact that in TCV the plasma can be centered on a wide variety of Z-positions, and the most frequently used plasmas are centered at either Z=0 or Z=+23 cm.

The third line of sight includes a steerable antenna, which is normally connected to a gyrotron for X2 Electron Cyclotron Heating (ECH) and Electron Cyclotron Current Drive (ECCD) experiments. Depending on the orientation of the antenna before the discharge, the antenna can be swept in the poloidal, toroidal or any inclined plane. The antenna angle can be varied from 7° to 55° (0° corresponding to the perpendicular view in the horizontal plane) twice during the TCV discharge. This enables electron Bernstein emission studies and oblique ECE measurements. A detailed description of the steerable antenna can be found in [6].

The HFS radiometer uses one of two conventional ECE lines placed again at Z=0 and Z=21.2 cm in a poloidal section different from the one used by the LFS ECE lines. Both HFS transmission lines are designed similarly to the second LFS line of sight.

4.5.1 Quasi-optical calculations

To calculate the RF beam shape along its trajectory between the antenna and the plasma, the beam is assumed to have a gaussian amplitude distribution $E(r) = E(0)exp(-(r/w)^2)$, where r is the radial coordinate and w the beam radius. The real power distribution along the beam radius is indeed measured to be close to gaussian (see fig. 4.11).

If the beam propagates along the z axis, its radius varies as

$$w(z) = w_0[1 + (\lambda z/\pi w_0^2)^2]^{1/2}, \tag{4.3}$$

where w_0 is the beam waist radius (minimum beam radius), λ the wavelength and z the distance from the beam waist [14].

In order to improve the spatial resolution one can use focusing optics. Normally the choice is between thin dielectric lenses and reflecting metallic mir-

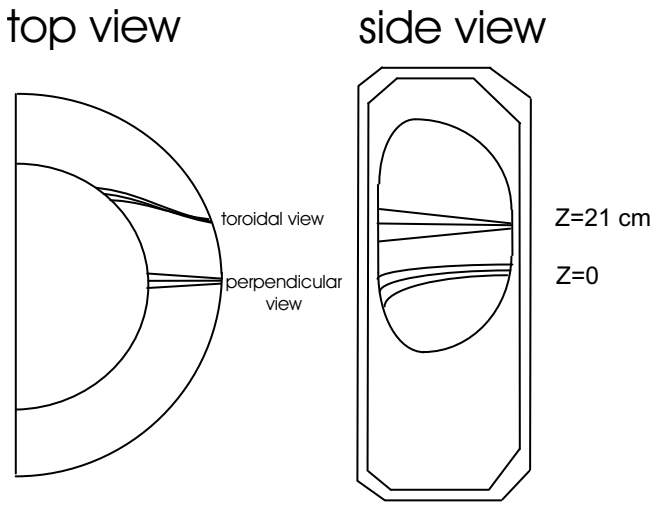

Figure 4.8: *Three lines of sight of the radiometer. The beam trajectories have been calculated by the TORAY-GA code, taking into account the beam divergence and refraction on the plasma.*

rors. In both cases the amplitude distribution across the beam should not change much, but the phase shifts by $\Delta\Phi = \pi r^2/\lambda f$, where f is the focal distance, creating the new waist. The distance from the focusing element to the new waist is:

$$d_2 = f[1 + \frac{d_1/f - 1}{(d_1/f - 1)^2 + (\pi w_{01}^2/\lambda f)^2}], \tag{4.4}$$

where d_1 is the distance to the first waist and w_{01} the first waist radius.

For the first line of sight, a bi-convex lens of TPX was fabricated with radii of 276 mm. The refractive index of TPX is 1.46, hence the focal distance $f = \frac{R_1 R_2}{(R_1+R_2)(n-1)} = 300$ mm. For the 1-inch oversized waveguide used as antenna and a distance between the first waist and the lens of 300 mm, the gaussian beam radius varies as shown in fig. 4.9. As one can see, the beam radius is more or less constant across the plasma, i.e. the beam is nearly parallel. The refraction effects due to the plasma density gradient are not taken into account here.

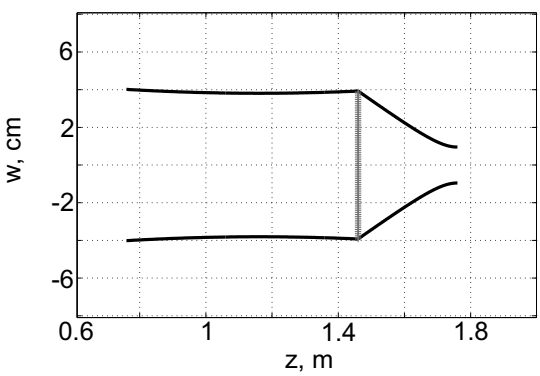

Figure 4.9: *The gaussian beam calculated using quasi-optical equations for the line in the equatorial plane. The optical axis z coincides with the tokamak major radius.*

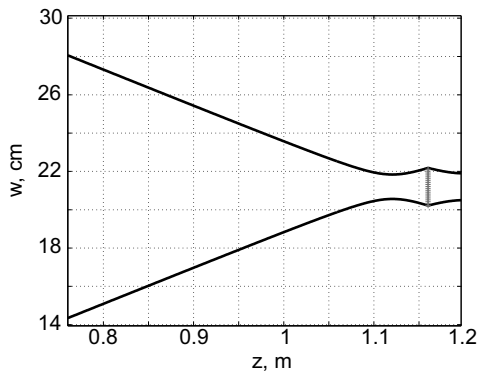

Figure 4.10: *The gaussian beam calculated using quasi-optical equations for the line with the elliptical mirror. The optical axis z coincides with the tokamak major radius.*

The elliptical mirror (section of an ellipsoid) with distances to foci d_1 and d_2 is equivalent to a thin lens with focal length $f = d_1 d_2/(d_1 + d_2)$. The advantage of the elliptical mirror is that the beam can be refocused from the

antenna waist to some point in the plasma and the antenna does not have to view the plasma directly. This is important since there is no vacuum window in TCV around Z=+20 cm and we have only 19 mm from the tokamak wall to the carbon tile surface. Hence the only possibility was to place the antenna parallel to the wall.

The room constraint makes it impossible to have nearly parallel beam as for the first line with the vacuum window. The mirror size, 18 mm, is not large compared to the wavelength, 3-4.6 mm, therefore diffraction plays an important role and the beam can not be focused on the distances larger than $D_a^2/2.44\lambda = 30 - 45$ mm. The Fresnel number in our case is $F = 0.5 - 0.7$, while Fraunhofer diffraction occurs at $F << 1$. The geometry of the beam in the space focused by the elliptical mirror with focal distance 37 mm is shown in fig. 4.10.

4.5.2 Scalar feedhorn

The corrugated or scalar feed horn (SFH) was installed in the second (Z=21 cm) line of sight because it has low sidelobes (< -30 dB). When the antenna does not view the plasma directly, but only the power reflected from the small mirror, the sidelobe signal coming from the plasma could be comparable with the main lobe signal. The measurements of SFH pattern performed in the lab are presented in fig. 4.11. No sidelobes have been detected at the -20 dB level. The cross-polarization level is -21 dB. See annex C for more details.

4.5.3 Oversized waveguides

To reduce the losses between the antenna and the radiometer to acceptable levels one can either place the radiometer close to the antenna to make the waveguides as short as possible or use oversized waveguides. The former solution is not always possible because of room constraints. In addition, the magnetic field of the tokamak can affect the functioning of the radiometer. The latter solution provides more flexibility. Using waveguides of size an order of magnitude larger than the wavelength, one can reduce the losses by an order of magnitude compared to fundamental waveguides.

The oversized waveguides used on TCV for ECE measurements are Oxygen Free High Conductivity (OFHC) copper tubes with 1 inch outer diameter. There are five miter bends in each line of sight. See annex C for more details.

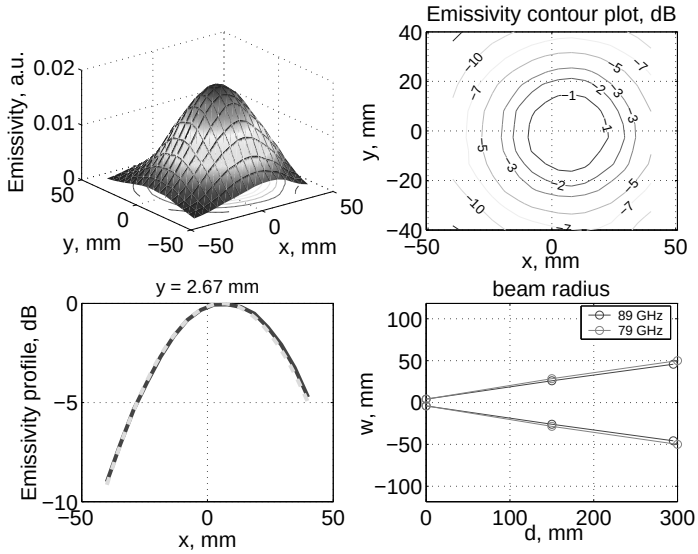

Figure 4.11: *The pattern of the scalar feed horn measured in the lab. 3D view, emissivity contour plot, the emissivity profile and the beam divergence for 79 and 89 GHz are plotted. The emissivity profile (solid line) is plotted along with the calculated gaussian profile (dashed line), confirming that the beam profile is indeed gaussian.*

4.5.4 Fundamental waveguides and motorized switch

The main RF components are connected by WR-12 (E-band) waveguides, designed for the 60-90 GHz frequency range (cut-off frequency 48.4 GHz), though there are some components made in the WR-10 dimension (W-band, 75-115 GHz, 59 GHz cut-off frequency). The radiometer is connected to oversized waveguide by a short section (∼30 cm) of WR-12 fundamental rectangular waveguide, a transition from rectangular to circular waveguide and a taper transition from fundamental waveguide with diameter 3.18 mm (0.125 inch) to an oversized waveguide with diameter 23.4 mm.

The switch at the entrance of the radiometer allows the connection to one of three existing ECE lines. The standard mechanical 4-position microwave switch (E-band) was connected to a compressed air driven motor. Since the sources of compressed air exist on TCV and are routinely controlled via standard computer interface, the remote control of the radiometer switch was easily implemented. The switching time is 2-3 seconds. Hence the radiometer can be easily connected to one of three antennas or disconnected before every

shot.

4.6 Noise temperature measurements and calibrations

In order to obtain the electron temperature from ECE measurements the receiver system (including the whole transmission line) has to be absolutely calibrated. The ideal way to calibrate the radiometer would be to use a black body at the temperature close to the plasma temperature range (100 eV - 10 keV). Unfortunately, such black bodies with known temperature do not exist.

Black bodies at temperatures up to 1000 ^{0}C can not be easily used because the signal generated by such a noise source is much lower than the noise generated by the radiometer itself.

Another approach is to use calibrated solid-state noise sources whose microwave noise power is equivalent to temperatures of the order of 10 eV, comparable to the receiver noise temperature (defined below in section 4.6.1).

The main problem for the absolute receiver calibration is the access to the vessel. Another serious problem is the validity of the calibration during months of tokamak operation. First, the receiver gain depends on the room temperature, as the broadband LNA does not have any feedback control of the gain, which depends on the frequency. The cubicle with the radiometer is equipped with fans to help reducing temperature variations. The power detector in each channel is placed in a temperature controlled volume to insure that the dependence of the gain on the room temperature does not exceed 1% per 1°C.

In conclusion, we can say that absolute calibration once a year would not be reliable for the whole year of the tokamak operation. Instead, we decided to perform cross-calibration on the temperature measured by the Thomson scattering diagnostics, which is recalibrated every few months.

Despite the difficulties in the absolute calibration procedure, the noise temperature of the receiver system for Z=0 line can be measured assuming that the vacuum window does not contribute much to the total receiver noise. The window transmission properties are presented in annex C.

4.6.1 Noise temperature measurements using the Y-method

Any resistor generates noise due to electron thermal motion. The noise power is proportional to the temperature. The temperature of a terminator (resistor) that would deliver the same noise power as the receiver is called the equivalent receiver noise temperature. The noise temperature can be expressed in K, eV or dB (0 dB corresponds to T=290 K). Another receiver characteristic is the noise figure, which is defined as: $F = P_{out}/GP_{in}$, where G is the receiver gain, P_{in} and P_{out} the noise power at the input and output of the receiver. Normally F is given in dB.

Usually the receiver noise temperature is measured by the Y-method [12]. Two black bodies at known temperatures (T_1 and T_2) are used to illuminate the antenna (one at the time). The measured powers are: $P_1 = k_B(T_1 + T_r)BG$, $P_2 = k_B(T_2 + T_r)BG$, where B is the channel bandwidth, G the gain and T_r the receiver noise temperature. The Y-factor is defined as:

$$Y = \frac{P_1}{P_2} = \frac{T_1 + T_r}{T_2 + T_r}$$

One can easily find that

$$T_r = \frac{T_1 - YT_2}{Y - 1}$$

In the receiver noise temperature measurements on TCV, Eccosorb (a material with a very high absorption of RF waves) was used as a black body. The known temperatures were the room temperature (293^0 K) and the liquid nitrogen boiling temperature (77 ^{0} K).

To illuminate the antenna by the two sources alternatively, a mechanical chopper rotating at $f \sim 1$ kHz was used (fig. 4.12). Since the noise power at the room temperature is much lower than the noise level generated by the receiver, coherent averaging of chopped signal is necessary. A lock-in amplifier was used for this purpose. The receiver noise temperature, including the transmission line, except for the vacuum window, was measured for each channel and found to be about 14 eV (see fig. 4.13).

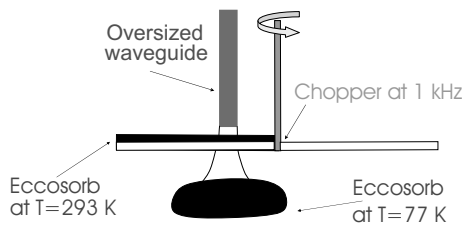

Figure 4.12: *The scheme illustrating the receiver noise temperature measurement by Y-method.*

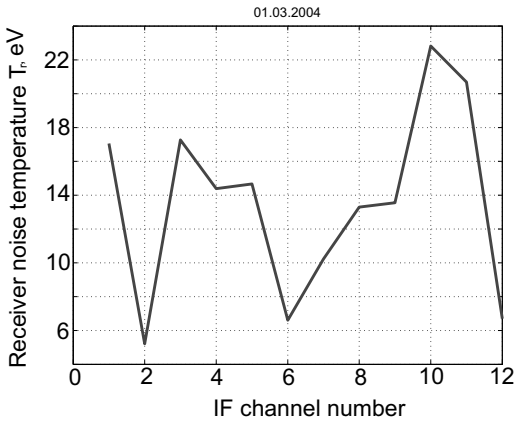

Figure 4.13: *The receiver noise temperature measured by Y-method.*

4.6.2 Relative calibration using magnetic field ramp-up

A relative calibration of the ECE radiometer can be done using the plasma as a noise source, and assuming that the temperature is constant on each magnetic flux surface [15].

The simultaneous ramp-up (ramp-down) of the toroidal magnetic field and plasma current moves EC resonances to the LFS (HFS), while the q-profile does not change, which means that the sawtooth inversion radius (sawtooth instability is described in Chapter 7) remains unchanged. This way, considering a pair of ECE channels, with resonances located symmetrically about the plasma center (one on the LFS, the other on the HFS) and equally close to the sawtooth inversion radius, one can easily find the relative calibration factor for the two channels, because they must measure the same temperature at that time.

The moment when two channels are located symmetrically about the plasma center is defined by a minimum of the oscillations of the ratio of the two channels (see fig. 4.14). These oscillations are due to sawteeth: the bigger phase shift between the channels, the bigger the amplitude of the oscillations.

If the change of the toroidal magnetic field is sufficient, most ECE channels cross the plasma center and can be calibrated with respect to some other

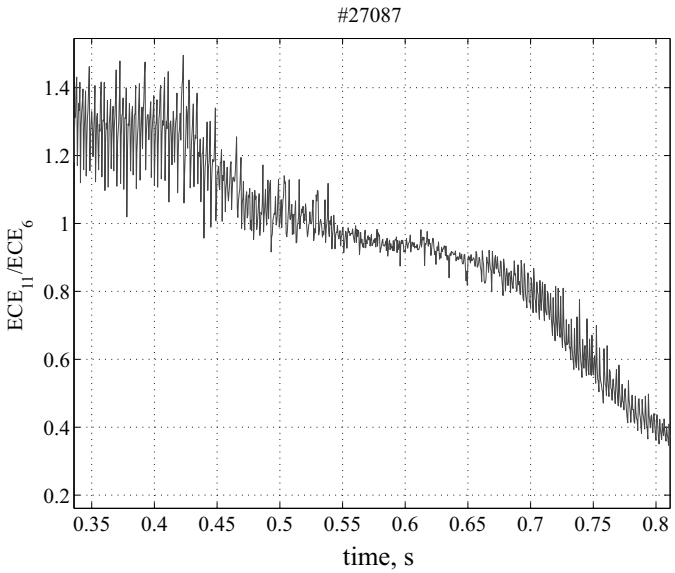

Figure 4.14: *The ratio of two ECE channels during magnetic field ramp-down. The decrease in oscillation amplitude at t=0.55 s corresponds to the moment when the channels are symmetric about the center of plasma.*

channel. By combining the results of all the pairs one can find the relative calibration for all the channels.

The main advantage of this method is the potentially achievable very high accuracy ($\sim 1\%$ on JET, [15]) due to the fact that plasma as a noise source is very hot compared to sources normally used for the absolute calibration, and provides a large signal to noise ratio. Another advantage is that in practice this calibration can be done quite often (every week if needed). Nevertheless, it is not an absolute calibration, which is needed anyway to obtain the temperature.

On TCV, the accuracy of the calibration between two channels was not very high (1-5%, typically 5%). Apparently the main reason for this is a relatively poor spatial resolution in the vertical direction (beam size) compared to the size of the plasma, resulting in an average of the signal for slightly different sawtooth phases. To overcome this obstacle, installation of the antenna with a smaller poloidal spot size is planned.

4.6.3 Cross calibration using Thomson scattering

After every shot the ECE profiles are cross-calibrated using the electron temperature profiles obtained from the TS diagnostics (see Chapter 2 for more details about TS system on TCV). Since TS and ECE have different geometry (the TS laser beam is vertical while the ECE beam is horizontal) both temperature profiles are mapped on the ρ coordinate, i.e. the square root of the normalized poloidal magnetic field flux. A reconstruction of the magnetic equilibrium is therefore needed (see Chapter 2). The ohmic phase during the plasma current flattop is considered for the cross-calibration. Most ECE frequencies are optically thick during the current flattop. For mapping ECE profiles the cold resonance condition is used. Typically the actual (thermal) resonance for the LFS ECE is shifted to the HFS by a few millimeters. The method proved to be reliable when the plasma parameters and the magnetic equilibrium do not change significantly during the cross-calibration phase on a time much faster that the temporal resolution of the Thomson scattering system (50 ms).

4.7 Overview of conventional ECE measurements

Typical TCV signals and measurements illustrating conventional applications of the ECE radiometer will be presented.

4.7.1 MHD oscillations

A discharge (#24736) with large amplitude temperature fluctuations due to Magneto-Hydro-Dynamic (MHD) activity is shown in fig. 4.15. At the top of the figure the traces of plasma current, line average electron density, injected ECH power, perturbations of the magnetic field at the edge and electron temperature at $\rho = 0.72$ are presented. At the end of the shot the small displacement of the plasma destabilizes an m=2 mode. At the bottom of the figure, the Mirnov signal [16] and ECE temperature are plotted on a fast time scale. The ECE time trace and amplitude growth are in agreement with the Mirnov coils data. The ECE signals allow a determination of the island width, its radial location and the associated temperature drop (7 cm, $\rho = 0.72$ and 500 eV, respectively, for this example).

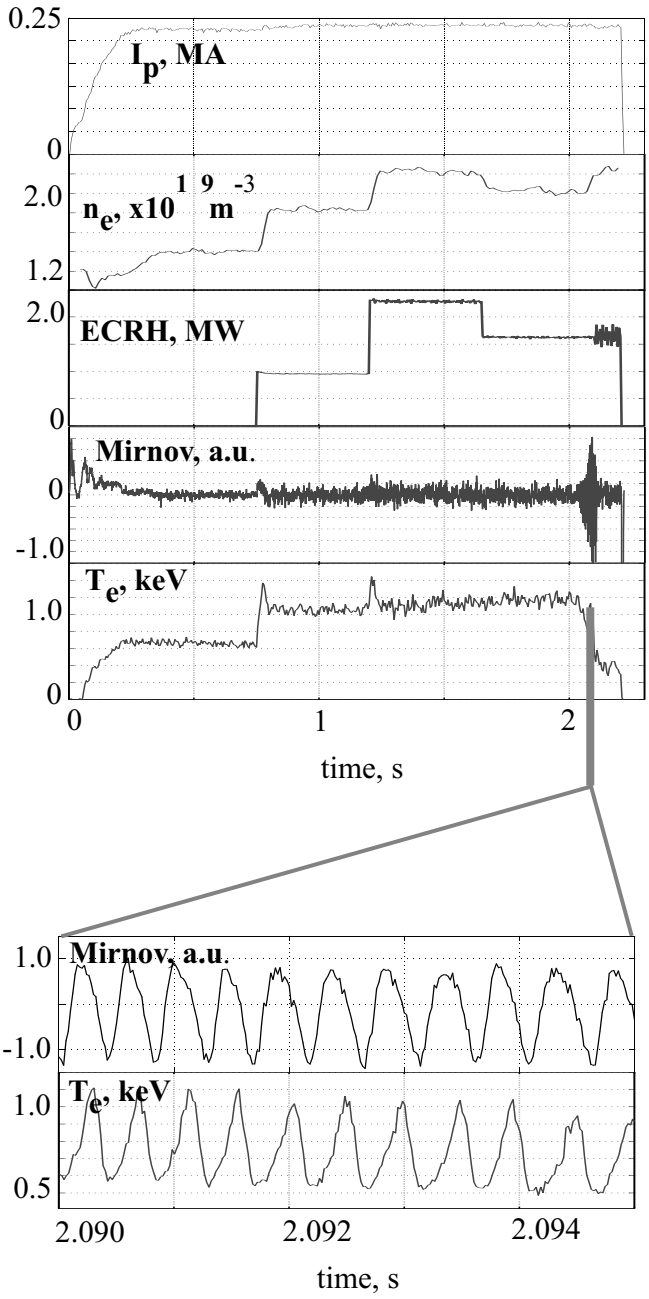

Figure 4.15: *Shot #24736: plasma current, average electron density, ECH power, Mirnov coil signal and electron temperature at* $\rho = 0.72$*;* $f = 71.1$ *GHz. At* $t = 2.09 - 2.095$ *s temperature oscillations due to m=2 MHD mode along with the Mirnov coil signal.*

4.7.2 Auxiliary heating and fast temperature variations

The fast temperature response to central ECH is shown in fig. 4.16. Three gyrotrons generating 0.5 MW in total doubled the electron temperature compared to the ohmic phase. The three temperature drops appearing during the ECH phase are caused by hydrogen puffs. They are not resolved by TS.

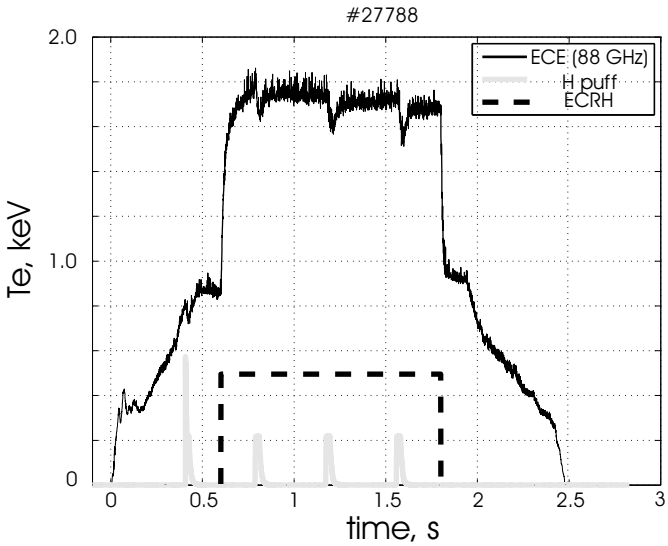

Figure 4.16: *ECH trace. The ECE response to the applied ECH power. Three drops during ECH phase are caused by hydrogen puffs.*

4.7.3 Sawtooth crashes

A typical sawtooth crash (see Chapter 7) during the ohmic phase of a TCV discharge is shown in fig. 4.17. The two time traces at the top show the electron temperature evolution, (a) - inside and (b) - outside the inversion radius. The corresponding temperature profiles measured by LFS ECE, (1) - before the sawtooth crash, (2) - after the crash, are also shown. Unlike TS [17], the LFS ECE can provide detailed temperature profile evolution at each crash. The HFS ECE system does not cover both HFS and LFS inversion radii.

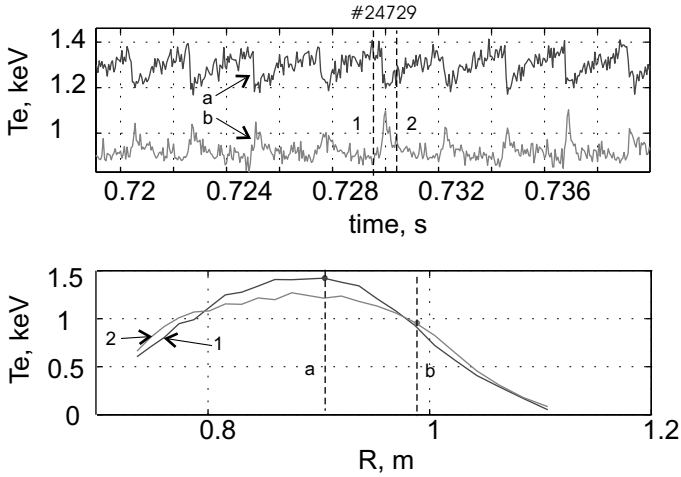

Figure 4.17: *Sawtooth crash. Two ECE time traces (a-inside, b-outside the sawtooth inversion radius) and two profiles (1-before the crash, 2-after the crash).*

4.7.4 Non-thermal electrons

In plasmas with a substantial suprathermal electron fraction, the LFS and HFS radiometers can provide qualitative and quantitative information about the Electron Distribution Function (EDF). The LFS and HFS radiometers provide complementary information due to the asymmetry of the ECE spectra emitted in the opposite radial directions. Moreover, the HFS radiometer partially covers the third harmonic ECE frequency range, which provides additional information on the suprathermal population.

On TCV non-thermal electrons are normally created by ECCD [4]. Depending on the density and energy spectrum of the non-thermal electrons, ECE may provide information on the bulk plasma temperature or on the non-thermal population.

The LFS ECE is less sensitive to the presence of fast electrons than the HFS ECE. To find out experimentally when the ECE signal becomes non-thermal, a discharge with ECCD power ramp (25° toroidal injection angle) has been performed. The ECE profiles corresponding to ECCD powers of 0.6 and 0.9 MW are shown in fig. 4.18.

In the case of 0.6 MW the LFS ECE profile remains thermal, while the HFS

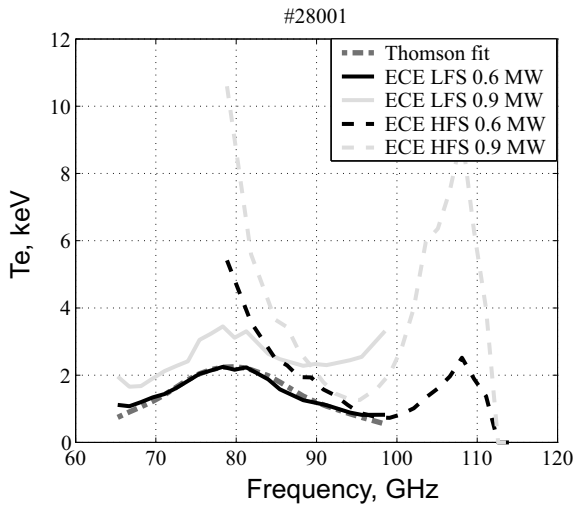

Figure 4.18: *Non-thermal signal during co-ECCD, comparison of the LFS and the HFS ECE. At 0.6 MW ECCD the LFS ECE does not deviate from the TS profile, while at 0.9 MW it does. TS data is mapped to frequency axis assuming second harmonic EC cold resonance.*

ECE profile clearly indicates non-thermal behavior in the plasma center, where most of the non-thermal electrons are confined. Downshifted third harmonic emission is observed in the HFS ECE spectrum at 100-114 GHz, due to low optical depth.

In the case of 0.9 MW both the LFS ECE and the HFS ECE are non-thermal. The changes in the ECE profiles compared to the case of 0.6 MW ECCD indicate higher suprathermal density and temperature in the case of higher power ECCD. For the typical suprathermal temperature on TCV of 20 keV the LFS ECE remains thermal for suprathermal density $n_{st} < 2 \cdot 10^{17}$ m^{-3}, while the threshold for the HFS ECE is $n_{st} \approx 2 \cdot 10^{16}$ m^{-3}.

4.8 Measurements with the steerable antenna

The use of a steerable antenna (fig. 4.19) allows the sweep of toroidal or poloidal (or both) angles during a TCV discharge. The fast sweep of poloidal angle offers a possibility to do ECE tomography. The sweep of the toroidal angle in steady-state regimes can provide information about the electron distribution function in the direction parallel to the magnetic axis of the tokamak. In the high density regimes (above cut-off levels), Electron Bernstein

Emission (EBE) can be measured ([18], [19], [20]). The EBE measurements constitute the main application of the toroidal antenna, as discussed below (Section 4.8.2).

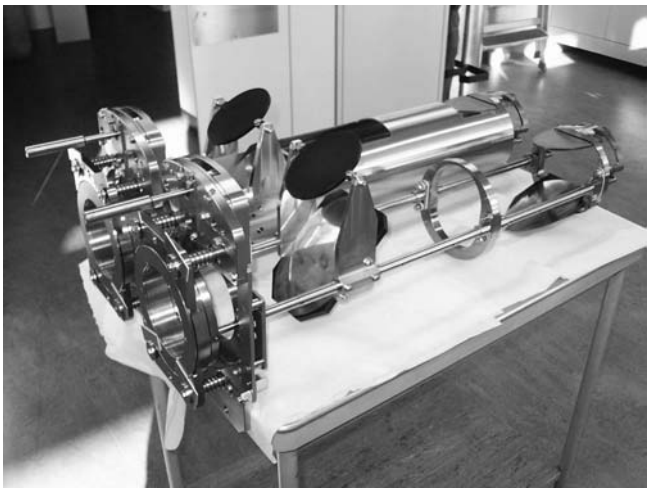

Figure 4.19: *The launcher used as a steerable antenna in the oblique ECE and EBE experiments.*

4.8.1 Oblique ECE

Oblique ECE in low density regimes (below cut-off) allows the study of the EDF due to the Doppler shift effect. The resonance condition for electrons in a warm magnetized plasma can be written as: $m\Omega_{ec} = \gamma\omega(1 - \beta_{\|} cos\theta)$, where m is the harmonic number, Ω_{ec} the fundamental electron cyclotron frequency, γ the relativistic factor, ω the wave frequency, $\beta_{\|} = v_{\|}/c$, $v_{\|}$ the electron velocity parallel to the magnetic field and θ the angle between the wave vector and the magnetic field. The angle is swept during the shot giving the dependence of $\beta_{\|}$ on θ (known) and γ. This offers an opportunity to reconstruct the EDF in the 2D velocity space [21], [22].

Oblique ECE measurements at a fixed toroidal angle have been previously performed on PBX-M ($\phi = 33°$) [21], Tore Supra ($\phi = 25°$) [21] and the FTU tokamak ($\phi = 10°$) [22]. On TCV, oblique ECE measurements have been performed, with the antenna toroidal angle being continuously swept from $\phi = 10°$ to $\phi = 54°$ (see fig. 4.20, bottom panel). The angle scans have been performed during the ECH/ECCD phase of the shot in both co-

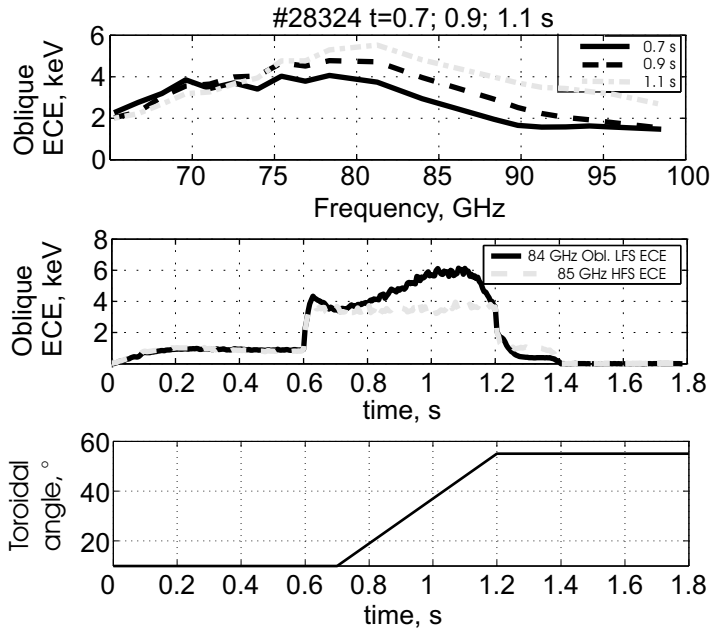

Figure 4.20: *The oblique ECE spectra during the toroidal antenna sweep. Three ECE profiles at $t = 0.7$ s, $t = 0.9$ s and $t = 1.1$ s with corresponding toroidal angles $\phi = 10°$, $\phi = 28°$ and $\phi = 46°$ are shown. The oblique LFS ECE time trace ($f = 84$ GHz), the perpendicular HFS ECE time trace ($f = 85$ GHz) and toroidal antenna angle are also plotted. Counter-ECCD (-30°, 0.9 MW) was applied at $t = 0.6 - 1.2$ s.*

and counter directions. Examples of LFS ECE profiles at several times and one LFS ECE time trace compared to its HFS counterpart are given in the top two panels of fig. 4.20. While the perpendicular HFS ECE spectrum does not change significantly, the oblique LFS ECE spectrum evolves due to the Doppler shift in the resonance condition as the antenna toroidal angle changes. A detailed analysis of those experiments is beyond the scope of this thesis.

4.8.2 Bernstein waves

In high density regimes on TCV, ECE cannot be used to obtain electron temperature because of the plasma cut-off. For the ECE-X2 the critical density depends on the magnetic field amplitude: $n_{crit} = 1.94 \cdot 10^{19} B^2(r)$ m^{-3}, where B is measured in T. Normally, for ECE-X2 in TCV $n_{crit} = 4 \cdot 10^{19}$ m^{-3}, ($B \sim 1.45$ T), while the density in the plasma core can be as high as

$16 \cdot 10^{19}$ m^{-3}. In such regimes, in regions of large density gradients and at some finite angle to the static magnetic field an electromagnetic wave can be converted to an electrostatic wave, which may be subsequently absorbed by the plasma [18]. This way over-dense plasmas can be heated by RF waves at the electron cyclotron frequencies and, in principle, the electron temperature can be obtained by measurements of the mode converted emission in the inverse process. The former is called Electron Bernstein Heating (EBH) and the latter is called EBE.

On TCV the LFS ECE radiometer can be connected to a remotely controlled toroidal antenna, which is used for the study of EBE. For the first EBE measurements the antenna was set to receive elliptical O-mode, which was later converted to linear O-mode. This set-up corresponds to the so-called B-X-O conversion scheme [18] that may take place in overdense plasmas on TCV.

Fig. 4.21 shows the contours of X-O mode transmission calculated by the ART code [23], which suggests that for the density gradients achieved in TCV so far, precise aiming of the receiver's antenna is necessary. The same is true for the EBH experiments, confirming that a real-time steerable antenna is required.

In fig. 4.22 the temporal evolution of the calculated and measured ECE/EBE signal is presented. A clear peak in the ECE intensity is present. Similar measurements made with the orthogonal polarization (elliptical X-mode) show no such peak. This suggests that the measured emission is in fact due to mode converted radiation. The receiver's antenna view in the shot is drawn in fig. 4.21, where two time points, before ($t = 0.9$ s)and after ($t = 1.3$ s) the emission peak are highlighted. Differences between the measured and calculated signal are likely due to uncertainties in the density profile and magnetic equilibrium reconstruction.

4.8.3 ECE tomography

Several discharges in which the poloidal angle was swept were operated on TCV. In order to reconstruct the temperature image one has to perform ray tracing calculations for all the antenna angles during the scan, which is time consuming. Only the optically thick region of plasma should be considered, not only because it is the necessary condition to obtain a measurement of the electron temperature, but also because in the case of optically thin plasma (or if the resonance is outside the plasma) the signal coming from the central

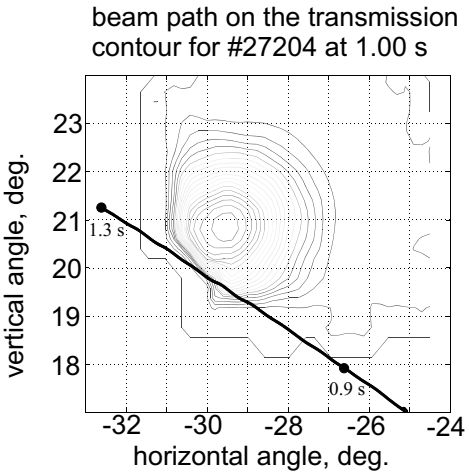

Figure 4.21: *The emission contour calculated by the ART code and experimental antenna sweep trajectory in the shot #27204.*

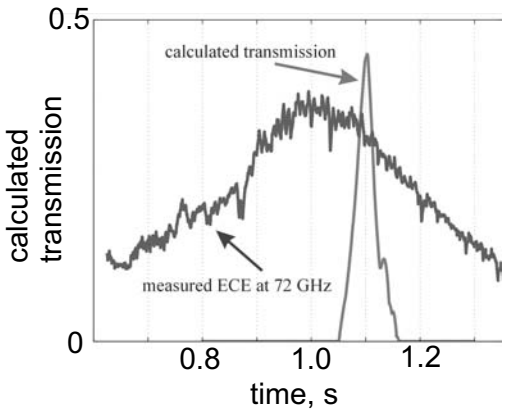

Figure 4.22: *The EBE signal calculated by the ART code and measured in the shot #27204.*

part of plasma and reflected from the wall can dominate. An example of the measured ECE signal during a poloidal antenna sweep is shown in fig. 4.23.

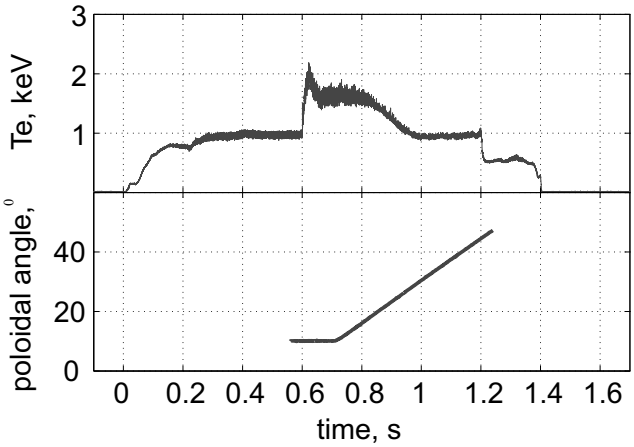

Figure 4.23: *ECE temperature during poloidal angle sweep (shot #28318). ECRH was applied at t=0.6-1.2 s. The ECE level at t=1-1.2 s corresponds to scattered radiation bouncing from the walls.*

Chapter 5

Development of the ECE model

By ECE model we mean the program that calculates the ECE spectrum based on known magnetic field and electron distribution function.

5.1 Motivation

The main application of the ECE model is the simulation of the experimental ECE spectra, which eventually allows the reconstruction of the electron distribution function.

The ECE model is required for all cases in which the measured ECE signal is not proportional to the electron temperature. The most frequent reasons for this are the presence of a significant number of non-thermal electrons, an insufficient optical depth, an ECE beam refraction, Doppler and relativistic shifts.

For example, it is known from experiment that on TCV in low density regimes under ECCD, the HFS ECE profile substantially deviates from the temperature profile measured by Thomson scattering diagnostics. The difference ca be as large as 400%.

5.2 Principal scheme of application of the ECE model

The scheme for the application of the ECE model is illustrated in fig. 5.1. In order to calculate the ECE spectrum one should first calculate the magnetic field structure, the ECE beam path to the receiving antenna and the local emission and absorption for the radiometer frequencies.

The magnetic field is routinely reconstructed on TCV by the magnetic equilibrium code LIUQE [5]. The beam is approximated by the rays, calculated by the TORAY-GA ray-tracing code [24]. Then the only unknown variable, which defines the resulting ECE spectrum, is the EDF.

It is possible to calculate the ECE spectrum based on a hypothetical EDF and compare it with the experimental one. The inverse problem, i.e. the reconstruction of the EDF from the ECE spectrum is ill posed.

The key element of the scheme is the choice of the EDF. It can be any type of distribution function, defined numerically or analytically, based on experimental data and reasonable assumptions. Some examples are given in 5.5.

5.3 WKB approximation

The ECE model uses the WKB approximation (named after G. Wentzel (1926, [25]), H. A. Kramers (1926, [26]) and L. Brillouin (1926, [27])), which assumes that on the scale of a wavelength the properties of the plasma affecting the wave propagation do not change. It is correct to use the WKB approximation for wavelengths short compared to the characteristic scales for the variation of the parameters that influence the dispersion relation, if there is no cut-off or resonance.

The wave in the plasma is assumed to propagate along a ray trajectory that can be calculated from the ray equations using the local dispersion relation. The methods working in this approximation are usually called *ray-tracing*, or *eikonal* methods [9].

In the TCV case, the wavelength corresponding to electron cyclotron frequencies are short compared to the plasma characteristic length (minor radius):

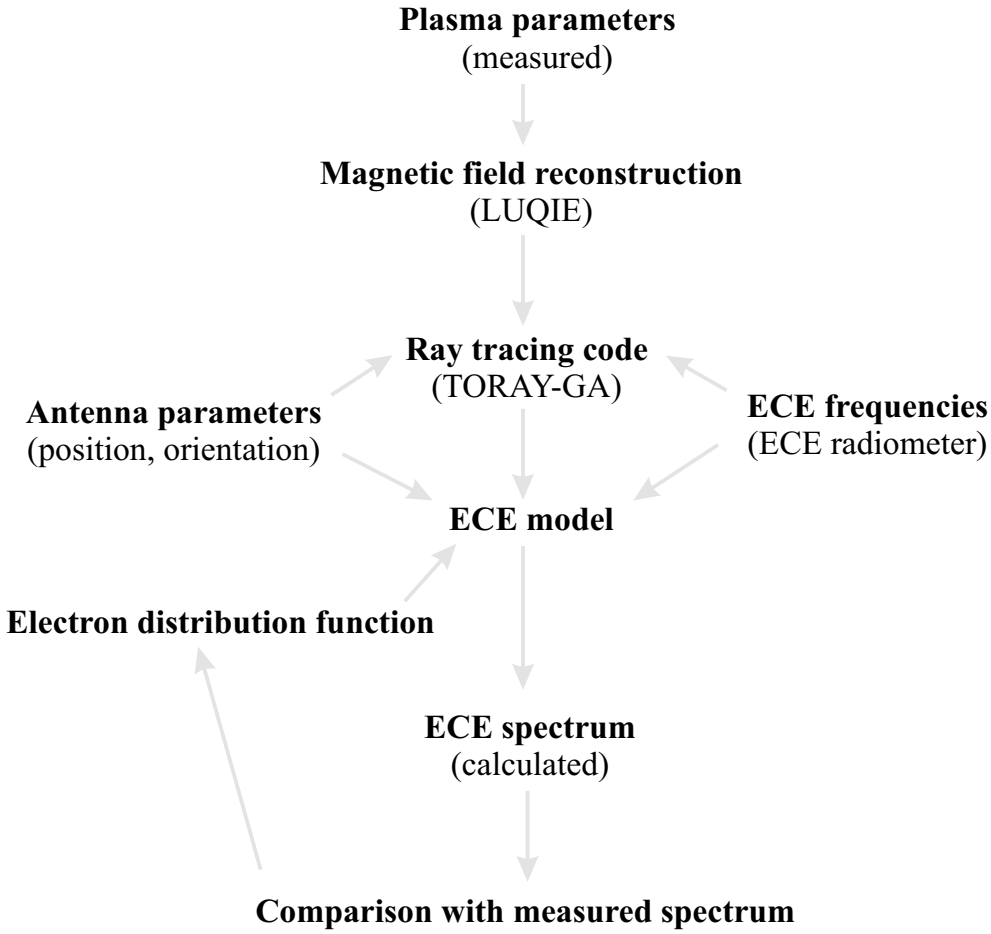

Figure 5.1: *The use of the ECE model.*

0.004 m << 0.240 m. In regimes subject to density cut-off, the ECE model should not be used.

EC resonances are present in all regimes in TCV. Formally, the WKB approach does not work in the region of a resonance. But we can assume that despite the absorption, the ray trajectory remains unchanged, or at least that the location of the resonance is calculated correctly.

5.4 Core of the ECE model

5.4.1 Emission coefficient

It was shown by Einstein (1917, [28]) that there are three fundamental processes in photon-particle interaction: spontaneous and stimulated emission and absorption. As a result, a photon can be emitted or absorbed. In this section we talk only about spontaneous emission by a single electron. We will discuss stimulated emission and absorption in the next section.

The emissivity of a free electron moving in magnetic field, i.e. the emitted power per frequency per solid angle is given by [29]:

$$\eta_\omega(\omega, v, \theta) = \frac{e^2\omega^2}{8\pi^2\epsilon_0 c}\sum_{m=1}^{\infty}\left[\left(\frac{cos\theta - \beta_\parallel}{sin\theta}\right)^2 J_m^2(x) + \beta_\perp^2 J_m'^2(x)\right]\delta(y) \qquad (5.1)$$

where

$$x = (\gamma\omega/\omega_{ec})\beta_\perp sin\theta, \qquad y = m\omega_{ec}/\gamma - \omega(1 - \beta_\parallel cos\theta),$$

$\delta(y)$ - Dirac's delta function, $J_m(x)$ - Bessel function, $J_m^{'}(x) = dJ_m(x)/dx$, e - the charge of an electron, ω - emission frequency, m - harmonic number, θ - the angle between the wave vector and the magnetic field (see fig. 5.2), $\omega_{ec} = eB_0/m_0$, $\gamma = 1/\sqrt{1-\beta^2}$, $\beta = v/c$, v - velocity of the electron, c - speed of light, m_0 - rest mass of electron. The emitted radiation is polarized, with the direction of the electric field given by the vector $(-(cos\theta/sin\theta)(cos\theta - \beta_\parallel)J_m(x), \quad -i\beta_\perp J_m^{'}(x), \quad (cos\theta - \beta_\parallel)J_m(x))$. All units are in SI system.

$$m\omega_{ec}/\gamma - \omega(1 - \beta_\parallel cos\theta) = 0 \qquad (5.2)$$

The resonance condition is given by eq. 5.2. As one can see, at a given location the resonance frequency is equal to ω_{ec} or its harmonics only if $\gamma = 1$ and $\beta = 0$. If the kinetic energy of the electrons is non-negligible, i.e. the plasma is not "cold", than the resonance frequency is different from the EC frequency and its harmonics. Due to relativistic increase of the electron mass, the equivalent EC frequency decreases by the factor γ.

A second effect is Doppler broadening. Depending on the electron velocity direction, the resonance frequency can increase or decrease. One can note that for angles close to 90^0 the relativistic shift dominates the Doppler shift.

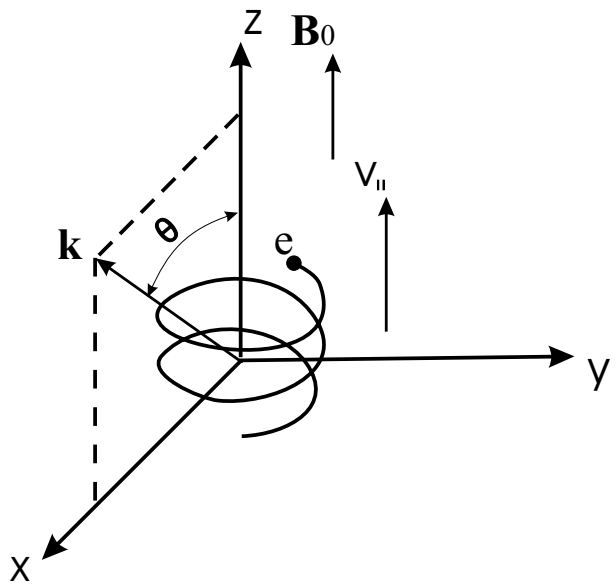

Figure 5.2: *The choice of the coordinates.*

For the radiometer viewing the plasma perpendicularly to the magnetic field and receiving the X-mode, eq. 5.1 can be simplified to:

$$\eta_\omega(\omega, v, \theta) = \frac{e^2\omega^2}{8\pi^2\epsilon_0 c}\sum_{m=1}^{\infty}\beta_\perp^2 J_m'^2(\beta_\perp\gamma\omega/\omega_{ec})\delta(m\omega_{ec}/\gamma - \omega) \tag{5.3}$$

The emission coefficient can be calculated at every point if the electron distribution function is known:

$$j_\omega = \int_0^\infty\int_{-\infty}^\infty \eta_\omega(p_\parallel, p_\perp, \theta) f(p_\parallel, p_\perp) 2\pi p_\perp dp_\perp dp_\parallel \tag{5.4}$$

where $p_\parallel, p_\perp$ are the components of the particle momentum parallel and perpendicular to the magnetic field.

5.4.2 Absorption coefficient

In every point of the plasma where spontaneous EC emission at the angular frequency ω occurs, stimulated emission and absorption also take place. Since both stimulated emission and absorption are proportional to the number of

photons, it is natural to combine them into one coefficient which is called absorption coefficient [29]:

$$\alpha_\omega = -\frac{8\pi^3 c^2}{N_r^2 \omega^2} \int_0^\infty \int_{-\infty}^\infty \eta_\omega(p_\parallel, p_\perp, \theta) \times \\ \left[\frac{\epsilon}{c^2} \frac{\partial f}{\partial p_\perp} - N(\theta) cos\theta \left(\frac{p_\parallel}{c} \frac{\partial f}{\partial p_\perp} - \frac{p_\perp}{c} \frac{\partial f}{\partial p_\parallel} \right) \right] 2\pi dp_\perp dp_\parallel \tag{5.5}$$

In eq. 5.5 $N = (k/\omega)c$ is the local refractive index of the plasma and N_r is the ray refractive index. N_r is proportional to the group velocity and approximately equal to the real part of N if the medium is not strongly anisotropic [29]:

$$N_r^2 = \left| N^2 \ sin\ \theta \frac{\left[1 + \left(\frac{1}{N} \frac{\partial N}{\partial \theta} \right)^2 \right]^{1/2}}{\frac{\partial}{\partial \theta} \left\{ \frac{cos\theta + \frac{1}{N} \frac{\partial N}{\partial \theta} sin\theta}{\left[1 + (\frac{1}{N} \frac{\partial N}{\partial \theta})^2 \right]^{1/2}} \right\}} \right| \tag{5.6}$$

In our model the integration over $(p_\parallel, p_\perp)$ is replaced by an integration over (p, Θ), where $p_\parallel = p \cdot cos(\Theta)$, $p_\perp = p \cdot sin(\Theta)$. Using the expression for a delta function of another function

$$\delta[g(x)] = \sum_i \frac{\delta(x - x_i)}{|g'(x_i)|},$$

where x_i are the roots of $g(x)$, one gets for the (p, Θ) coordinates:

$$\delta(m\omega_{ec}/\gamma - \omega(1 - \beta_\parallel cos\theta)) = \delta(\Theta - \Theta_{res}) \frac{c\ m_0 \gamma}{\omega p\ sin\Theta_{res}\ cos\theta},$$

where $cos\Theta_{res} = (\gamma\omega - m\omega_{ec})/(\gamma\omega\beta\ cos\theta)$, $\quad \gamma = \sqrt{1 + p^2/(m_0 c)^2}$.

Obviously, Θ_{res} is a function of p and the real space parameters ω, ω_{ec} and θ. The radiometer used in the experiment defines ω, which is a constant in our calculations. The EC frequency ω_{ec} depends only on the magnetic field and can be found from the magnetic equilibrium reconstruction. The angle

between the wave vector and the magnetic field depends not only on plasma parameters, but also on the antenna position and orientation. To calculate θ in cases more involved than the ray passing through the center of the plasma perpendicular to the magnetic field, a ray tracing code is needed (see 5.4.4).

Therefore we have a resonance curve in momentum space (p, Θ) defined by plasma and diagnostic parameters. To calculate the emission and absorption coefficients we integrate over p along this curve. Since the emissivity and the resonance condition depend on the harmonic number, the contribution for each harmonic must be calculated separately. Usually we consider $m = 2$, $m = 3$ and $m = 4$, and we find that the contribution from $m = 4$ is negligible.

5.4.3 Refractive index

In order to calculate the absorption coefficient using eq. 5.5 we need to know the refractive index of the plasma. Being solved correctly for an arbitrary electron distribution function the refractive index can directly give an absorption coefficient. Unfortunately, this is a difficult task (Chapter 3) and it could not be undertaken as part of the present work.

Therefore we have to use one of the approximations, such as the cold plasma approximation or the weakly relativistic approximation.

The cold plasma approximation is the easiest solution, as it leads to a quadratic equation in N^2 (3.13). The solution for given cyclotron frequencies, plasma frequencies and θ angle is easy to find. The disadvantage of this method is that the thermal movement of the particles is disregarded. As a result, the refractive index is quite different from the one corresponding to a hot plasma in the vicinity of the EC resonance. However, the ECE spectrum obtained with a cold refractive index is not very different from that obtained with a hot refractive index, because the main contribution from the electron motion comes into eqs. 5.4, 5.5 via the electron distribution function and its derivatives. Hence, the cold plasma refractive index can be used in the ECE spectra modelling as a first approximation.

The weakly relativistic approach uses small Larmor radius (compared to wavelength) and low electron temperature (compared to electron rest mass) expansions. There exist relatively easy formulas to calculate the corrections to the cold plasma solution for frequencies close to the second harmonic

resonance in the case of perpendicular propagation [30]:

$$N_\perp^2 = \frac{-(1+b) \pm \sqrt{(1+b)^2 + 4aN_{\perp,cold}^2}}{2a}, \tag{5.7}$$

where

$$a = -\frac{1}{2}(\frac{\omega_{pe}}{\omega_{ec}})^2 \frac{\omega^2 - \omega_{ec}^2}{\omega^2 - \omega_{ec}^2 - \omega_{pe}^2} F_{7/2}(z_2), \quad b = -2(1 - \frac{\omega_{pe}^2}{\omega(\omega + \omega_{ec})})a.$$

The function $F_q(z)$ used in eq. 5.7 is known as Shkarovski function and was introduced by Y.N. Dnestrovsky [31]:

$$F_q(z) = -i \int_0^\infty \frac{d\tau}{(1 - i\tau)^q} e^{iz\tau}.$$

This method is very useful to estimate the inaccuracy of the cold plasma approach. However this method gives a limited accuracy for a high electron temperature and high wave frequency, and it assumes a maxwellian distribution, while we are interested in regimes with a strong non-thermal population.

A more accurate method consists in a fully relativistic formulation [32]. The code that uses this approach has been developed for TCV by E. Nelson-Melby [33]. For typical shots of interest the result is only a few percent different from the weakly relativistic one. Again, one should note that the code assumes an isotropic maxwellian distribution. The drawback of a fully relativistic code compared to weakly relativistic formulas is the calculation time. It takes several minutes to calculate the refractive index in one point for a single frequency (on Sun UltraSparc 2). Since we calculate hundreds of points along the ray pass for each frequency, it would take more than a week to simulate a single ECE profile. Therefore, frequent usage of the fully relativistic refractive index is nearly impossible in practice.

5.4.4 Ray tracing

In a case where the antenna looks perpendicular to the magnetic field at the center of the plasma, one can assume that the ray goes straight through the center of the plasma. In all other cases refraction due to electron density gradients bends the ray trajectory and ray tracing calculations are needed.

If $g(\mathbf{k}, \omega, \mathbf{r}, t) = 0$ is the local dispersion relation, we can write a set of equations [34]:

$$\frac{d\mathbf{r}}{ds} = \frac{\partial g}{\partial \mathbf{k}}, \quad \frac{d\mathbf{k}}{ds} = -\frac{\partial g}{\partial \mathbf{r}}, \quad \frac{dt}{ds} = -\frac{\partial g}{\partial \omega}, \quad \frac{d\omega}{ds} = \frac{\partial g}{\partial t}, \tag{5.8}$$

where s is a measure of the position along the ray trajectory. For the cold plasma dispersion relation, the final set of equations may look easy to solve. However, there are numerical problems. Doing many iterations while calculating the ray trajectory the solution may become unstable to numerical errors, the step size can be too long in the region where strong refraction occurs or too short resulting in a non-self-consistent solution. It is even more difficult to get a reliable ray-tracing code for a hot plasma dispersion relation.

In order to avoid numerical problems we decided to use the well known ray-tracing code TORAY-GA [24].

5.4.5 Radiation transport

If we define I_ω as the radiated power per unit of surface, of solid angle and of frequency, the balance between the emission and the absorption at each point along the ray is given by [29]:

$$N_r^2 \frac{d}{ds}\left(\frac{I_\omega}{N_r^2}\right) = j_\omega - \alpha_\omega I_\omega, \tag{5.9}$$

where d/ds denotes derivation along the ray. Eq. 5.9 is called the *equation of transfer*. Before we calculate the emergent radiation we define the *source function* S_ω and the *optical depth* τ.

$$S_\omega = \frac{1}{N_r^2}\frac{j_\omega}{\alpha_\omega} = \frac{\omega^2}{8\pi^3 c^2} k_B T_r, \tag{5.10}$$

where k_B is Boltzmann's constant and T_r is the so-called *radiation temperature*. In the case of a maxwellian distribution, the source function gives the power equal to the emission of the black body with a temperature T_r.

$$d\tau = -\alpha_\omega ds, \qquad \tau = \int_0^\tau d\tau = -\int_l^s \alpha_\omega ds, \tag{5.11}$$

In eq. 5.11 l is the length of the ray in the plasma. The optical depth τ is a very important integral plasma characteristic for ECE applications. It depends on the frequency and is measured backward along the ray. If τ is sufficiently large, then the absorption is high; all the radiation gets absorbed

inside the plasma and it is only a thin layer that is emitting outside the plasma. We can say that plasma emits at certain frequencies as a black body and calculate the emitted power using Planck's law. In practice we say that the plasma is optically thick if $\tau \geq 3$, which corresponds to a 95% absorption.

If we assume that there is no incident radiation and the emitting medium has the same T_r along the ray, the emerging intensity, i.e. the intensity of the radiation leaving the plasma can be written as:

$$I_\omega = \int_0^{\tau_0} S_\omega(\tau) e^{-\tau} d\tau = \frac{\omega^2}{8\pi^3 c^2} k_B T_r (1 - e^{-\tau_0}), \tag{5.12}$$

where τ_0 is the result of the integration (eq. 5.11) along the whole ray.

In a tokamak plasma, the electron temperature and consequently the radiation temperature change along the ray, but the emitting layer is quite narrow (due to the variation of the magnetic field and the high τ values). As a consequence, T_r in eq. 5.12 corresponds to an average temperature of the emitting layer.

Eq. 5.12 illustrate the principle of the ECE diagnostic, which measures a quantity proportional to I_ω. The radiation temperature is proportional to the measured value. To get absolute numbers one should know the calibration coefficients, which depend on the diagnostic set-up. To obtain the electron temperature one has to assume a maxwellian distribution of electrons. In both cases, sufficient optical depth is necessary.

5.4.6 Summary

In 5.4.1-5.4.5 the necessary steps to calculate the ECE spectrum are described. As indicated at the beginning of this Chapter, it is sufficient to know the magnetic field and the electron distribution function to calculate the ECE spectrum. The use of the WKB approximation is justified and in practice unavoidable. The inaccuracy in the ray refractive index, caused by the use of analytical approximations, is usually small.

In fig. 5.3 we show an example of the ECE model intermediate values, which are related to the final result of the model, i.e. ECE. The plasma is assumed to be maxwellian. The emission coefficient j, the absorption coefficient α, the optical depth τ are calculated for 80 GHz in plasma with central temperature $T = 2 \cdot 10^7$ K, central density $n_e = 2 \cdot 10^{19}$ m^{-3}. In the ECE model all

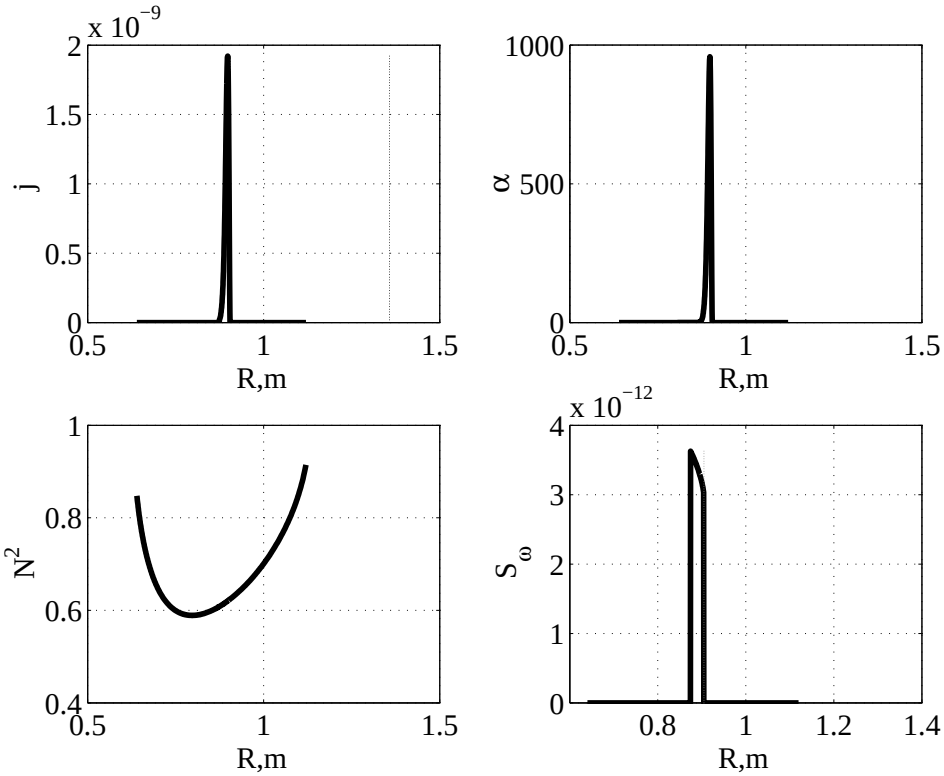

Figure 5.3: *The emission coefficient, the absorption coefficient, the refractive index and the source function calculated for a single frequency. All values are in SI units.*

values are in SI units, that is why we use [K] instead of [eV] for the electron temperature (1 eV=11605 K). This result is a sum of $m = 2$, $m = 3$ harmonics in extraordinary mode (see Chapter 3) for perpendicular propagation.

In fig. 5.4 the first graph shows the optical depth τ calculated from HFS to LFS, thus for HFS ECE reception. The second graph, representing $e^{-\tau}$, gives an idea of the absorption of the hypothetical incident beam. In the last graph, the source function attenuated by the plasma absorption for the HFS detection is shown. This graph allows determination of the location of the emitting spot and its width. As one can see the emitting spot is narrower than the resonance region, and it would be slightly displaced to the LFS for the LFS detection. This effect depends on the temperature and for maxwellian plasma in TCV should not exceed a few millimeters.

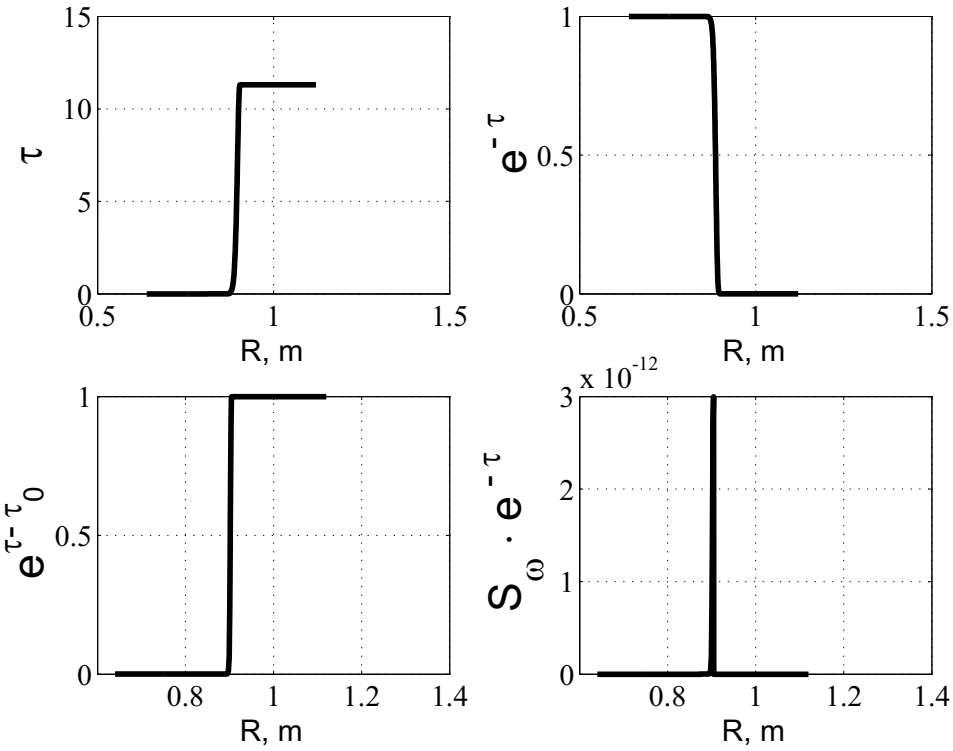

Figure 5.4: *Optical depth is calculated for the HFS detection.* $e^{-\tau}$ *is used in eq. 5.12 and shows the absorption.* $S_\omega e^{-\tau}$ *defines the location of the emission spot visible from the HFS.*

5.5 Distribution function

In this section, three types of distribution functions used for TCV data analysis are described. Other types of distribution functions used in the thesis can be found in Chapter 6 and Chapter 7.

5.5.1 Maxwellian distribution function

The widely used maxwellian distribution has been used to test the ECE model and to check the importance of some effects included in the model. For example there can be a difference in the location of the emission spots between HFS and LFS antennas at high electron temperature.

In this work the EDF is normalized in such a way that its integral over the velocity space is equal to the local electron density. Therefore the maxwellian

distribution is written as

$$f(v) = n_e \left(\frac{m_e}{2\pi k_B T_e}\right)^{3/2} exp\left(-\frac{m_e v^2}{2k_B T_e}\right). \tag{5.13}$$

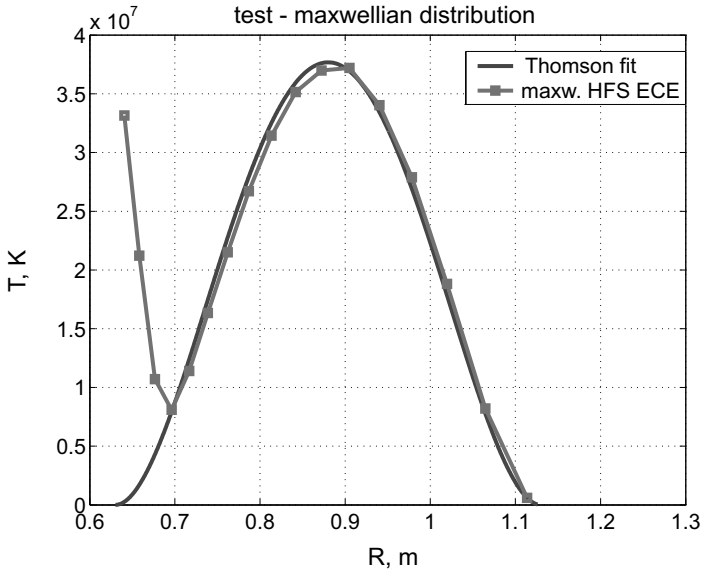

Figure 5.5: *The ECE spectrum calculated for HFS detection, using a maxwellian distribution function. The deviation of the ECE temperature at the HFS is due to the third harmonic radiation coming from the LFS of plasma.*

In fig. 5.5 an example of a calculated spectrum using the maxwellian distribution function is shown. In the region where there is no harmonic overlap ($R \geq 0.7$ m) the HFS ECE gives the electron temperature with a good accuracy.

5.5.2 Bi-maxwellian distribution function

A more probable candidate for the simulation is the bi-maxwellian distribution function, a sum of two maxwellian distributions (eq. 5.14). This approach, allows the existence of a small fraction of electrons, whose energy distribution can be described with a separate maxwellian, having a higher temperature than the bulk plasma.

$$f(v) = (1-\eta) f_b(v) + \eta f_s(v) \tag{5.14}$$

Here f_b is related to the bulk plasma, while f_s corresponds to the suprathermal population. Normally f_b has a lower temperature, $T_b < T_s$, and a higher electron density, $n_b > n_s$.

This kind of distribution function is often suggested by the experimental data, such as the HXR spectrum, which when plotted in semi-logarithmic scale often shows two slopes [4]. This approach works well in low power ECCD regimes when the fraction of non-thermal electrons is small.

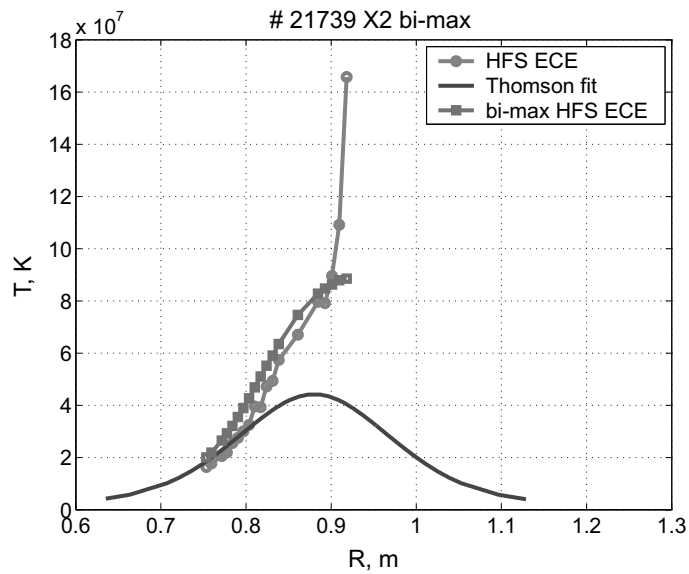

Figure 5.6: *The ECE spectrum calculated for the HFS detection using the bi-maxwellian distribution function, the experimentally measured HFS ECE spectrum and the electron temperature profile from the TS data fit. The simulated spectrum matches the measured one for nearly all frequencies.*

5.5.3 Fokker-Planck code generated distribution function

The evolution of the electron distribution function can be described by the Fokker-Planck (or Vlasov) equation:

$$\frac{\partial f}{\partial t} + \mathbf{v} \cdot \frac{\partial f}{\partial \mathbf{x}} + \frac{e}{m}(\mathbf{E} + \mathbf{v} \times \mathbf{B}) \cdot \frac{\partial f}{\partial \mathbf{v}} = \left(\frac{\partial f}{\partial t}\right)_c \tag{5.15}$$

where $\mathbf{x}$ is the position in the real space, $\mathbf{v}$ the velocity and on the right hand side of the equation there is a collision term [2]. A code which solves the Fokker-Planck equation is called a Fokker-Planck code.

An interesting approach is to use a distribution function calculated by a Fokker-Plank code to calculate the ECE spectrum and compare with the experimental one for a variety of ECRH/ECCD experiments. The CQL3D code [35] was used to calculate the ECE spectra for TCV shots with ECCD-X2. The results are generally satisfactory, particulary in the case of low power ECCD.

Figs. 5.7-5.9 show the results of the simulation of shot #21739 at $t = 0.5$ s when 0.25 MW ECCD were injected into the plasma. The experimental HFS ECE profile deviates from the profile obtained from the Thomson scattering data, indicating the presence of the suprathermal electrons.

CQL3D was used to calculate the distribution function for three values of the radial diffusion coefficient for electrons: $D = 0.1$ m^2/s, $D = 1$ m^2/s and $D = 10$ m^2/s. If confinement is assumed to be high (low diffusion coefficient, fig. 5.7) the fast electrons stay near the plasma center where they are generated. As one can see, the thermal part of the HFS ECE profile ($R \leq 0.8$ m) is well reproduced. However for more central frequencies ($0.8 < R \leq 0.9$ m) the discrepancy is not negligible.

In case of poor confinement (high diffusion coefficient, fig. 5.9) the simulated profile is much broader and the shape of the profile is similar to the experimental one. However, the simulated profile suggests the existence of non-thermal electrons at ($0.75 < R \leq 0.8$ m), which contradicts the experimental data (HFS ECE does not deviate from the TS data).

In the intermediate case of $D = 1$ m^2/s, which is normally used for modelling this type of discharge, the result is not better than in the previous two cases.

Note that for every parameter change, such as the diffusion coefficient, one has to rerun the Fokker-Planck code, which takes several hours. Therefore, if we simply want to find the distribution function that matches the experimental data, this method is not very efficient.

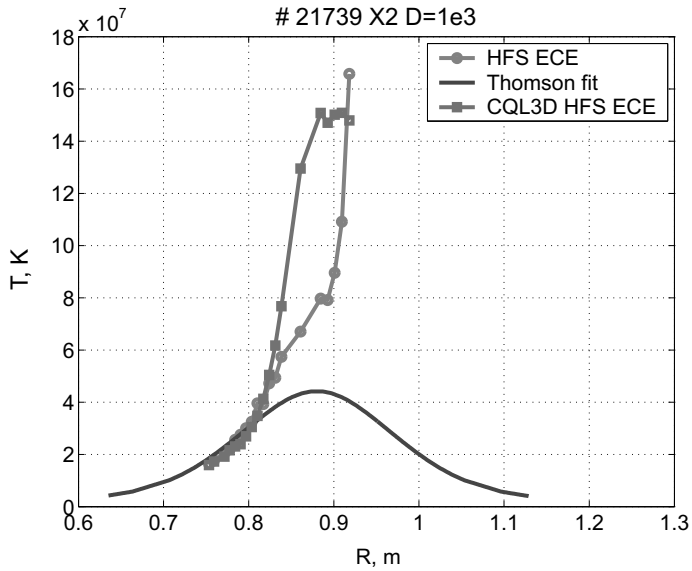

Figure 5.7: *The experimental ECE HFS profile, the TS data fit and the ECE spectrum calculated for the HFS detection, using the CQL3D distribution function ($D = 0.1\ m^2/s$).*

5.5.4 Trapped particles effect

It is generally assumed that the plasma parameters, such as density and temperature, are the same on the same flux surface. But the electron distribution function actually varies along the same flux surface due to the poloidal asymmetry of the magnetic field in a tokamak. This effect is taken into account in the ECE model. The distribution function is usually defined for the outermost point of the flux surface where the magnetic field is minimum. Then it is recalculated for the regions with the higher magnetic field using the conservation of the magnetic moment (first adiabatic invariant, eq. 5.16).

$$\mu = \frac{mv_\perp^2}{2B} = const \tag{5.16}$$

5.6 Implementation of the code

The ECE code is written in MATLAB. It consists of the core file and several supplementary m-files, which read ray tracing and magnetic reconstruction results, define the distribution function or read the CQL3D results and calculate a refractive index.

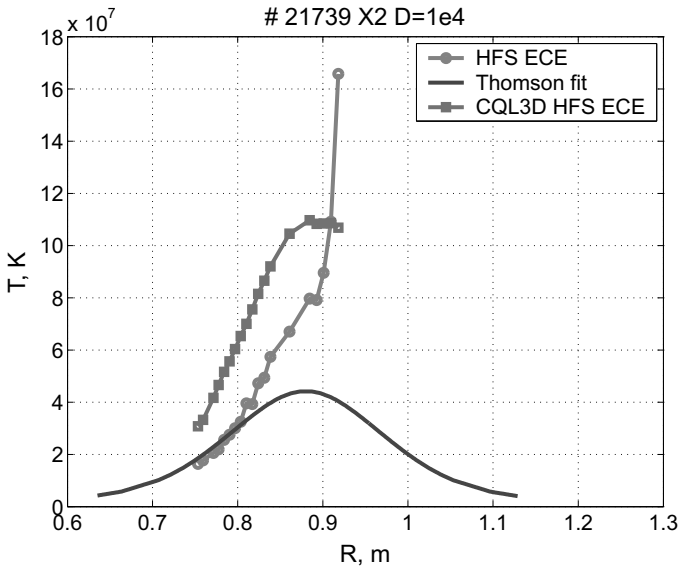

Figure 5.8: *The experimental ECE HFS profile, the TS data fit and the ECE spectrum calculated for the HFS detection, using the CQL3D distribution function ($D = 1\ m^2/s$).*

The grid used for the integration in the real space is not uniform. First the program uses the preliminary rough mesh to find the resonances and then increases the grid density in the resonance regions, where the emission and the absorption at the second and the third harmonics take place.

The grid in the velocity space is built using quadratic accumulation, i.e. the grid density is higher for the lower energies, based on an initial estimate of the temperature.

In order to improve the performance, eventually all calculations are formulated in matrix form. The ECE model is normally run on IBMaix Sirius 4000 machine (up to few GigaFlops available for a single user). The calculation time for a single frequency is a few minutes, depending on the grid and number of users using the machine. Hence, it takes tens of minutes to calculate the whole profile.

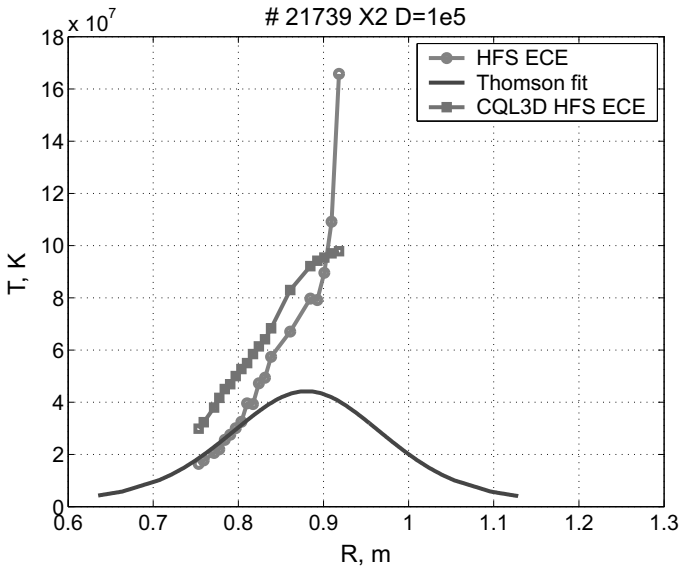

Figure 5.9: *The experimental ECE HFS profile, the TS data fit and the ECE spectrum calculated for the HFS detection, using the CQL3D distribution function ($D = 10\ m^2/s$).*

5.7 Crosschecks and convergence study

The model was tested on maxwellian and bi-maxwellian functions. The results match the analytical formulas. All expected thermal and non-thermal effects are found in the results.

In the velocity space the model converges linearly. This fact is used to estimate the final result using the calculations made on relatively low-resolution grid (up to 100 points for the momentum axis).

In the configuration space, the rate of convergence is faster than quadratic. Starting from 500-600 points, the final result depends only on the grid in the velocity space.

5.8 Further improvements

5.8.1 Partial cut-off

There are regimes in which frequencies corresponding to the LFS edge of the plasma (65-68 GHz), can not propagate across the plasma center because of

the density cut-off. Normally, the ECE model would skip such frequencies because it is impossible to calculate the emission and the absorption along the whole ray. Hence one should not analyze ECE at these frequencies. However, the experimental signal received at the LFS suggest that there is an emission at these frequencies reaching the antenna. Indeed, the cut-off in the center of the plasma does not affect the LFS frequencies viewed from LFS, because all the emission and the absorption occurs at the LFS edge (fig. 5.10). Recent versions of the model deal with such "partial cut-off" situations and calculate the ECE from the part of the plasma not affected by the cut-off.

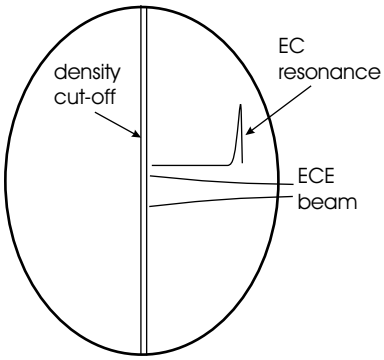

Figure 5.10: *Sketch illustrating the partial cut-off situation. The ECE beam cannot propagate through all the plasma, but the ECE-X2 resonance is still accessible.*

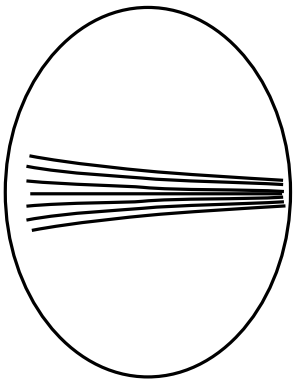

Figure 5.11: *Sketch illustrating the antenna beam. The beam can be considered as a number of rays.*

5.8.2 Antenna pattern

To simulate all properties of the antenna, one should take into account not only its position and orientation, but also the beam width and its divergence. In principle, we can consider the beam as a set of several rays (fig. 5.11). We can treat each ray separately and calculate the sum for the beam, assuming gaussian power distribution across the beam (see Chapter 4, Section 5 for more details). This approach has not been realized so far. In cases where the beam refraction is not too strong, which is normally the case, the antenna pattern does not significantly affect the calculated spectrum.

5.8.3 Scattered radiation

Scattered radiation may be of importance in situations in which the TCV plasma occupies a small part of the vacuum vessel (fig. 5.12). Thus the radiation that is not absorbed by the plasma, for example ECE in vertical direction, can undergo multiple reflections from tokamak walls, being scattered, randomly changing its polarization and filling the part of the vessel where there is no optically thick plasma. This radiation can contribute to the antenna signal, but it is very hard to localize its source. The contribution can be significant in the case of low power mode reception. For instance, a part of the power emitted in X-mode (higher power at second harmonic than in O-mode), being reflected from the wall, can be received in O-mode. Also, when the antenna is not directly illuminated by the plasma, one can get some ECE reflected from the walls.

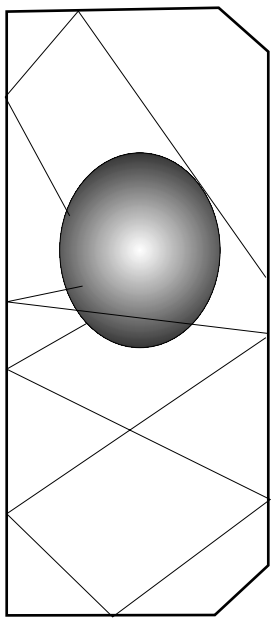

Figure 5.12: *Sketch illustrating scattered radiation filling the vessel.*

In the ECE model, scattered radiation can be added as a fraction of the emitted radiation, disregarding the probability of reabsorption. The effective wall reflection coefficient can be found empirically.

Chapter 6

Reconstruction of the distribution function during strong X2 ECCD and X3 heating

6.1 Motivation (Improved Confinement and ITB)

Under some experimental conditions, the confinement can be improved, leading to better performance of tokamaks. One of the most important topics in tokamak physics research is the study of these Improved Confinement (IC) regimes. IC means that the energy confinement time degrades less with applied heating power than in usual, so-called Low confinement modes (L-modes). The most known scenarios are H-mode [36], [37], [38] and the scenario with Internal Transport Barrier (ITB) [39], [40], [41]. ITB is a narrow radial region with reduced transport and steep radial gradients. Many experiments support the idea that the current profile modification is an essential part of the ITB scenario. The current profile should be flat (the magnetic shear $s = (r/q)(dq/dr)$ is zero) or even hollow (negative magnetic shear) for the ITB to appear. The current profile can be modified by current drive or in the transient phase during ohmic current penetration. Current drive is necessary to achieve a steady-state ITB. ECCD is am effective way to modify the current profile locally and is routinely used on TCV.

In TCV, ECCD power being absorbed in the plasma creates non-thermal electrons. In a simplified way this process can be illustrated as follows.

The RF power injected into the plasma is absorbed by the electrons whose velocity corresponds to the resonance condition (eq. 5.2) for the given point in the configuration space. During this process some electrons gain enough energy to go to collisionless regime. We call them fast electrons. Others will encounter collisions with other particles, losing energy, heating the plasma bulk. As a result, there will be more fast electrons than in the case of thermal equilibrium, and a tail in the EDF will appear.

The absorption of the EC waves is toroidally asymmetric, i.e. electrons moving in one toroidal direction absorb more power than electrons moving in the opposite direction. That is because the electron resonance velocity depends on the wave vector parallel to the magnetic field (eq. 5.2). As a result, a non-inductive current is generated. A significant part of the non-inductive current is carried by the fast electrons. Therefore, the existence of the fast electrons is an essential feature of the ITB formation in TCV. That is why the study of the suprathermal electrons is important for understanding ITB physics.

6.1.1 The TCV diagnostic capabilities for the EDF studies

On TCV there are three diagnostic systems that can provide some information about the EDF: TS, HXR camera and ECE (see Chapter 2). The drawbacks of TS are poor temporal resolution and only perpendicular view, which allows the study of the distribution function only in the direction perpendicular to magnetic field. The same is true for HXR. The ECE system is more flexible, but the interpretation of the data is more involved.

The attempt to reconstruct the electron distribution function has been undertaken in continuous ECCD regime first, because the poor temporal resolution of the TS and the HXR systems is relatively unimportant in this case. Hence complementary information about the EDF is available and the possibility of crosschecks exists. The regime with X2 ECCD + X3 ECH has been chosen because X3 absorption on the bulk plasma is low ($\sim 20 - 30\%$) and can actually be measured by the DML using modulated ECH.

6.1.2 Related analysis previously done on TCV

Attempts to extract information about the EDF have been undertaken on TCV since the HFS radiometer has been installed. The bi-maxwellian ap-

proach has been used in [4].

Using the time-to-peak method the dynamics of the fast electrons during pulsed ECCD has been studied [42] and the importance of the transport of fast electrons has been shown.

6.2 Simulation: from bi-maxwellian to two-slope

6.2.1 An example of a TCV discharge

Shot #18791 was chosen because it has the biggest observed discrepancy between predicted and measured X3 absorption and the bi-maxwellian approach failed to explain anomalously high X3 absorption.

The time evolution of plasma current, average plasma density, injected microwave power, TS electron temperature, radiative temperature from HFS ECE and HXR intensity are plotted in fig. 6.1.

The ohmic phase of the shot lasts till 0.3 s when X2 co-ECCD at toroidal injection angle $\phi = 25°$ starts. From 0.4 s to 0.5 s X3 ECH is applied along with X2 ECCD, while from 0.5 s to 0.7s the X3 power is modulated in order to measure the X3 power absorption.

The HFS ECE shows non-thermal features already at 0.3-0.4 s during the X2 phase, and deviates from the thermal level several times more during the X2+X3 phase. The X3 absorbed power measured by the DML (450-500 kW) corresponds to 100% of the injected power.

As one can see in fig.6.2, the X3 absorption predicted by the TORAY-GA, i.e. calculated for the bulk plasma only, is about 20%. It is concluded that the anomalously high absorption of the X3 power is due to the fast electrons present in this regime.

Several attempts to explain the difference between the measured and the calculated absorption using the bi-maxwellian approach (Chapter 5) have been undertaken [4], [33]. Even using fully relativistic approach [33] and assuming a temperature for the suprathermal population of 25-35 keV, which is 10 times higher than the bulk temperature and 2-3 times higher than the ECE radiative temperature or the HXR photon temperature, and a suprather-

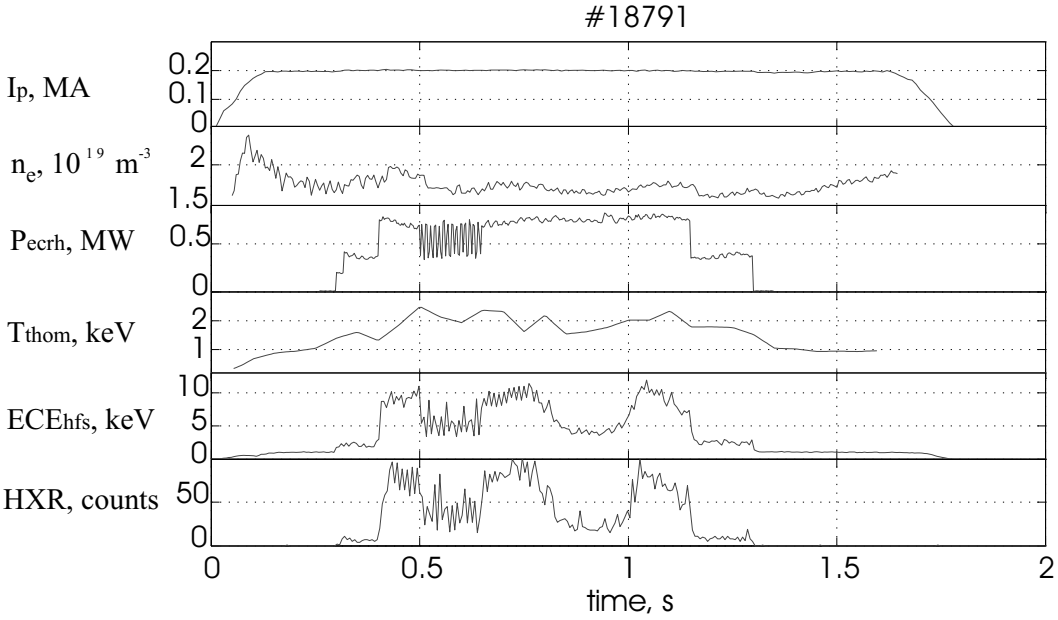

Figure 6.1: *The shot #18791 overview. The time traces of plasma current (I_p), average plasma density (n_e), injected microwave power (P_{ecrh}), TS electron temperature (T_{thom}), radiative temperature from HFS ECE (ECE_{hfs}) and HXR intensity are shown.*

mal density about 20% of the bulk density, the calculated absorption is not higher than 70%. Moreover, such assumptions are far from being realistic because such a suprathermal population would double the energy stored in the plasma and there will not be agreement with experimental data (ECE, HXR). Therefore another approach is needed to describe the EDF evolution during X2+X3 heating.

6.2.2 Two slopes EDF

In this section a new type of EDF, similar to the bi-maxwellian is proposed to reduce the gap between the experimental and calculated X3 absorption. The goal is to build an EDF that would provide high X3 absorption (80-100% in single pass) and good agreement with calculated ECE and HXR spectra, and that the bulk plasma could still be characterized by density and temperature in agreement with TS data.

The two-slope EDF can be defined analogously to the bi-maxwellian (eq.5.14) as:

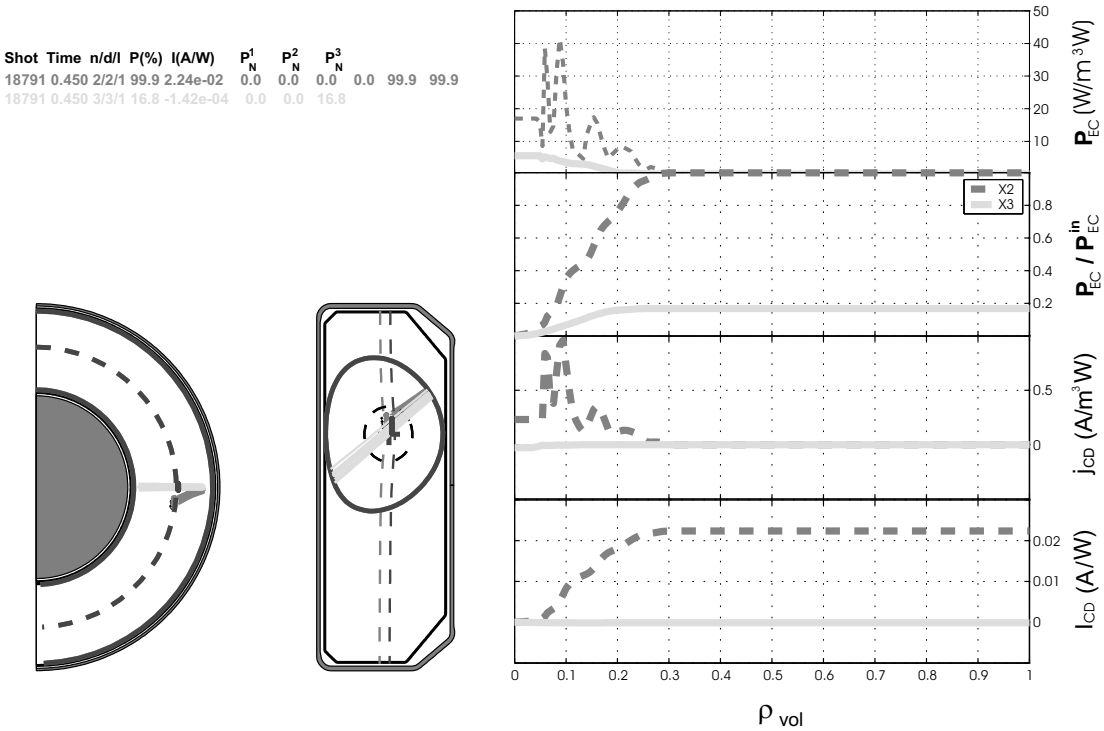

Figure 6.2: *The results of the absorption calculations by TORAY-GA for the X2 and X3 in shot #18791 at 0.45 s.*

$$f(v) = \begin{cases} f_b(v), & v \leq v_k \\ f_s(v), & v \geq v_k \end{cases} \tag{6.1}$$

Here v_k is the velocity which separates the bulk part of the EDF from the non-thermal part in the velocity space.

In fig. 6.3 the comparison of a two-slope EDF with a bi-maxwellian, based on a TCV relevant example, is presented. The transition from the bulk slope to the suprathermal is chosen in the range 7-10 keV, because the lower energies correspond to the TS energy range, while the higher energies are seen by the HXR camera. The lower bi-maxwellian is equivalent to the two-slope EDF in terms of total suprathermal density, but the second slope of this bi-maxwellian EDF is lower. The number of electrons in the second (suprathermal) maxwellian that have low energies ($< 7 - 10$ keV) can easily be 35-50 %. The upper bi-maxwellian EDF is equivalent to the two-slope

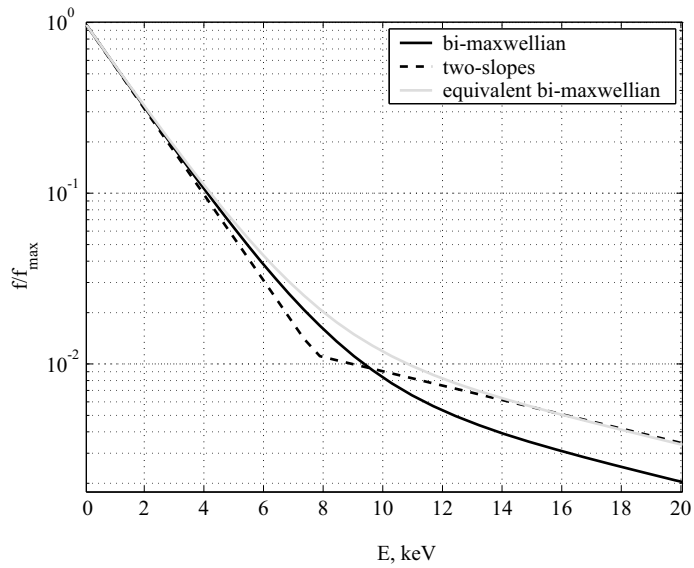

Figure 6.3: *The comparison of the two-slope distribution function (dashed line) with the bi-maxwellian (solid line). The lower bi-maxwellian is equivalent to the two-slope EDF in terms of total suprathermal density, but the second slope is lower. The upper bi-maxwellian EDF is equivalent to the two-slope EDF in terms of matching both slopes, but the total suprathermal density for bi-maxwellian EDF is higher in this case.*

EDF in terms of matching both slopes, but the total suprathermal density for the bi-maxwellian EDF is higher in this case.

6.2.3 Modelling using two-slope EDF

The two-slope EDF has been applied to model the ECE HFS spectrum in shot #18791 and calculate the X3 relativistic absorption using the ECE model (Chapter 5).

The bulk slope is defined by the TS temperature data. The suprathermal slope is defined by the photon temperature from the HXR camera measurements (fig. 6.4). The overall density is defined by the TS density measurements corrected by the FIR density measurements. This way the only unknown parameter is the electron kinetic energy corresponding to v_k, which defines the non-thermal electron density. In our model it can not be less than 7 keV, which means that the number of fast electrons allowed in the model is limited, because the EDF derivative is negative everywhere. The

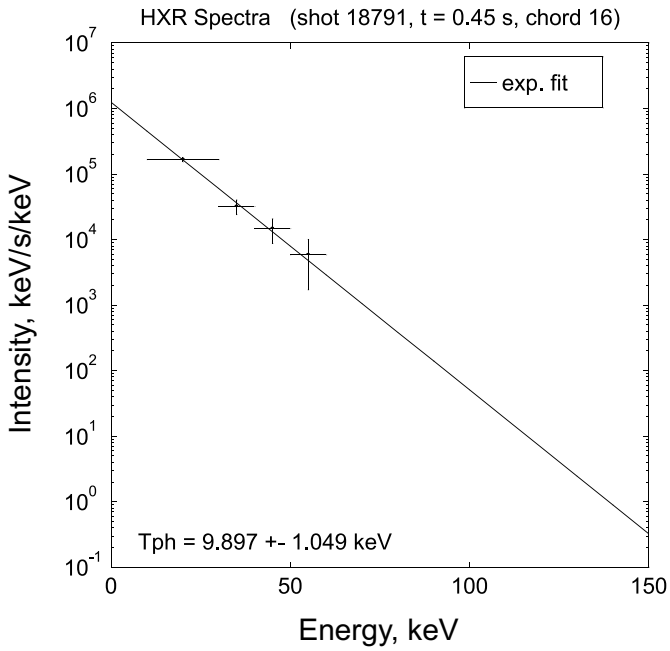

Figure 6.4: *The typical HXR spectrum for the central chord is shown. The measured photon temperature has been used as an estimate of the suprathermal temperature (the second slope of the two-slope EDF).*

latter condition is justified by the fact that no kinetic instabilities have been observed in the experiment. In order to find the suprathermal density profile we model the HFS ECE spectrum. If the simulated HFS ECE profile matches the experimental one, one can also expect that the suprathermal density profile shape is similar to the HXR emissivity profile.

The result of the simulated ECE HFS profile is presented in fig. 6.6. The agreement between the simulated and measured profiles is satisfactory. The simulated ECE HFS profile is not very sensitive to the absolute values of the suprathermal density in the very center ($\rho < 0.2$). The density profile has been chosen as shown in fig. 6.7 not only to match the experimental ECE HFS profile, but to allow at least 80% absorption for the X3 waves. One should note that the shape of the suprathermal density profile is similar to the HXR emissivity profile, which has been obtained from the inversion of the line integrated measurements.

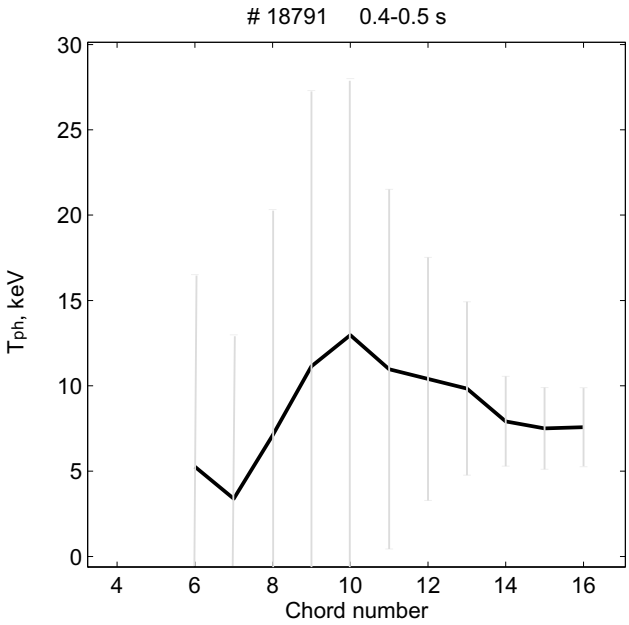

Figure 6.5: *The photon temperature profile from the HXR camera. The photon temperature is approximately uniform across the plasma.*

6.2.4 When results from two-slope and bi-maxwellian approaches are similar

Shot #18971 constitutes an extreme case of discrepancy between the measured X3 absorption and the calculated one for the bulk plasma. In order to simulate the anomalous absorption using the bi-maxwellian model one would need to have the suprathermal fraction about 100%, which would contradict the TS data. However, in other cases where the discrepancy is not that large, the bi-maxwellian approach can be used.

Shot #18782 is similar to shot #18791, but it has a lower X2 injection angle ($-2.4°$) and a lower measured X3 absorption (28%). The results of the simulation of the HFS ECE profile are shown in fig 6.8. The suprathermal profiles for the bi-maxwellian and two-slope EDF are plotted in fig. 6.9 along with the reconstructed HXR emissivity profile shape. The main difference between the two methods is the suprathermal density needed to explain the experimental results. It is always higher in bi-maxwellian case. Since the suprathermal density is less than 10% of the total electron density, both methods can be used. However, the suprathermal density given by the two-

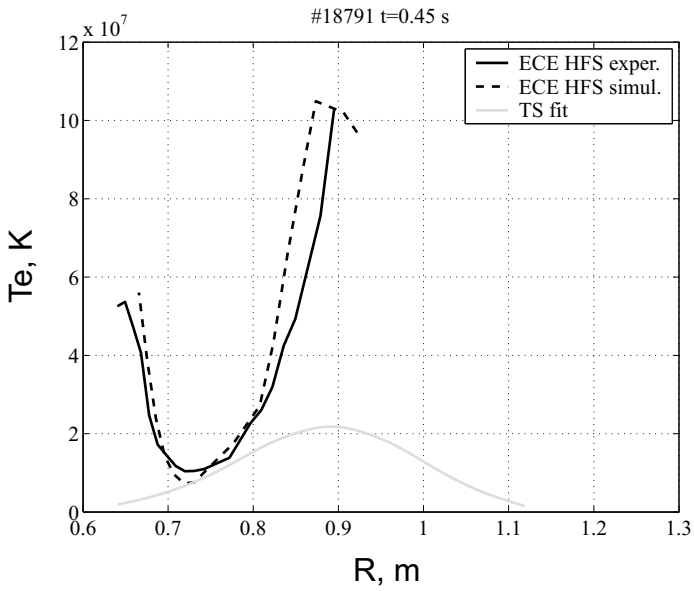

Figure 6.6: *The result of the modelling of the ECE HFS profile (dashed line) along with the experimental one (solid line) and the electron temperature profile from the TS fit.*

slope method is obviously closer to the minimum amount of the fast electrons needed to explain the experimental results.

6.3 Discussion

Using the two-slope EDF based on the experimental results, the simulated ECE HFS profile matches reasonably well the experimental one. At the same time, the calculated absorption of X3 power can reach 80% (shot #18791), not taking into account some smaller effects, such as multiple pass absorption. The local density of the fast electrons is high only in the center of plasma and does not contradict any measurement. The whole number of fast electrons is only 0.4% of the total number, thus the energy stored in the plasma would be only 2% higher than estimated from TS measurements only. The fast electrons profile is peaked in the center because they are generated in this region and are well confined. The HXR emissivity profile is peaked approximately in the same way.

This example shows that when the suprathermal population is not negligible compared to the bulk plasma, the bi-maxwellian approach may fail and

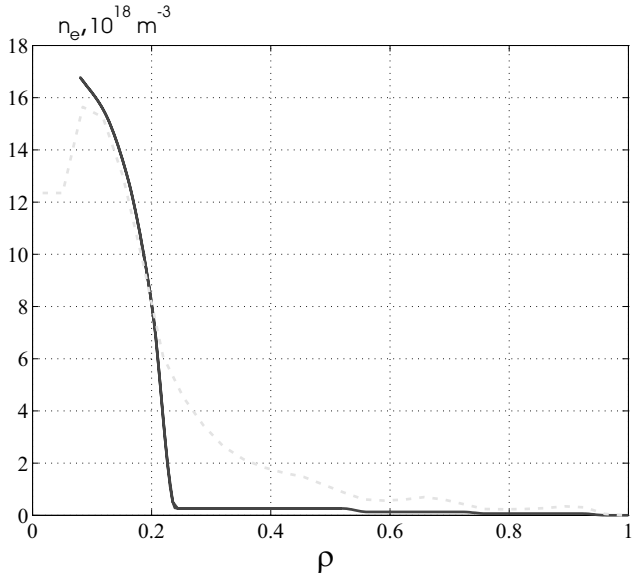

Figure 6.7: *The profile of the non-thermal electrons used in the simulation (solid line) and the reconstructed experimental HXR emissivity profile (dashed line).*

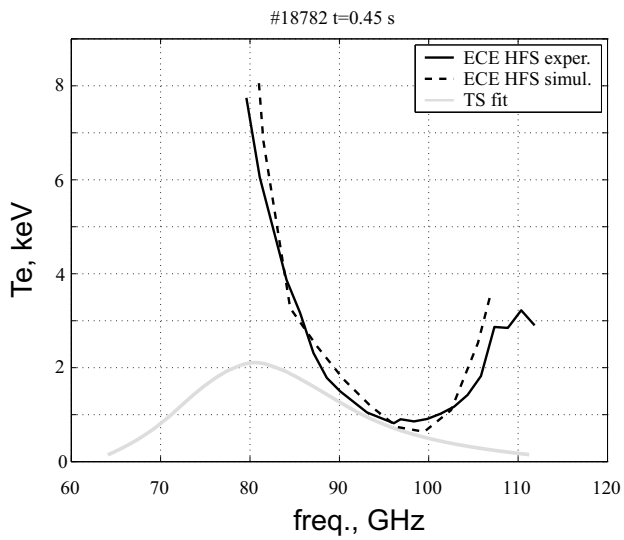

Figure 6.8: *The result of the modelling of the ECE HFS profile (dashed line) for shot #18782 along with the experimental one (solid line) and the electron temperature profile from the TS fit.*

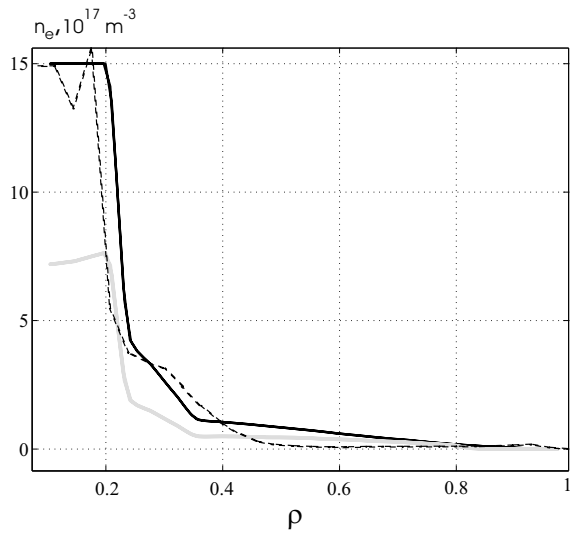

Figure 6.9: *The profiles of the non-thermal electrons used in the simulations (solid lines) for shot #18782: upper curve - the bi-maxwellian EDF, lower curve - the two-slope EDF. The reconstructed experimental HXR emissivity profile (dashed line) is also shown.*

another, more general form for the EDF, such as two-slope EDF, may give better results.

In addition, we can address whether or not the temperature in the plasma core rises to several times that expected for L-mode confinement or whether instead, the presence of non-thermal electrons leads to the overestimation of the plasma temperature and energy? The answer is the following. Even when the absorption properties of the plasma are completely changed due to the existence of a substantial fraction of fast electrons, most of the energy stored in the plasma is still contained in the plasma bulk and therefore the study of the performance of ITB regimes based on TS measurements is justified.

Chapter 7

Fast changes of the distribution function as a result of magnetic reconnection

7.1 Motivation

The term magnetic reconnection indicates a change of topology of the magnetic field in the presence of a plasma [43]. During this process magnetic field lines break and reconnect in different manners. The released magnetic energy can be transformed into kinetic energy, heat or waves in the plasma. Magnetic reconnection occurs around the earth, the sun and other stars, and in laboratory plasmas [43], [44]. A schematic view of two-dimensional (2D) reconnection is shown in fig. 7.1.

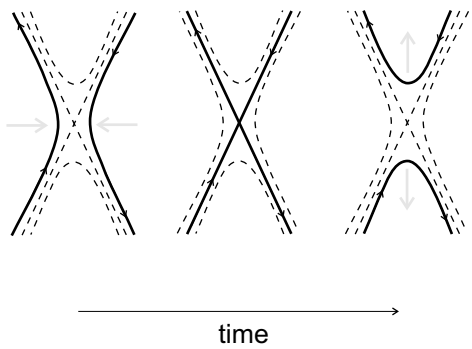

Figure 7.1: *2D magnetic reconnection around an X-point.*

The existing theories of magnetic reconnection do not explain all experimental facts. A major problem is that the observed reconnection time is very short compared to predicted values; often the discrepancy is several orders of magnitude [43]. A second example is that it is not clear what triggers reconnection, i.e. what initiates the topology change by bending and approaching B-field lines.

In tokamaks a well-known example of magnetic reconnection results from sawtooth instability (described in 7.4). In this chapter we consider an important aspect of magnetic reconnection during a sawtooth crash - the acceleration of electrons. The basic questions to be answered are: how many electrons are accelerated and up to what energy.

7.2 Sweet-Parker model of 2D reconnection

A simple model of two-dimensional magnetic reconnection has been proposed by Sweet ([45], [46]) and Parker ([47], [48]), shown schematically in fig. 7.2. We consider a plane region where the magnetic field in the x-direction changes sign at $y = 0$ and has uniform absolute values for $|y| > L_y$. The field lines approach the $y = 0$ line at speed u_y and reconnect. Everywhere except in the region $|y| < L_y$ the magnetic field is assumed to be frozen into the plasma. Then the plasma has to flow away at speed u_x along the direction of the reconnecting field.

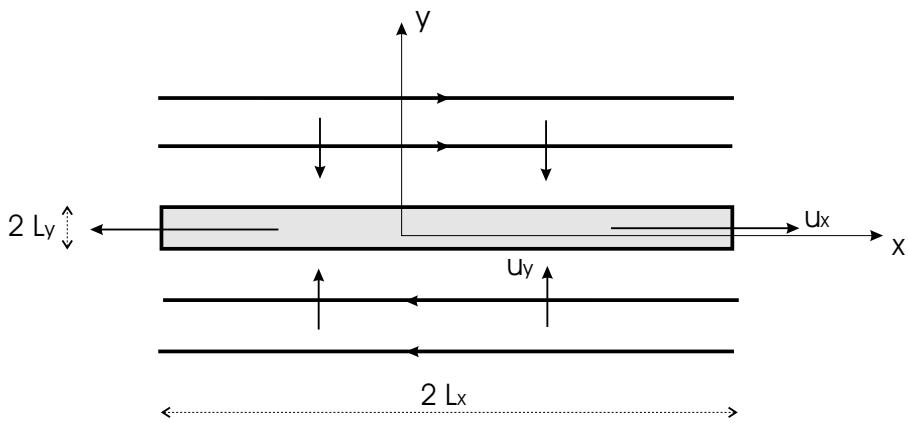

Figure 7.2: *Illustration to the Sweet-Parker model of 2D magnetic reconnection.*

In the reconnection region, where oppositely directed magnetic field lines

meet, a current has to be generated according to Ampere's law:

$$\mu_0 \mathbf{j} = \nabla \times \mathbf{B} \tag{7.1}$$

Thus, the layer where the reconnection takes place constitutes a current sheet. In the center of the reconnection region, where the magnetic field vanishes, from the Ohm's law

$$\mathbf{E} + \mathbf{v} \times \mathbf{B} = \eta \mathbf{j} \tag{7.2}$$

we have $E_z = \eta j_z$. Outside the reconnection region, where the current goes to zero, we have $E_z = u_y B_x$. Assuming conservation of mass $u_y L_x = u_x L_y$ and conservation of energy $B_x^2/2\mu_0 = \rho u_x^2/2$ we have

$$u_x = B_x/\sqrt{\mu_0 \rho} = v_A \qquad u_y = \frac{v_A}{\sqrt{R_m}} \tag{7.3}$$

where v_a is the Alfvén speed and $R_m = \mu_0 L_x v_A/\eta$ is the magnetic Reynolds number. The reconnection time can be estimated as follows

$$\tau_{SP} \sim \frac{L}{u_y} = \frac{L}{v_A}\sqrt{R_m} \tag{7.4}$$

where $L \sim L_x$ is the characteristic length-scale of the region affected by the reconnection. Experimentally observed reconnection times are typically several orders of magnitude shorter than τ_{SP}.

7.3 Dreicer acceleration

The generation of fast particles is one of the main consequences of magnetic reconnection in collisionless plasmas. By fast particles we mean particles whose kinetic energy is at least several times higher than the mean kinetic energy for the same sort of particles in the plasma. Fast particles are present throughout the universe. For example, they are present in cosmic rays and they produce synchrotron radiation in distant galaxies.

Charged particles can be accelerated during magnetic reconnection due to different mechanisms. First, strong electric fields produced at the reconnection site (X-line for two-dimensional reconnection or singular magnetic field lines in three-dimensional reconnection) can directly accelerate the particles. Second, the turbulence produced by the reconnection mechanisms may accelerate the particles stochastically. A third acceleration mechanism could

be connected to the MHD shock waves, which are often a part of the reconnection process [43].

Let us consider the simplest case of runaway generation, i.e. the acceleration by a constant electric field along the magnetic field. Note that we limit our analysis to the acceleration of electrons only.

The electrons are subject to acceleration by the electric field and at the same time to collisional friction. If an electron gains high enough velocity, the collisions become so infrequent that it cannot be effectively slowed down anymore and therefore runs away.

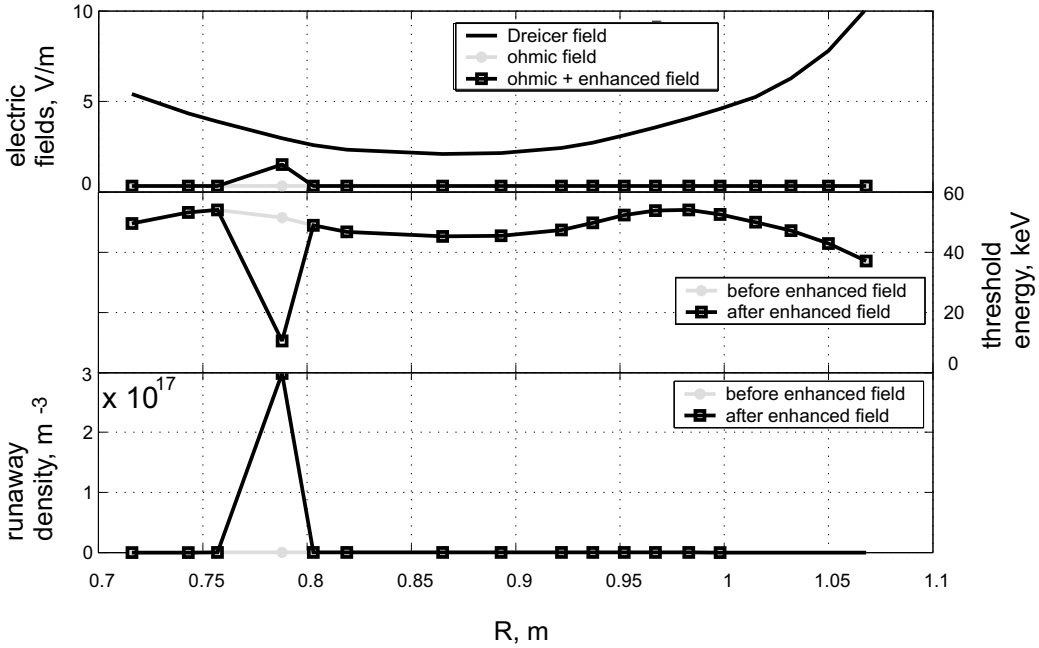

Figure 7.3: *Dreicer field, threshold energy and runaway density for a typical TCV plasma.*

The runaway problem has been considered by Dreicer [49] in 1959. He has demonstrated that for electrons drifting with respect to ions, the collisional force starts to decrease if the drift velocity exceeds $\sqrt{2}v_T$, where v_T is the thermal velocity. The critical electric field that corresponds to the drift velocity $u_d = \sqrt{2}v_T$ is $E_c = 0.214E_D$, where E_D is the so-called Dreicer field (eq. 7.5), given by:

$$E_D = \frac{q_i ln\Lambda}{4\pi\epsilon_0\lambda_D^2} = 3.02 \times 10^{-13}\frac{nln\Lambda}{T_e} \tag{7.5}$$

The problem solved in [49] gives the critical electric field for the average electron of a maxwellian plasma. However, even in the maxwellian distribution there are always electrons with velocities much higher than the thermal velocity. Such electrons run away for electric fields much lower than E_c. As it has been shown in [50], the fraction of runaway electrons for a field E is:

$$\frac{n_r}{n_0} \approx exp\left(-\frac{v_r^2}{2v_{Te}^2}\right) = exp\left(-\frac{E_D}{2E}\right) \tag{7.6}$$

In fig. 7.3 the results of calculations using the Dreicer's formulas for typical TCV plasma parameters are presented, both for a purely ohmic case and under the assumption that the toroidal electric field is locally enhanced by 1.5 V/m around the $q = 1$ radius. Such an assumption will be justified by calculations performed in 7.4.3, showing that an electric field with an amplitude of up to 10 V/m or more can be generated during sawtooth collapse, and the reconnection is believed to occur in the vicinity of the $q = 1$ surface. An electric field of 1.5 V/m has been chosen because it would produce a number of fast electrons ($\sim 3 \cdot 10^{17}$ m^{-3}) relevant to the TCV experiments.

7.4 Sawtooth instability

7.4.1 Experimental observations

Sawtooth oscillations are the most common example of a reconnection process in a tokamak plasma. They appear in many different experimental regimes in tokamaks as periodic variations of the core temperature and density (see fig. 7.4). They have been reported for the first time in [51]. The first theoretical model has been presented in [52].

The typical sawtooth behavior of electron temperature on TCV is shown in fig. 4.17. Each sawtooth cycle can be divided in the ramp phase and the crash phase. During the ramp phase, the temperature rises in the plasma core due to the heating. During the crash phase, the core confinement degrades and the energy accumulated during the ramp phase is released to the outer part of the plasma.

The crash is caused by the $m = 1, n = 1$ instability (supposedly a kink mode [53]), which can appear in the plasma if a $q < 1$ region exists. During the ramp phase, the current profile peaks in the center, i.e. the q value in the center goes down. During the crash, the current profile flattens and the central q value goes up. The crash is associated with magnetic reconnection within the $q < 1$ region. Sometimes a precursor $m = 1, n = 1$ can be clearly seen before the crash (schematically shown in fig. 7.5, real signal in fig. 7.17). Even after the crash, $m = 1, n = 1$ oscillations may remain, indicating incomplete reconnection.

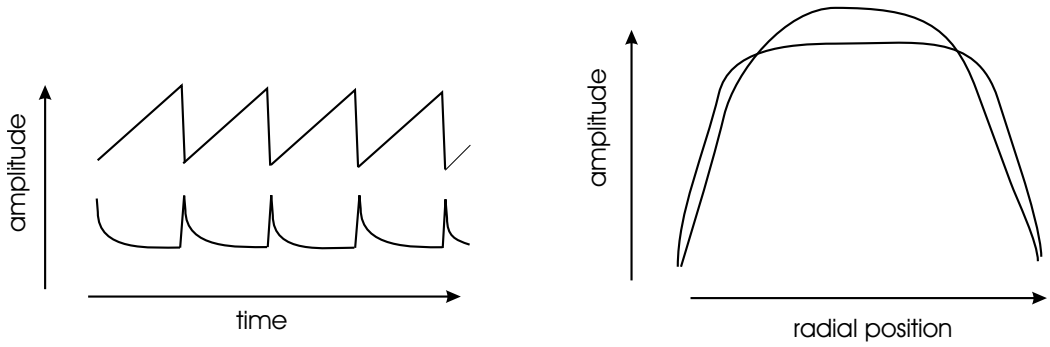

Figure 7.4: *Schematic view of sawtooth oscillations. At the left two time traces are shown. The upper trace corresponds to the central region of plasma ($q < 1$). The shape of the upper trace explains the name of the oscillations. The lower time trace comes from the outer region of the plasma ($q > 1$). At the right the flattening of the profile due to the sawtooth crash is shown. The drawn signals can correspond to the plasma density, temperature or X-ray emission.*

Knowledge of the q-profile is required for understanding and modelling sawtooth crashes. The available experimental data collected on different tokamaks (see ref. in [2], [44]) indicate that during a sawtooth crash the q value in the center changes only by a few percent and stays below unity during the whole sawtooth period. Some reports indicate that the central q value lies in the range 0.7-0.8 (see ref. in [2]).

7.4.2 Kadomtsev sawtooth model

Since the first observations of sawteeth, a huge discrepancy between the duration of the crash ($\sim 100\mu s$) and the characteristic resistive time $\tau_R =$

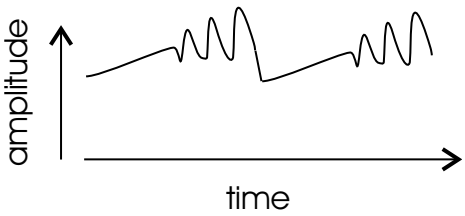

Figure 7.5: *Schematic view of precursor oscillations.*

$\mu_0 r_1^2/\eta \sim 10$ ms has been noted (η - resistivity, r_1 - inversion radius). The first model that proposed the explanation of the fast magnetic reconnection mechanism was the Kadomtsev model [52], which can be considered as a particular case of the Sweet-Parker model, applied to the helical magnetic field of a tokamak.

The Kadomtsev model predicts reconnection times (eq. 7.4, $L \sim$ inversion radius) close to the experimental crash times ($\sim$100 μs). However, there are several important contradictions with the experimental data. In the experiments, the crash time does not scale as $L^{3/2}$. The measured q values in the center often stay well below unity during the whole sawtooth period, while the model predicts values close to unity. There is evidence that the reconnection is often incomplete, while the Kadomtsev model assumes a full reconnection. More involved models have been proposed later (e.g. [54], [55]), but most of these questions are still open.

7.4.3 Evaluation of the electric field generated during the sawtooth crash

In this section we estimate the electric field that can be generated during the sawtooth collapse. Although precise calculations would require an exact knowledge of the current profile and a 3D magnetic equilibrium code, a simple model is sufficient to verify that during reconnection an electric field satisfying the Dreicer condition for a number of electrons can be generated.

According to Faraday's law, the reduction of the poloidal magnetic field flux generates an electric field:

$$\nabla \times E = -\frac{\partial B}{\partial t}. \tag{7.7}$$

In the cylindrical approximation eq. 7.7 can be simplified to:

$$\frac{\partial E_{tor}}{\partial \rho} = \frac{\partial B_{pol}}{\partial t}. \tag{7.8}$$

The rate of change of the poloidal magnetic field can be estimated from the crash time and the assumed change of the current profile (there is no direct measurement of the current profile on TCV). It is convenient to use the safety factor q instead of the current density j.

In the simplest case of a circular plasma cross section, using the cylindrical approximation, the safety factor can be calculated as follows:

$$q_{circ}(r) = \frac{2\pi r^2 B_{tor}}{\mu_0 I(r) R}, \quad where \quad I(r) = 2\pi \int_0^r j(r^{'}) r^{'} dr^{'},$$

where I(r) is the current flowing inside the 'r' flux surface, r is the minor radius, B_{tor} is the toroidal magnetic field, $\mu_0 = 4\pi \cdot 10^{-7}$ H m^{-1} and R is the major radius of the torus. For a plasma with non-circular cross-section the following approximation can be used:

$$q_{shape}(r) \approx \frac{rB_{tor}}{RB_{pol}} \left(\frac{1+\kappa^2}{2}\right) (1+\epsilon^2(1/2\Lambda^2+1))(1.24-0.54\kappa+0.13\delta+0.3(\kappa^2+\delta^2)),$$

where κ is the elongation of the plasma cross-section, δ is the triangularity, ϵ is the tokamak's inverse aspect ratio (r/R) and $\Lambda = \beta_{pol} + l_i/2 - 1$, l_i is the internal inductance.

In our estimation for TCV, we used the q value at the edge, the position of the $q = 1$ surface and we assume that the q value in the center of the plasma changes only by a few percent. This has been observed in a number of tokamaks, in which the current profile can be measured [2]. The q value at the edge can be calculated knowing the total current, the toroidal magnetic field and the plasma shape. The $q = 1$ position can be easily found from the ECE or x-ray measurements. In the example shown in fig. 7.6 the q value in the center of plasma rises from 0.89 to 0.92 during the crash. The resultant toroidal electric field generated by the change of the poloidal magnetic field flux is about 10 V/m (fig. 7.7) if the reconnection time is 100 μs. If we compare this result with the calculations presented in fig. 7.3, we can conclude

that the electric field generated during the collapse is sufficient to accelerate a significant number of the electrons above the runaway (Dreicer) threshold energy.

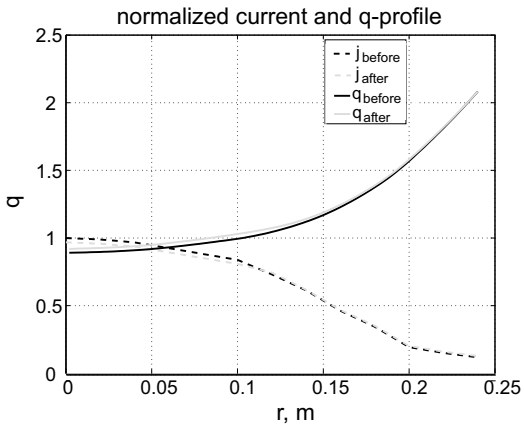

Figure 7.6: *The normalized current and the safety factor profiles before and after the crash on TCV.*

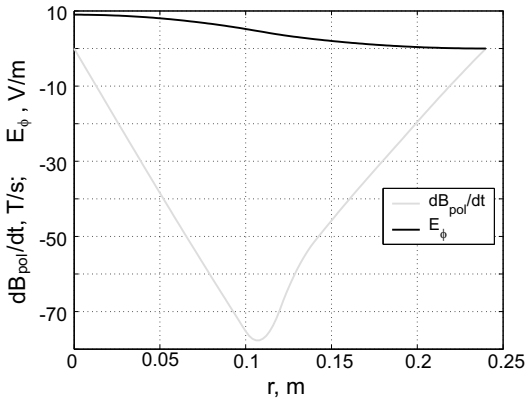

Figure 7.7: *The estimated change in the poloidal magnetic field and generated toroidal electric field during the sawtooth crash on TCV.*

7.5 Experimental data and analysis

7.5.1 Previously reported results

In 1978 it has been found on the Pulsator tokamak [56] that there is a correlation between MHD activity (sawteeth, tearing modes) and hard x-ray emission due to runaway electrons. Hard x-ray emission modulated by sawteeth has been observed even in high density cases, $n_e > 10^{20}$ m^{-3}, and was found to depend on the sawtooth amplitude.

In more recent (2000) experiments on T-10 [57], spikes corresponding to sawtooth crashes have been observed on the data from a tangentially viewing x-ray camera [58]. In some cases one can see enhanced signals correlated with the sawteeth on the conventional soft x-ray imaging system or hard x-ray camera data due to the bremsstrahlung produced by the suprathermal electrons.

One can therefore suppose that those non-thermal electrons could be produced by the magnetic reconnection events (there was no auxiliary heating in those experiments). However, a more detailed study is needed to confirm the acceleration mechanism and quantify the acceleration. Such analysis based on ECE and x-ray diagnostics has been performed on TCV. The results are discussed below.

7.5.2 Proof of the generation of fast electrons due to magnetic reconnection on TCV

In order to demonstrate that the generation of fast electrons is indeed due to magnetic reconnection, all other possible mechanisms should be excluded. This is the reason why the first experiments on TCV dedicated to this subject were carried out without auxiliary heating, i.e. in the ohmic regime.

Important plasma parameters related to the Dreicer acceleration process, such as the plasma density and the loop voltage for a TCV discharge are shown in fig. 7.8. As one can see, during the ohmic phase flattop (t=0.4-0.6 s), these parameters remain constant and the HXR camera detects no fast electrons. However, the HFS ECE profile deviates from the LFS ECE for a short period of time just after the sawtooth crash (fig. 7.9).

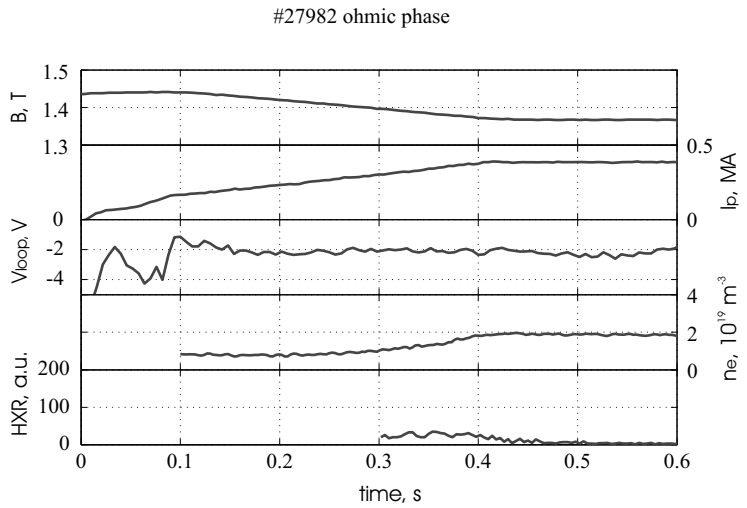

Figure 7.8: *Overview of the ohmic phase of the TCV discharge. The HXR camera signal suggests that there are no fast electrons at 0.4-0.6 s.*

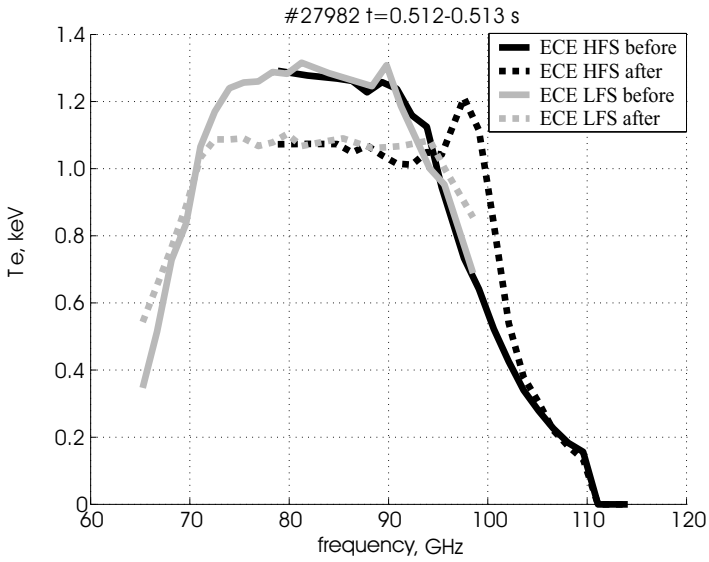

Figure 7.9: *The sawtooth crash (t=0.5124 s) during the ohmic phase of the discharge. The LFS and the HFS ECE profiles are shown for two moments of time - before (t=0.5123 s) and after the crash (t=0.5126 s). The two profiles coincide before the crash, but after the crash the HFS profile significantly deviates from the LFS profile outside the inversion radius, at 95-100 GHz.*

This constitutes a first hint at the generation of energetic electrons during the sawtooth crash, conjecture that is supported by the soft x-ray measurements with aluminium foil, which corresponds to photon energy in the 15-30 keV range. As one can see in fig. 7.10, there are no such photons during the ramp-up phase of the sawtooth, but they appear just after the crash. They are not spatially localized, which suggest that the radiation comes from interaction of the energetic electrons with the tokamak walls.

Combining the observations from the HXR camera, soft x-ray cameras and the ECE radiometers we can come to some first conclusions. There is generally no significant population of non-thermal electrons during the ohmic flattop phase. The non-thermal electrons appear for a short period of time following the sawtooth crash, with energies at least up to 30 keV. Some of these electrons quickly leave the plasma, heating the walls of tokamak, producing spikes of non-thermal x-ray radiation. Others are probably slowed down by the bulk plasma. Below we analyze this phenomenon in detail.

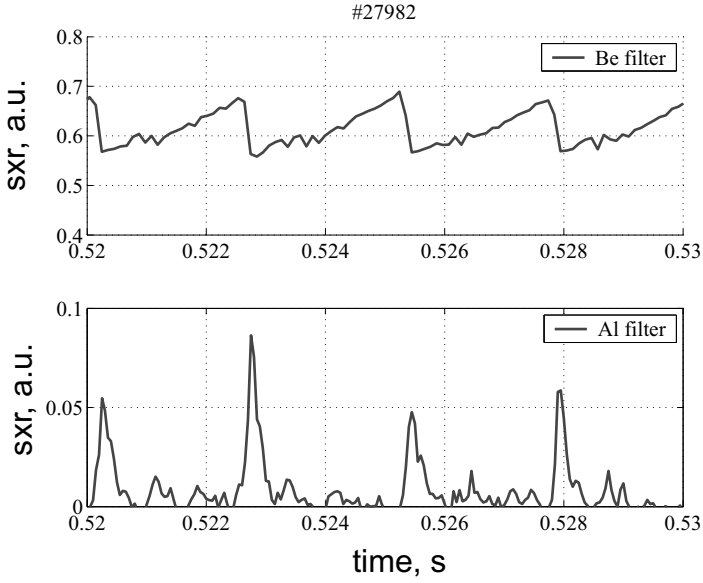

Figure 7.10: *The comparison of two x-ray signals, obtained with different filters. The signal at the bottom is not sensitive to the photons with energies below 15 keV (Al filter 308 μm + 350 μm Be filter), while the signal at the top includes photons in the energy range 1-10 keV (47 μm Be foil). Obviously the non-thermal photons can be registered only after the sawtooth crash.*

7.5.3 The dependence on the amplitude and the period of the sawteeth

The effect described above appears to be more pronounced for bigger sawteeth. Therefore, special measures should be taken to increase the sawtooth amplitude, such as plasma shaping (increased triangularity), impurity puffing (argon injection) or, most effectively, auxiliary heating (ECH). While ECH does not produce significant numbers of non-thermal electrons, ECCD does. In this case, as it is shown below, the population of fast electrons grows during the short time period just after the crash and then relaxes to the steady-state level defined by the ECCD. For the reason of simplicity we start the analysis from plasmas without ECCD.

Instead of extracting the suprathermal density or temperature from the ECE measurements, we simply use the deviation of the HFS ECE from the thermal level to characterize the non-thermal population and compare many sawteeth. Later, for a few typical cases, we will try to quantify the suprathermal population more precisely in terms of density and temperature.

The HFS ECE deviation corresponds (eq. 7.9) to the energy $W_{st} \propto (n_{st} \cdot T_{st})$ of the suprathermal electrons, provided that the suprathermal population is optically thin ($\tau_{st} << 3$) and the suprathermal temperature does not vary significantly. The former condition is usually true for the electrons generated by reconnection only. The latter condition cannot be easily verified, thus the HFS ECE deviation is used as a rough estimation only.

$$\tau_{st} = \frac{T_{hfs} - T_{lfs}}{T_{st}}, \qquad for \qquad \tau_{st} << 1 \tag{7.9}$$

In eq. 7.9, τ_{st} denotes the optical depth of the suprathermal population in the bi-maxwellian approximation (Chapter 5), T_{hfs} and T_{lfs} are the values measured by the HFS and the LFS ECE, and T_{lfs} is assumed to be equal to the bulk temperature. This is a reasonable assumption if $\tau_{st} << 3$ and $\tau_{bulk} > 3$. The cases where T_{lfs} is significantly different from the bulk temperature are considered later. T_{st} is the suprathermal temperature in the bi-maxwellian approximation.

In fig. 7.11 the HFS ECE deviation is plotted versus the sawtooth crash amplitude. Crash amplitudes less than 500 eV correspond to the ohmic phase of the discharge, while the bigger crashes were achieved with ECH (no ECCD). As one can see, the dependence is nearly linear.

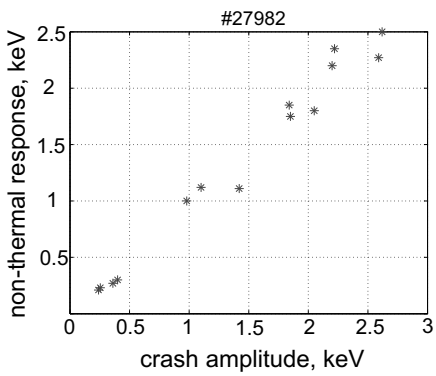

Figure 7.11: *The dependence of the ECE HFS profile deviation on the sawtooth crash amplitude.*

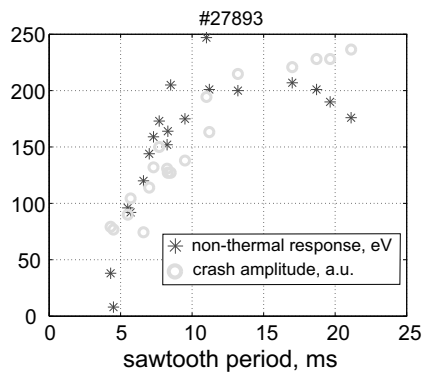

Figure 7.12: *The dependence of the ECE HFS profile deviation on the sawtooth period.*

In fig. 7.12 the HFS ECE deviation is plotted versus the sawtooth period. A rise of the HFS ECE deviation with a sawtooth period in the range of $4-8$ ms

can be mainly due to the corresponding increase in the crash amplitude, which is also shown in fig. 7.12. Therefore, there is no obvious dependence of the energy of the suprathermal electrons on the sawtooth period itself.

7.5.4 Characteristic times

In the TCV discharges the typical duration of the crash, obtained from ECE measurements is 20-60 μs. The crashes are slightly longer in the ohmic phase of the discharge, compared to the ECRH phase. Apparently, the reason is that the sawtooth inversion radius is smaller during the ECRH phase (see fig. 7.13), because the current density profile becomes more peaked. The crash time derived from the x-ray measurements is typically about 100 μs. This slight discrepancy can be explained by the fact that the x-ray measurements are also sensitive to the plasma density, which does not drop as quickly as the electron temperature.

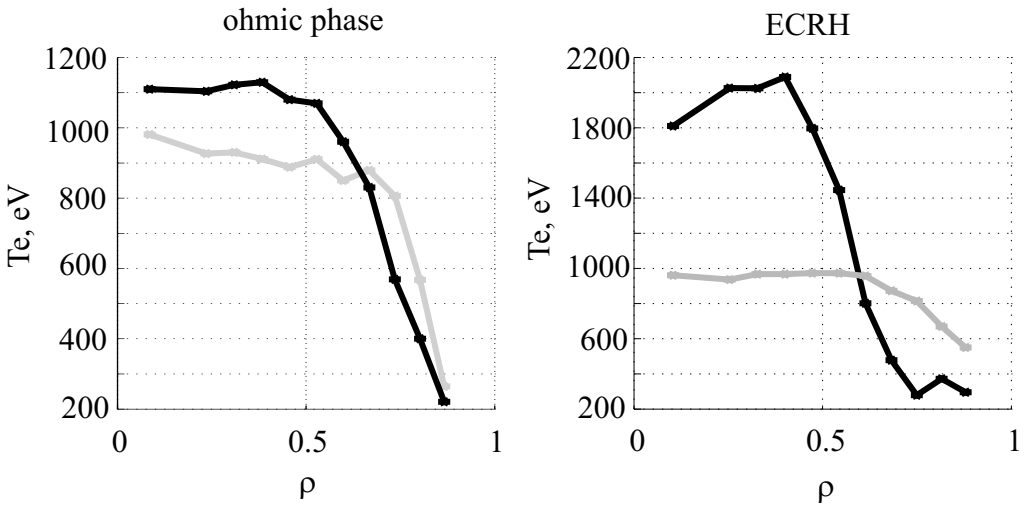

Figure 7.13: *Two sawtooth crashes during the same TCV discharge. The temperature profile is more peaked in the ECRH phase of the discharge (on the right) and the sawtooth inversion radius is slightly narrower.*

The duration of the non-thermal ECE after the sawtooth crash is typically about 1 ms (fig. 7.15-7.17). The decay of the non-thermal signal is exponential. The characteristic decay times are in 200-400 μs range (fig. 7.14). The slowing-down time for the electrons with an energy of 15-30 keV is 1-2 ms (Appendix E). Since reconnection lasts for less than 100 μs and it is nearly

over by the time when the non-thermal HFS ECE starts to decrease, and taking into account that the slowing down time is expected to be 5 times longer than the observed relaxation time (1-2 ms vs. 200-400 μs), we can conclude that the observed times correspond to the average life time of the fast electrons in the plasma.

As shown in fig. 7.16, the non-thermal ECE starts at the beginning of the crash. The maximum of the non-thermal emission occurs 20 μs after the end of the crash. The pitch-angle scattering time for the electrons with energies 15-30 keV is 30-90 μs and is comparable with the crash time + 20 μs.

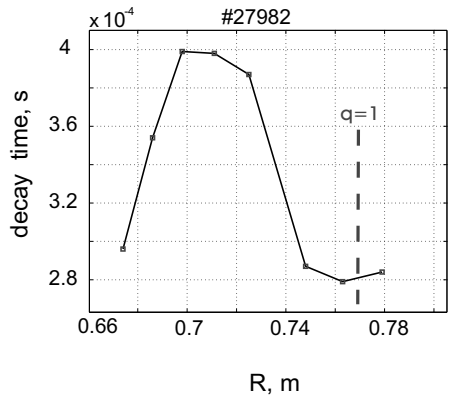

Figure 7.14: *The decay time for the non-thermal HFS ECE signals corresponds to the average lifetime of the suprathermal electrons in the plasma.*

Fig. 7.15 shows the comparison of the HFS and LFS ECE. The center of plasma corresponds to 82 GHz. The non-thermal emission is visible on the HFS ECE in the frequency range 90-105 GHz during ~1 ms after the crash (see also 'HFS off-axis' signal in fig. 7.17). The LFS ECE in the same frequency range shows only a moderate increase of the emission after the crash during ~0.5 ms (see also 'LFS off-axis' signal in fig. 7.17), which can be explained by the heat pulse propagating from the plasma core outwards [17], although some contribution from the fast electrons is possible. One can note that during the ramp phase following the crash the precursor m=1, n=1 appears.

Fig. 7.16 shows the comparison of two sawteeth on a faster time scale. The contour plot on the right shows the non-thermal emission after the crash even in 80-90 GHz frequency range, corresponding to the plasma core. However,

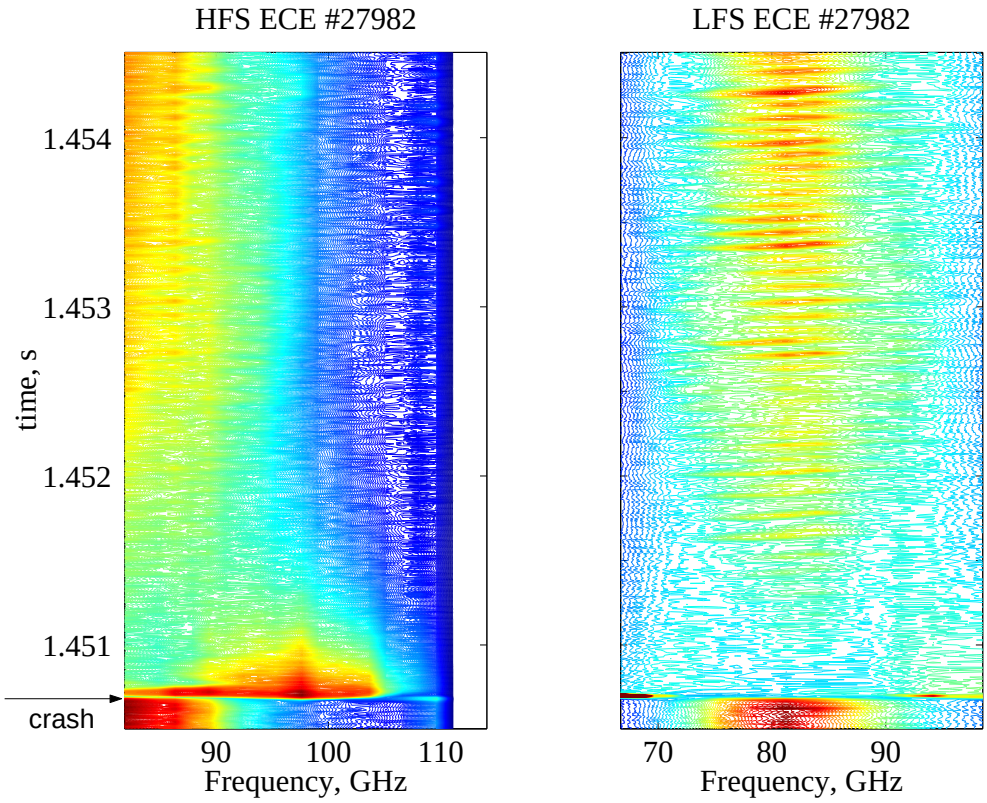

Figure 7.15: *The contour plots of the HFS ECE (on the left) and the LFS ECE (on the right) during sawtooth crash (#27982).*

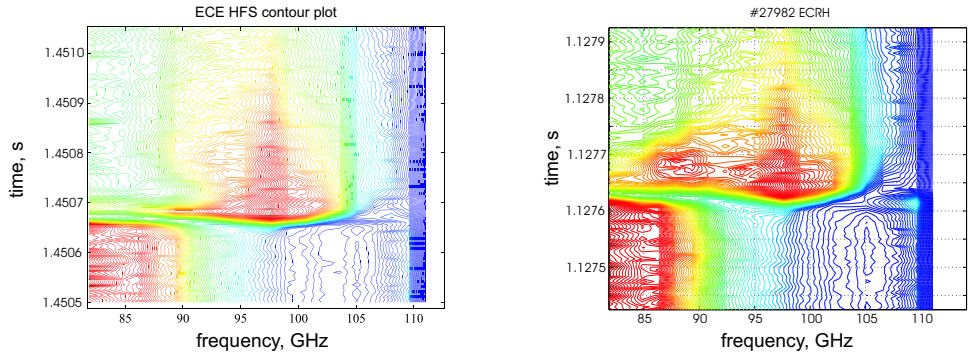

Figure 7.16: *The contour plots of the HFS ECE on a fast time scale for two different sawteeth.*

it does not necessarily imply that a significant number of the fast electrons is present in the plasma core. The effect can arise from the relativistically

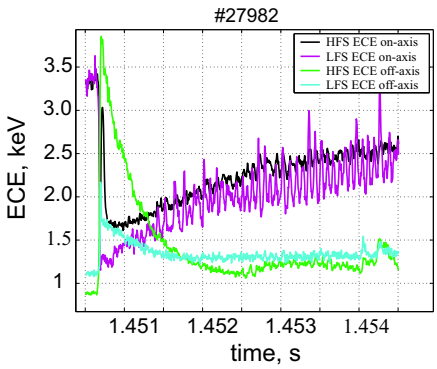

Figure 7.17: *The ECE time traces during the sawtooth crash. 'On-axis' signals were measured at 83 GHz, while 'off-axis' signals at 97 GHz.*

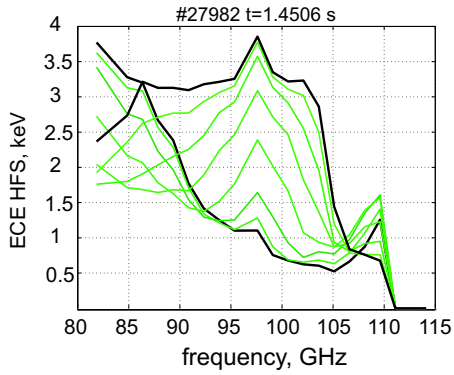

Figure 7.18: *The HFS ECE profiles during the sawtooth crash with 5 μs steps. The HFS ECE rises at 92-105 GHz.*

downshifted emission of the fast electrons localized in the vicinity of the $q = 1$ radius. One can note that on the time scale of 500 μs the maximum of the non-thermal HFS ECE does not drift away radially.

Fig. 7.17-7.18 are complementary to fig. 7.15. Fig. 7.17 shows four ECE time traces during the crash already presented in fig. 7.15. Two 'on-axis' traces were measured at 83-84 GHz from the LFS and the HFS, and correspond to the $q < 1$ region. Two 'off-axis' traces were measured at 97-98 GHz and correspond to the $q > 1$ region. One can notice a large discrepancy between the two 'off-axis' signals after the crash. The effect is associated with the presence of non-thermal electrons. Fig. 7.18 shows the HFS ECE profiles with 5 μs time steps starting at $t = 1.4506$ s and gives an idea about the amplitude of the signals shown in fig. 7.15.

7.5.5 Estimation of the energy and density of the fast electrons

In order to estimate the energy and density of the fast electrons generated by reconnection, modelling of the distribution function is required. The idea is to use the model described in Chapter 5 to simulate the experimentally measured ECE spectra.

First, we consider cases in which the LFS ECE remains thermal during the

crash, while the HFS ECE exhibits non-thermal behavior. Since the reconnection is believed to be local and the deviation of the HFS ECE is not very large compared to the bulk temperature, we can assume that the fraction of the accelerated electrons is small and use the bi-maxwellian approach. Unfortunately, the shape of the distribution function cannot be experimentally reconstructed on such a short time scale (insufficient temporal resolution of the HXR camera).

The soft x-ray diagnostic can only provide information on the presence of electrons with energies in the 15-30 keV range just after the crash. It is very difficult to extract their density or location in the plasma, because the x-ray signal is line integrated, depends on the plasma density and impurities and is heavily polluted by emission coming from the walls of the tokamak. To find these parameters we shall use the HFS ECE measurements.

We assume that the energy spectrum of the accelerated electrons does not vary significantly in space. This assumption is justified by the fact that electrons are accelerated locally, in a region where the plasma parameters, such as the electron density, are approximately uniform. The first conclusion from the modelling of the HFS ECE spectra is that the density profile of suprathermal electrons has a maximum located outside the q=1 magnetic surface. Depending on the slope of the distribution function, the location of the maximum can be shifted towards the HFS, thus the maximum suprathermal temperature for the bi-maxwellian approach corresponds to the case where the fast electrons are confined at the HFS edge of the plasma. For shot #27982 during the ECRH phase (t=1.4506), the maximum suprathermal temperature and the bulk temperature were found to be $T_{st} < 11$ keV and $T_{bulk} < 3.5$ keV.

The lower limit for the suprathermal temperature is imposed by the need for the HFS ECE signal to reach the measured level of 4 keV outside the $q = 1$ radius. This way we get $T_{st} > 4.4$ keV. The minimum suprathermal density required to reach the observed level of the non-thermal ECE HFS emission at $T_{st} = 11$ keV is $2 \cdot 10^{17}$ m^{-3}. This can be higher for lower suprathermal temperatures.

A typical suprathermal density profile used in the modelling is shown in fig. 7.19. The location of the maximum outside the $q = 1$ surface and the existence of the fast electrons in the plasma core are important features of the profile. An example of the modelled spectrum of the HFS ECE along with the profile measured on TCV just after the collapse is also shown in

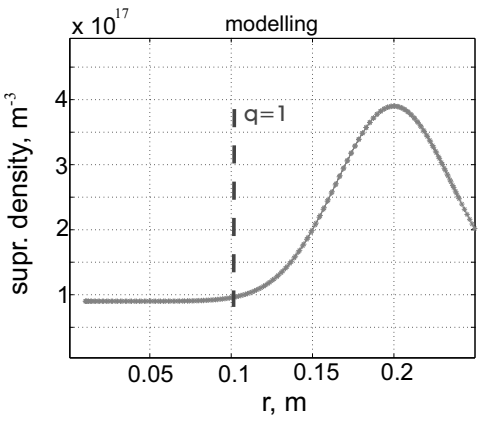

Figure 7.19: *Typical suprathermal density profile used in the modelling.*

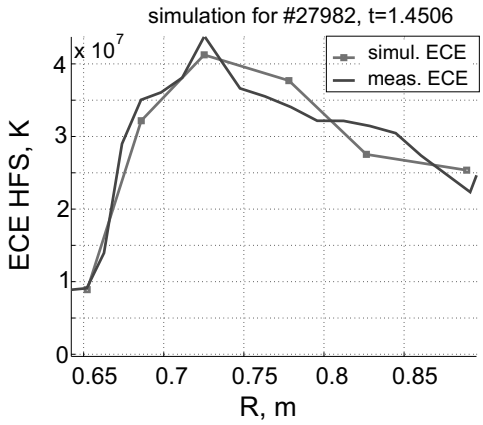

Figure 7.20: *Example of the simulated HFS ECE along with the measured profile (#27982).*

fig. 7.20.

Sometimes very short (20 μs) spikes of non-thermal LFS ECE can be observed during reconnection (fig. 7.21). Both the LFS and the HFS ECE spectra cannot be modelled simultaneously using a bi-maxwellian or a similar distribution function, such as the two-slope or the three-slope EDF. Since all typical relaxation times are longer than 20 μs, there is no reason why the EDF should be similar to a sum of maxwellians. Much better agreement with experimental profiles during the LFS ECE spikes has been achieved using an exponential distribution (eq. 7.10)

$$f(x) = \lambda \cdot exp(-\lambda x), \quad \lambda > 0. \tag{7.10}$$

This form is normally used to model the time interval between successive rare random events, or, in other words, 'time-to-failure' measurements, when the 'failure' (hazard) rate is constant over time. A more general form of the exponential distribution is the Weibull distribution for the case where the 'failure' rate is not constant over time:

$$f(x) = \frac{c}{b}\left(\frac{x}{b}\right)^{c-1} exp\left(-\left(\frac{x}{b}\right)^{c}\right), \quad b > 0,\ c > 0. \tag{7.11}$$

Here b is the scale parameter and c is the shape parameter. In our case, we can see the process as an acceleration of the electron until the first collision

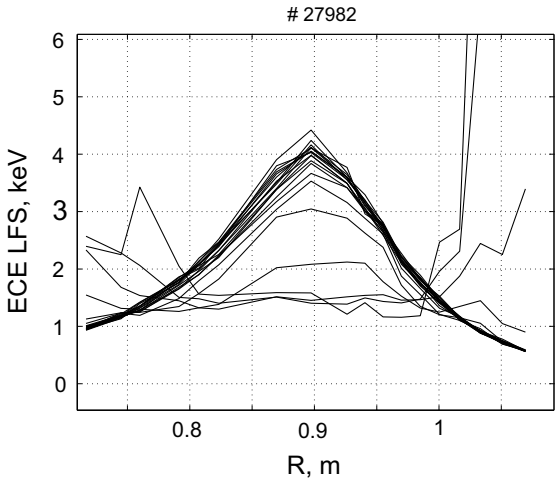

Figure 7.21: *The LFS ECE during the crash. The spikes of the non-thermal emission last for 20 μs.*

(failure) happens. The longer the acceleration without collisions, the higher the gained energy. The exponential distribution, normalized such that its integral over the velocity space is equal to the plasma density, can be written as

$$f(p) = \frac{n_e}{(16\pi m_e k_b T_\lambda)\sqrt{2 m_e k_b T_\lambda}} exp(-\frac{p}{\sqrt{2 m_e k_b T_\lambda}}), \tag{7.12}$$

where p is the electron momentum. Note that T_λ does not have the same meaning as the temperature T in normal (maxwellian) distributions, i.e. it does not correspond to the mean electron energy. For example, in our simulation of the LFS spikes, we used $T_\lambda = 2.5 \cdot 10^6$ K, which corresponds to the mean kinetic energy of electrons of $4 \cdot 10^7$ K.

In regimes with ECCD, where the fast electrons are directly generated, the sawtooth significantly enhances the non-thermal population for the short period of time following the crash. Again, most of the electrons accelerated during the crash are located outside q=1. Other features, such as the time scale of the enhancement, are similar to the regimes without ECCD, except for the higher amplitude of the non-thermal response, which significantly exceeds the thermal level ($T_{bulk} < 5$ keV). Obviously, the existence of suprathermal electrons with a temperature $T_{st} > 15$ keV before the sawtooth crash, results in higher energies and higher numbers of electrons accelerated

by the reconnection process at the crash.

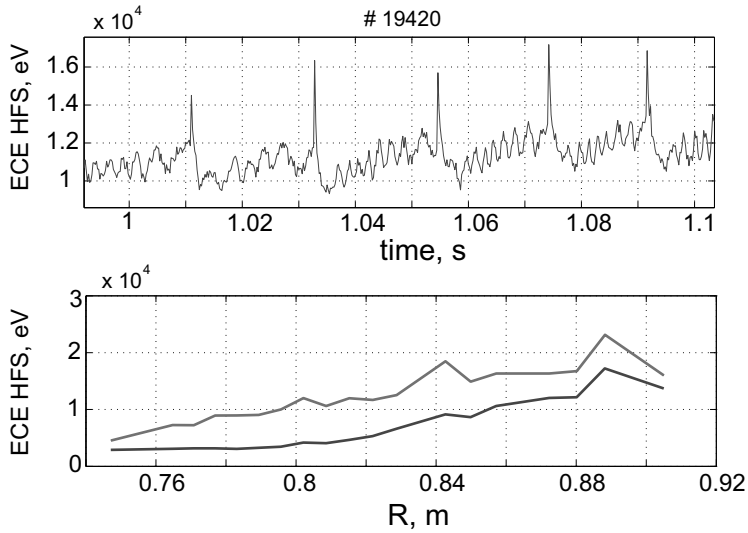

Figure 7.22: *The HFS ECE during the crash in the discharge with ECCD. The lower profile corresponds to the moment before the crash and the upper profile to the moment just after the crash.*

7.6 Discussion and conclusions

The energy released through acceleration of electrons in the ECRH plasma (e.g. up to 500-600 J for # 27982) is up to 30-40 % of the energy lost during the crash and it is up to 10 % of the energy stored in the plasma. Note that ions are not taken into account in these estimations. The maximum of the non-thermal emission is reached 40 μs after the beginning of the reconnection process, which corresponds to a power of 15 MW.

The time interval between the appearance of the non-thermal emission and the moment when the maximum of the non-thermal ECE is reached is longer than the crash duration, suggesting that reconnection processes last longer than the crash itself.

The Dreicer acceleration mechanism seems to be appropriate for the description of the observed acceleration. The hotter the plasma, the larger the number of the electrons that can be accelerated by a given electric field. The

estimated electric field generated by reconnection can produce the number of fast electrons that are required to simulate the experimental ECE spectra.

The profile of the suprathermal electrons is observed to be peaked outside the $q = 1$ surface. This can be explained by the fact that there is no magnetic surface structure inside q=1 just after the crash. The suprathermal profile inside q=1 becomes immediately flat over a large region (fig. 7.19), while magnetic surfaces still exist outside q=1.

The observed evolution of the ECE HFS profile suggests that the radial diffusion dominates over the slowing down. An effective diffusion coefficient for the fast electrons during the sawtooth collapse and shortly after the collapse can be calculated either from the broadening of the suprathermal profile at the beginning of the reconnection or from the relaxation of the suprathermal profile when the acceleration is over. Using the former approach, for the observed characteristic time of 35 μs (fig. 7.18) and a broadening of 3 cm, obtained from the modelling of the non-thermal ECE, we estimate $D_{st} = 25$ m^2/s. The latter approach gives the same result using the relaxation time of 390 μs (fig. 7.17) and 10 cm as distance from the location of the suprathermal electrons to the plasma edge.

The obtained diffusion coefficient is higher than values reported typically for Lower Hybrid Current Drive (LHCD) experiments $D_{st} = 0.1 - 1$ m^2/s, except for JET where $D_{st} = 6 - 10$ m^2/s [59]. In TCV, during ECCD the diffusion coefficient for fast electrons was estimated to be $D_{st} = 0.5 - 5$ m^2/s [42].

Such discrepancy can be explained by the fact that we analyze the dynamics of the fast electrons during and just after the crash, when, due to the reconnection and redistribution of magnetic field lines, the confinement is worse than during the sawtooth ramp phase. The fact that confinement is normally better in the plasma core (relevant to the LHCD/ECCD experiments) than at the plasma edge also helps explaining the gap. Note also that the electrons in the LHCD/ECCD experiments have large parallel momentum and energy in the range 100-200 keV, while we look at 15-30 keV electrons.

Additional information either on the energy spectrum or location of the fast electrons would be needed to extract more precise data from the ECE spectra. One possibility is to install a tangential x-ray camera, which would be more sensitive to the localized population of the fast electrons due to its viewing geometry then a conventional x-ray camera viewing the poloidal plasma cross section.

Chapter 8

Conclusions and outlook

In the course of this thesis a new ECE radiometer viewing the plasma from the low field side, which is an important addition to the diagnostic suite of the TCV tokamak, has been developed. A main application of the radiometer is a measurement of electron temperature, highly resolved both in time and space. This allows study of the plasma confinement and stability on TCV. In combination with an existing radiometer viewing the plasma from the high field side, non-thermal electron dynamics can be investigated. In addition, the radiometer has multiple lines of sight, which can receive the emission perpendicular to the toroidal magnetic field as well as with a finite $k_{\|}$. The toroidal line of sight allows access to over-dense plasmas via mode converted emission.

A numerical model simulating the ECE spectrum has been developed. The model takes into account thermal and non-thermal components of the distribution function, finite optical depth, finite resonance layer thickness and harmonic overlap. The ECE model allows analysis of the non-thermal and anisotropic emission.

The developed diagnostic and numerical tools have been applied to analyze the changes of the electron distribution function during ECCD and sawtooth crashes corresponding to magnetic reconnection events. It was found that high power X2 ECCD together with X3 ECRH can locally modify the electron distribution function such that it cannot be properly described using the bi-maxwellian distribution. On the other hand, the two-slope distribution proposed in this thesis is consistent with the experimental observations, including anomalously high X3 absorption.

It has been shown that fast changes of the electron distribution function

during sawtooth collapse are accompanied by acceleration of electrons. The energy spectrum of the accelerated electrons depends on the sawtooth amplitude and the global plasma parameters affecting the Dreicer acceleration mechanism. The non-thermal population produced by the sawtooth crashes has been quantified ($n_{st} > 2 \cdot 10^{17}$ m^{-3}, $E = 15 - 30$ keV). The importance of electron acceleration as a mechanism for dissipating the energy released during magnetic reconnection has been shown (30-40 % of the energy lost during the crash appears in the form of fast electrons). The observed dynamics of the fast electrons suggests high radial diffusion during and just after the crash (an estimate of $D_{st} = 25$ m^2/s has been made), dominating over the classical slowing down process.

The high diagnostics potential of the ECE system for studying fast electrons has been demonstrated. Further improvements to the diagnostics and modelling are possible. The main concern is the uncertainty in the results of the reconstruction of the electron distribution function. The reconstruction is an ill-posed problem, as it requires an inversion. Several solutions are usually possible because neither the location nor the energy spectrum of the fast electrons is known exactly. To overcome this obstacle, additional experimental information should be gathered using other diagnostics. That has motivated the development of a tangential x-ray camera [58], [57] for TCV, which is underway. A tangential x-ray camera can provide more precise information about the localization of fast electrons, which will add constraints to the inverse problem.

To facilitate the reconstruction of the electron distribution function, an iterative scheme should be implemented. In this way, the parameters to be determined, describing the non-thermal population, namely the suprathermal electron density profile and energy spectrum, would be found by a routine, which would model the ECE spectra, until the best match for the experimental spectra is found. This optimization should include all available experimental information, such as the location of the suprathermal electrons, if it is known from the tangential x-ray data.

The method for reconstructing the electron distribution function used in this thesis can be used to study wave-particle interactions in the plasma, in particular to better understand the current drive process and to predict its efficiency in future thermonuclear installations.

Finally, the ECE system on TCV itself will be upgraded. An ECE antenna with a smaller poloidal spot size will improve the sensitivity for MHD mode

studies and will allow correlation ECE measurements ([60], [61]) to detect small-scale modes in the plasma.

Appendix A

Microwave components characteristics

Table A.1: Balanced mixer MXP-10-RSSXL. Mixer specifications.

RF	LO	IF	Conversion loss
Frequency 83.5 - 99.5 GHz	Frequency 81.5 GHz	Frequency 2-18 GHz	10.0 dB max
Power -10 dBm	Power +13 dBm		
Frequency, GHz	Frequency, GHz	Frequency, GHz	dB
83.5	81.5	2	7.1
87.5	81.5	6	6.8
91.5	81.5	10	7.5
95.5	81.5	14	7.7
99.5	81.5	18	8.2

Table A.2: Balanced mixer MXP-12-RSSXL. Mixer specifications.

RF	LO	IF	Conversion loss
Frequency 65 - 81 GHz	Frequency 63 GHz	Frequency 2-18 GHz	9.0 dB max
Power -10 dBm	Power +13 dBm		
Frequency, GHz	Frequency, GHz	Frequency, GHz	dB
65	63	2	7.6
67	63	4	7.5
69	63	6	8.3
71	63	8	7.6
73	63	10	8.2
75	63	12	7.2
77	63	14	7.8
79	63	16	8.5
81	63	18	8.4

Table A.3: Backshort tuned Gunn Oscillator GDM-12-0216R. Mechanical Tuned Gunn Oscilator specifications.

Micrometer, inch	Frequency, GHz	Power out, mW
0.246	64.00	76
0.253	63.75	79
0.258	63.50	75
0.265	63.25	63
0.271	63.10	59
0.274	63.00	58
0.278	62.90	58
0.282	62.75	60
0.287	62.50	63
0.292	62.50	55
0.300	62.00	45

Table A.4: Backshort tuned Gunn Oscillator GDM-10-0216R. Mechanical Tuned Gunn Oscilator specifications.

Micrometer, inch	Frequency, GHz	Power out, mW
0.307	82.50	75
0.294	82.25	76
0.269	82.00	75
0.261	81.75	76
0.250	81.60	76
0.240	81.50	75
0.226	81.40	75
0.212	81.25	75
0.187	81.00	74
0.162	80.75	72
0.134	80.50	71

Table A.5: High Pass WR-10 Filter FHP-10-08235.

Test parameter	Specified	Measured
Passband frequencies	85.5-110 GHz	85.5-110 GHz
Insertion loss (passband)	1.50 dB	1.12 dB
Corner frequency (-3 dB point)	81.50	2.90 dB at 81.5 GHz
Rejection level and frequency (typ)	35 dB at 73.4 GHz	39.28 dB at 73.4 GHz

Table A.6: High Pass WR-12 Filter FHP-10-06335.

Test parameter	Specified	Measured
Passband frequencies	67-90 GHz	67-90 GHz
Insertion loss (4 GHz above cut-off frequency)	1.25 dB (max)	0.65 dB
Cut-off frequency (-3 dB point)	63.50	1.87 dB at 63 GHz
Rejection level and frequency (typ)	35 dB at 56.7 GHz	49.16 dB at 56.7 GHz

Table A.7: High directivity directional coupler QJR-E03300.

Frequency GHz	Coupling Value, dB	Directivity dB	VSWR Mainline	VSWR Coup.line
60-90	2.8	35.0	1.095	1.105

Table A.8: Amplifier AFS42-00101800-25-10P-42.

Frequency	Gain	VSWR	Noise Figure	Output power
GHz	dB	In/Out	dB	at 1 dB gain compression
0.1	40.26	2.31/1.65	2.66	10.61
0.5	40.31	2.02/1.66	2.34	10.55
2.0	40.25	2.16/1.59	2.43	10.34
4.0	40.11	2.11/1.34	2.40	11.31
6.0	39.56	2.15/1.58	2.31	12.31
8.0	39.87	2.16/1.98	2.26	12.34
10.0	39.64	2.19/1.86	2.20	12.66
12.0	39.54	2.20/1.87	2.13	10.69
14.0	38.36	2.21/1.73	2.15	12.44
16.0	38.55	2.06/1.56	2.22	12.64
18.0	40.13	2.21/1.95	2.10	12.31

Table A.9: Microwave cable assembly Sucoflex-104, 500 mm length, SMA connectors.

Frequency range, GHz	Insertion loss max, dB	Return loss max, dB
0.1-1.9	0.19	40.08
1.9-3.6	0.27	36.54
3.6-5.4	0.31	33.22
5.4-7.2	0.44	29.82
7.2-9.0	0.46	29.35
9.0-10.8	0.50	27.14
10.8-12.6	0.51	27.97
12.6-14.4	0.54	26.84
14.4-16.2	0.56	26.21
16.2-18.0	0.60	24.50

Appendix B

IF spectrometer characteristics

1	Number of channels	24
2	Noise factor, dB	< 3
3	Dynamic range, dB	> 23
4	Bandwidth of IF channel, MHz	750
5	Bandwidth of video amplifiers, kHz	100
6	Output voltage of the video amplifiers (for load resistance of 2 $k\Omega$), V	$0 - 10$
7	Local oscillator frequency stability, MHz	< 15
8	Gain stability, % (for ambient temperature variation of $2 - 3^o$ C)	2.5
9	Digital control of each channel gain, 0.5 dB step	up to 20 dB

Channel #	Central frequency, GHz
1	1.60
2	3.05
3	4.51
4	5.96
5	7.42
6	8.87
7	10.33
8	11.78
9	13.24
10	14.69
11	16.14
12	17.60

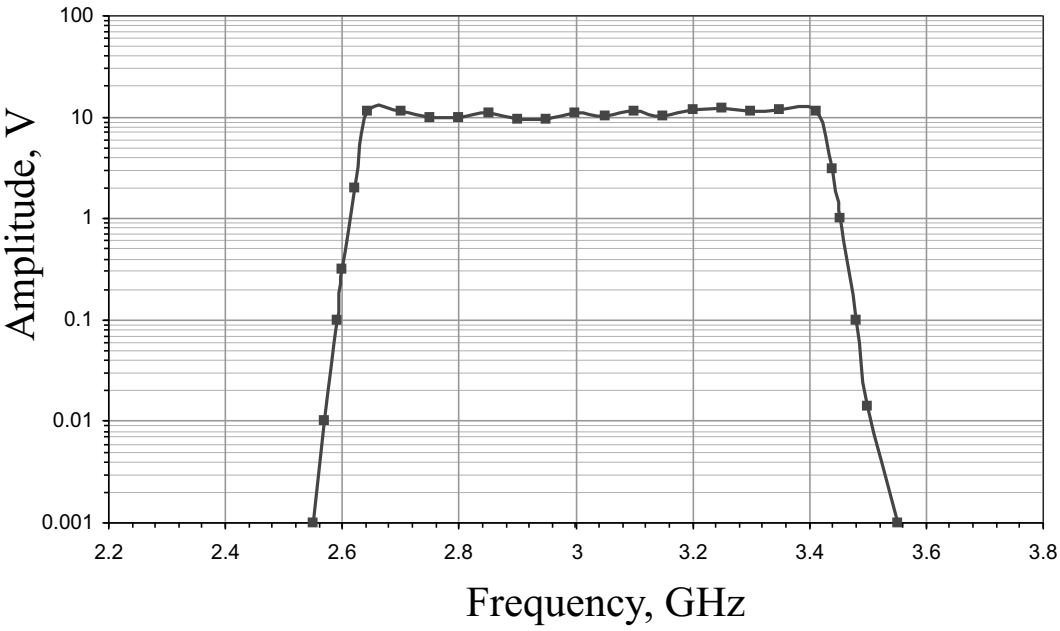

Figure B.1: *Amplitude-frequency characteristic of the IF spectrometer channel.*

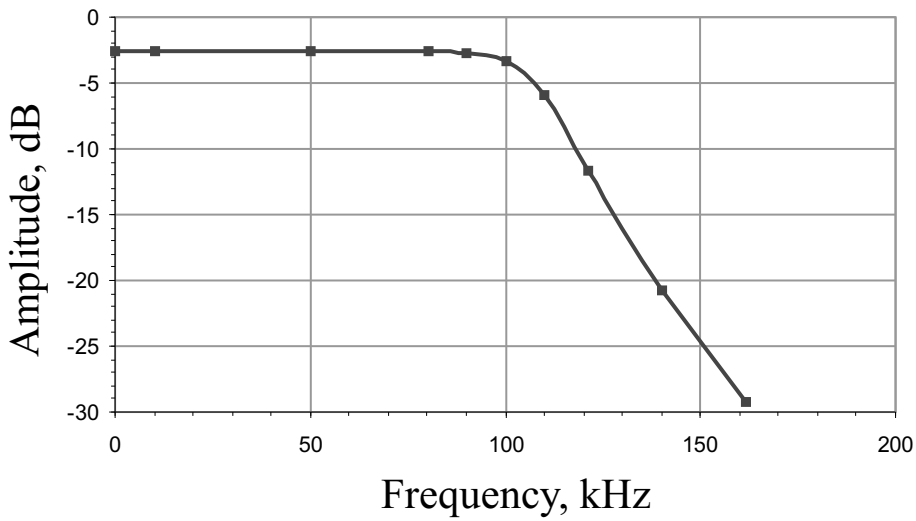

Figure B.2: *Amplitude-frequency characteristic of the video amplifier.*

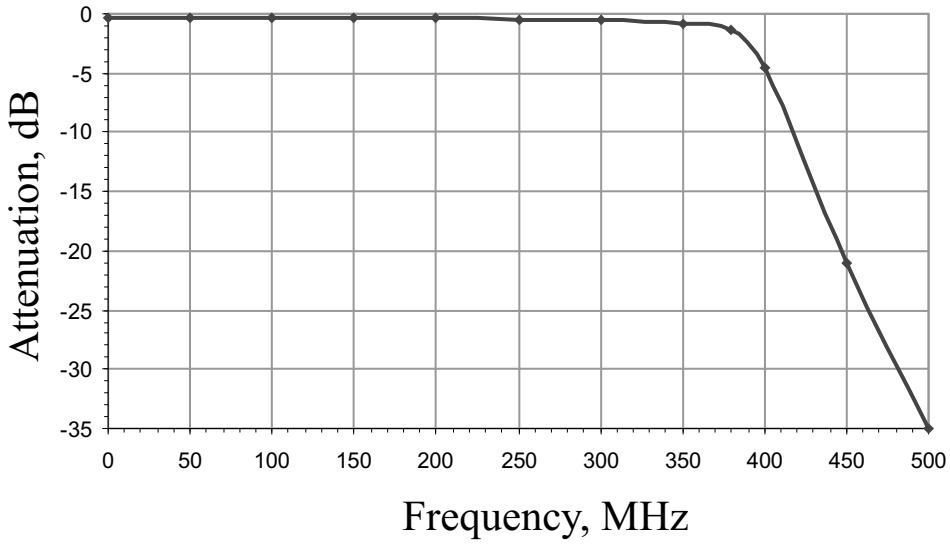

Figure B.3: *Attenuation-frequency response of the IF filter section.*

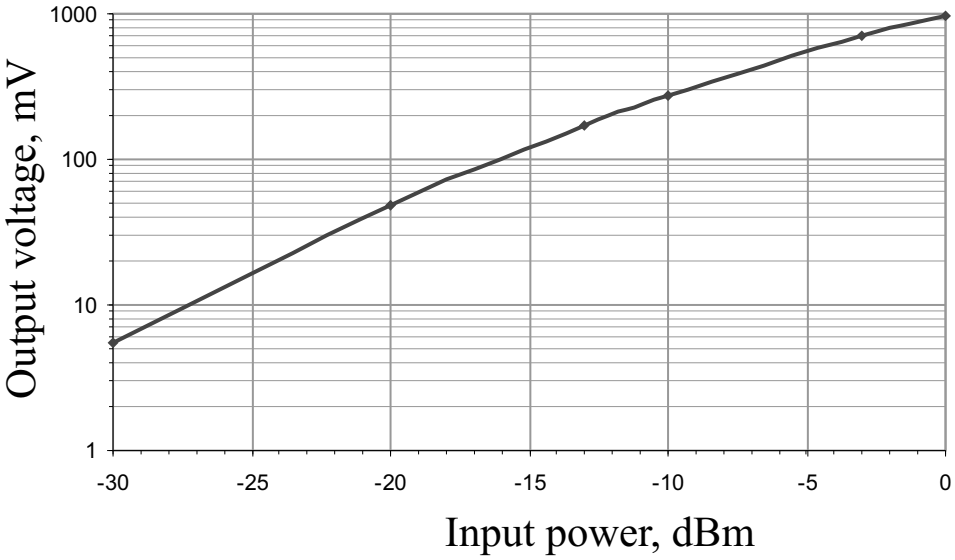

Figure B.4: *Input-output characteristic of the IF spectrometer channel.*

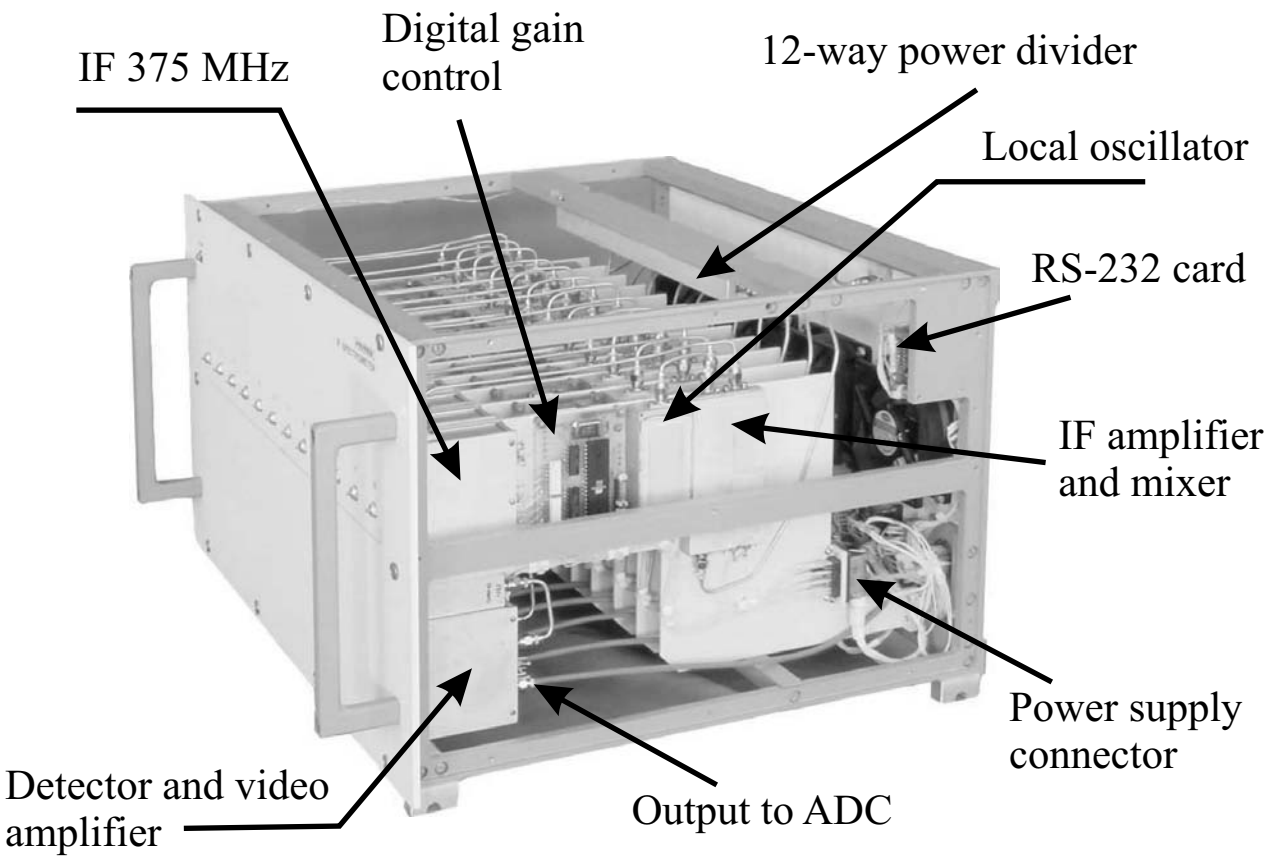

Figure B.5: *Side view of the 12-channel IF spectrometer. The main components are indicated.*

Appendix C

Transmission line

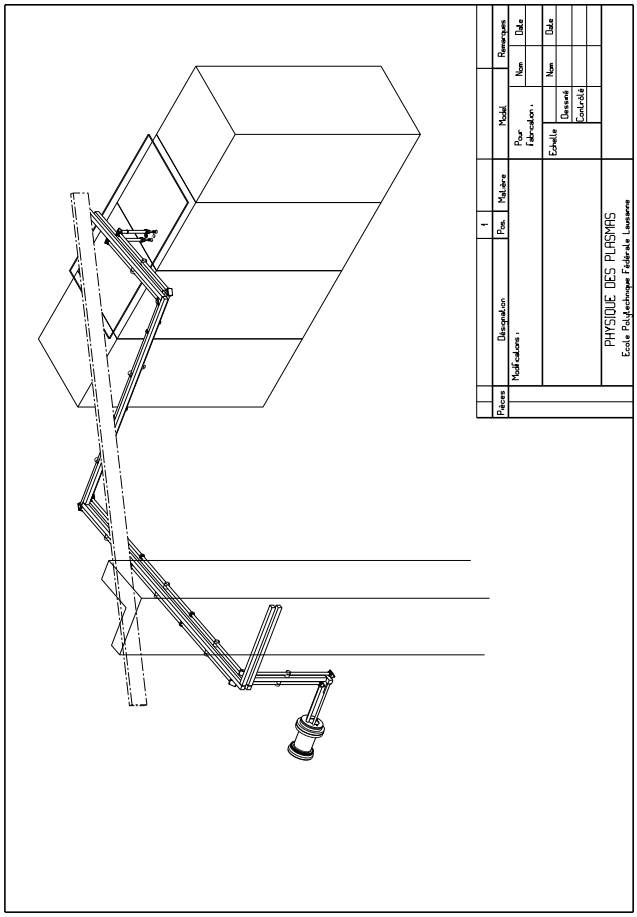

Figure C.1: *Oversized waveguide lines from the vacuum window to the radiometer.*

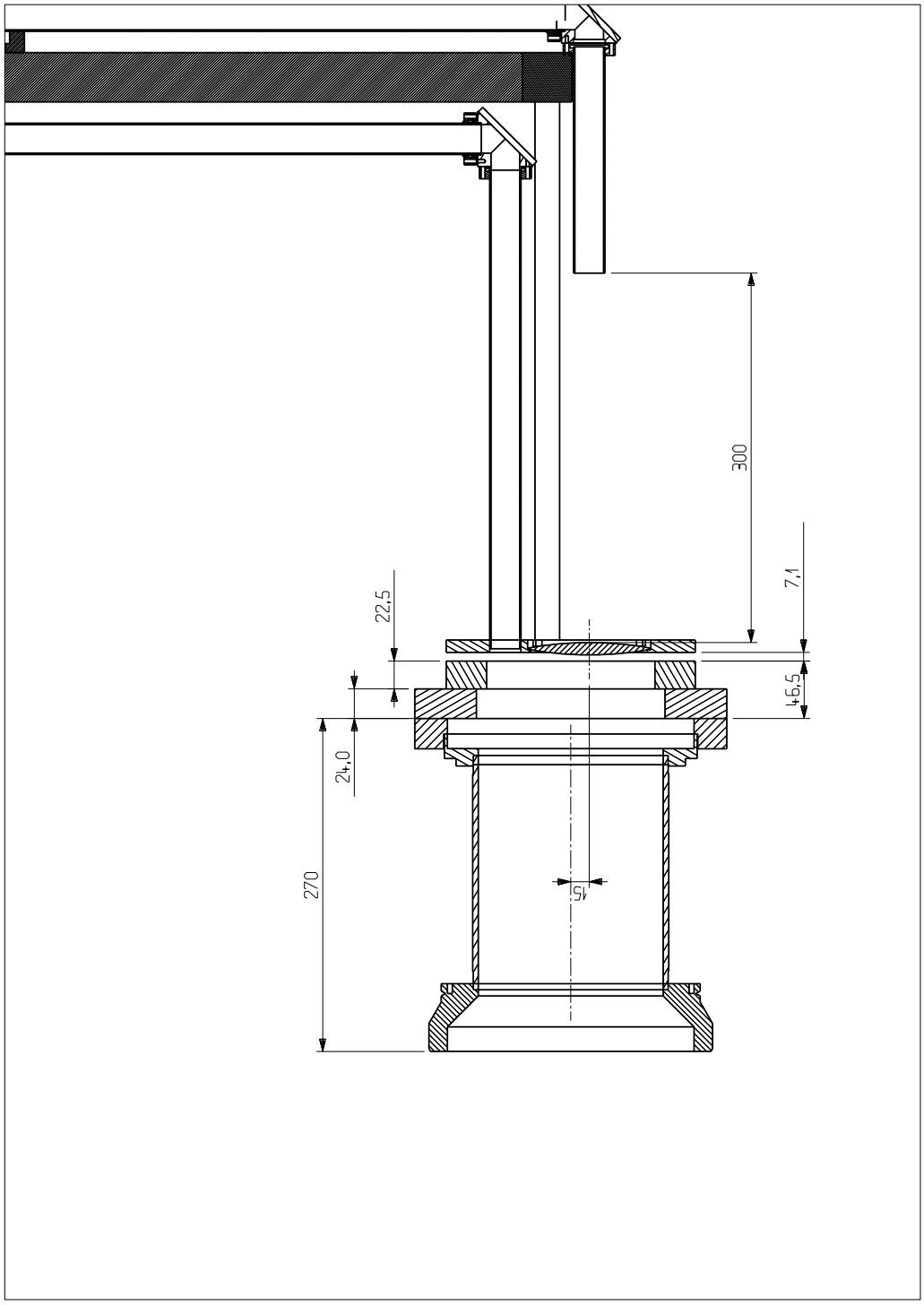

Figure C.2: *Vacuum window, lens and oversized waveguides for both Z=0 and Z=21 cm lines.*

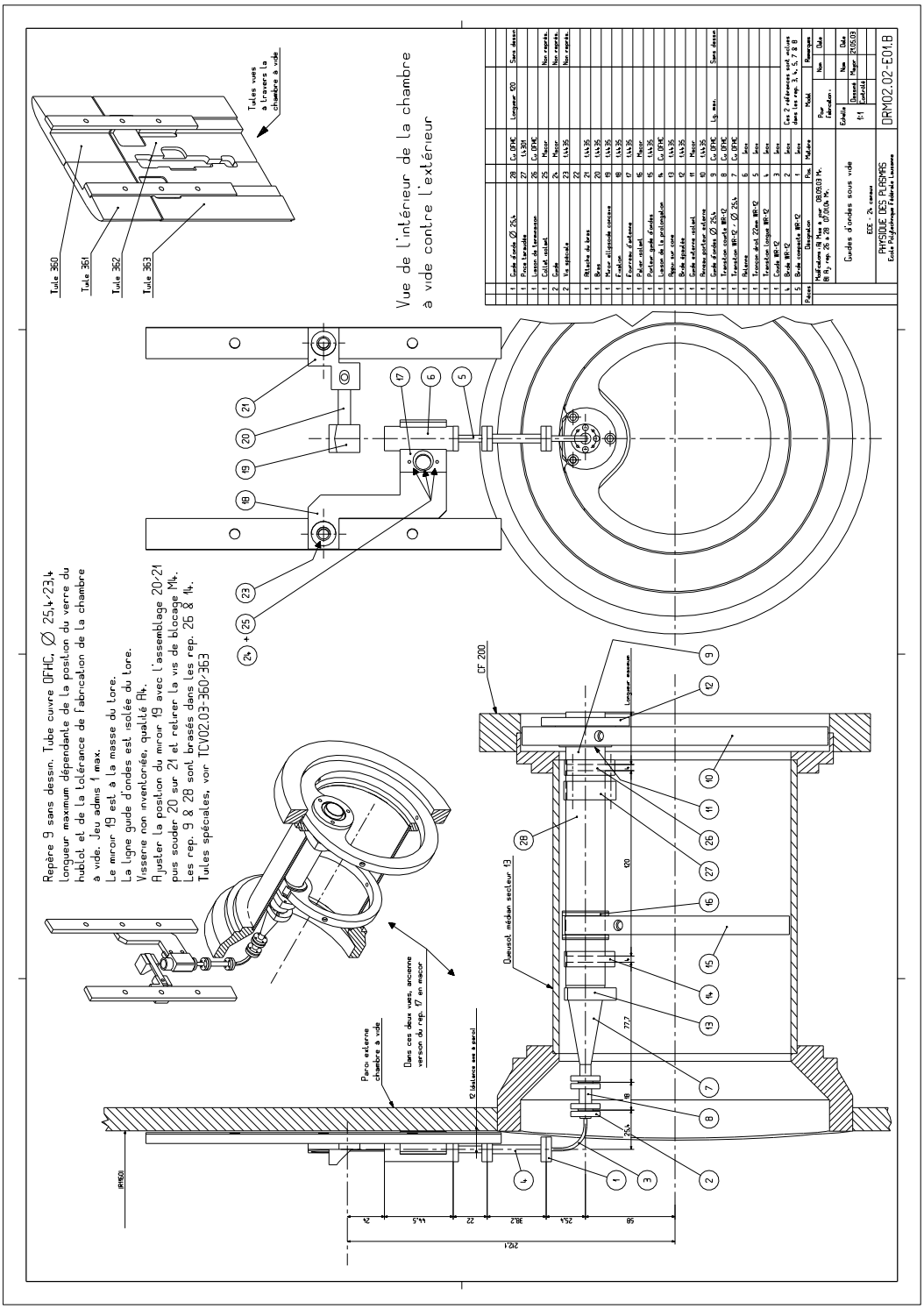

Figure C.3: *In-vessel part of the Z=21 cm line.*

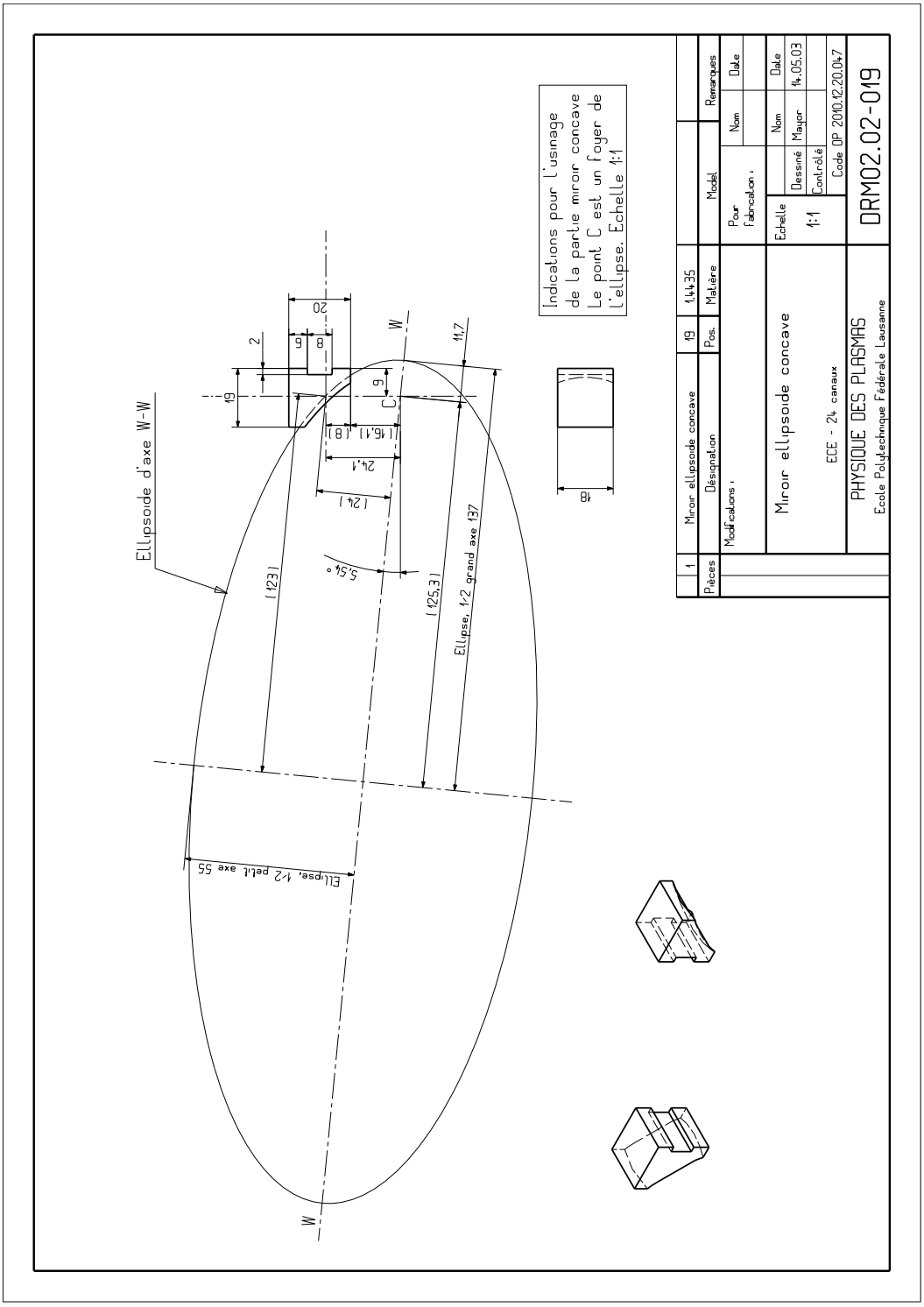

Figure C.4: *Elliptical mirror used in the Z=21 cm line.*

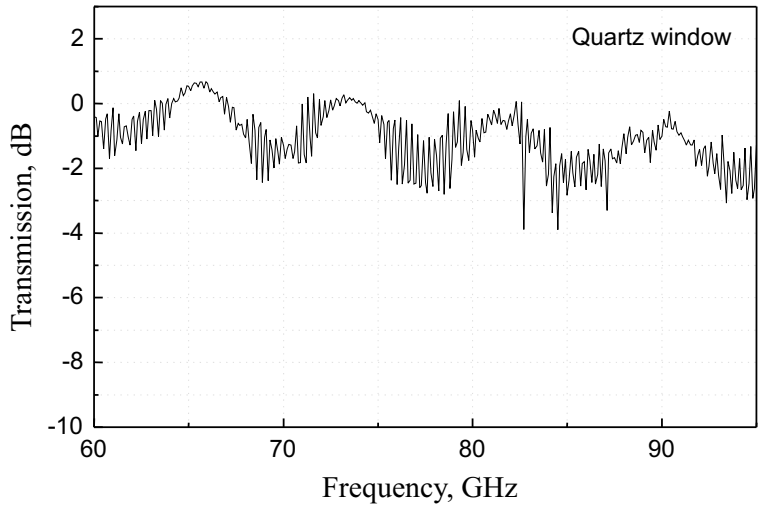

Figure C.5: *Measured transmission of the vacuum window.*

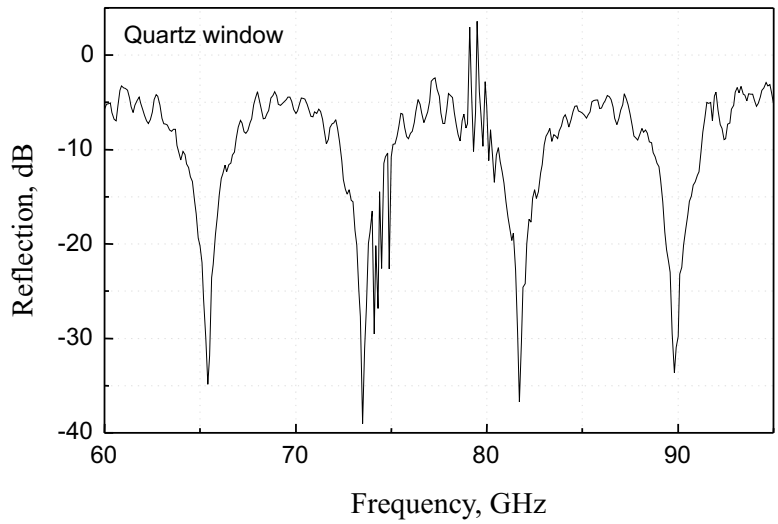

Figure C.6: *Measured reflection of the vacuum window.*

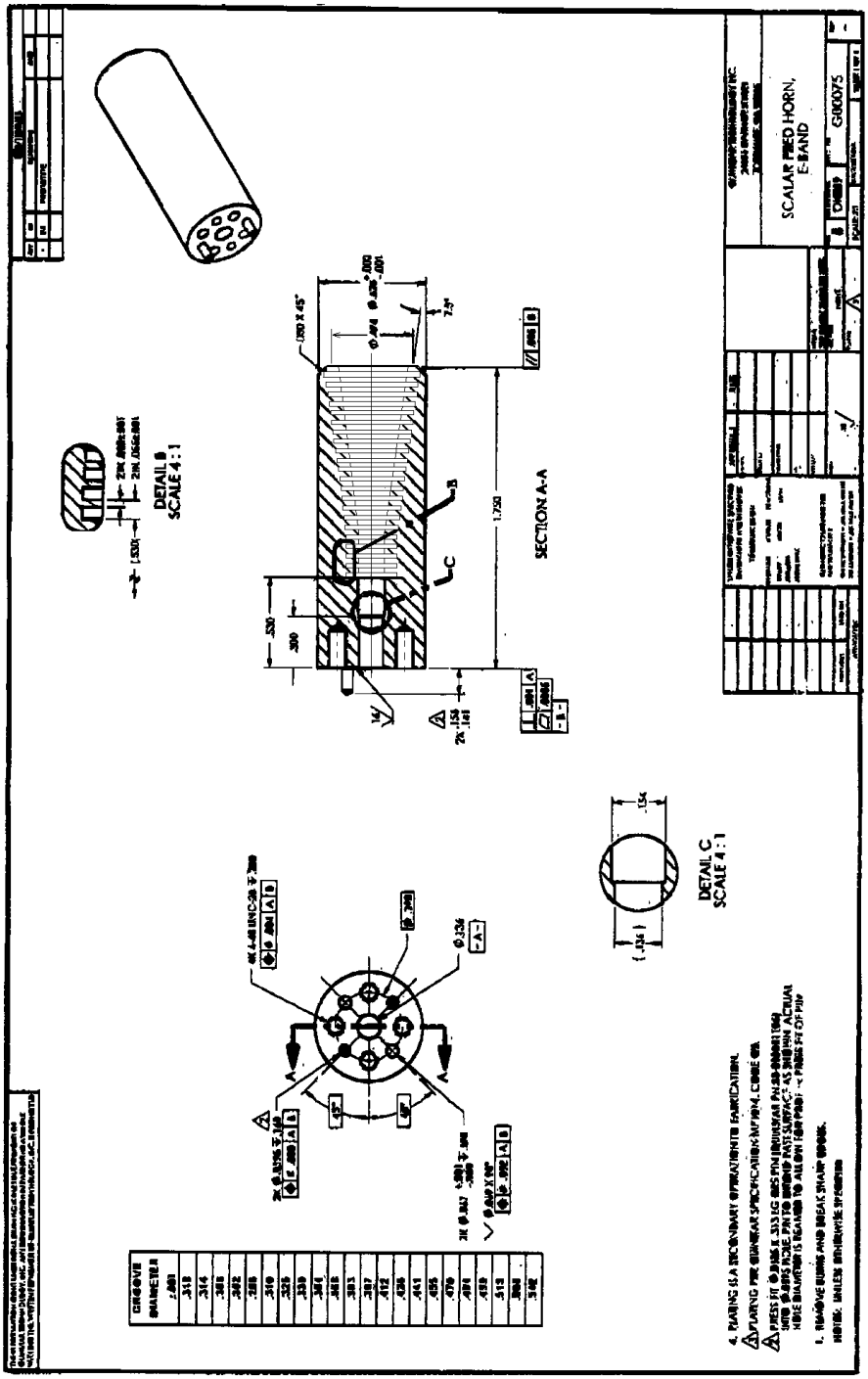

Figure C.7: *Scalar feed horn design.*

Appendix D

Plasma parameters related to magnetic reconnection

In table D.1 one can find typical plasma parameters and characteristic electric fields for the ohmic plasma on TCV (low density) compared to typical numbers for reconnection experiments, terrestrial magnetosphere and solar corona ([43]).

Table D.1: *Typical plasma parameters and characteristic electric fields.*

Parameter	TCV tokamak	Reconnection experiments	Terrestrial magnetosphere	Solar corona
L_e, m	0.25	10^{-1}	10^{7}	10^{8}
n_e, m^{-3}	10^{19}	10^{20}	10^{5}	10^{15}
T, K	10^{7}	10^{5}	10^{7}	10^{6}
B, T	1.5	10^{-1}	10^{-8}	10^{-2}
λ_D, m	10^{-4}	10^{-6}	10^{3}	10^{-3}
R_{gi}, m	$2 \cdot 10^{-3}$	10^{-3}	10^{5}	10^{-1}
λ_i, m	10^{-1}	10^{-2}	10^{6}	10^{1}
$ln\Lambda$	17	11	33	19
λ_{mfp}, m	10^{3}	10^{-2}	10^{16}	10^{4}
β	10^{-3}	10^{-2}	10^{-1}	10^{-4}
$L_u(\approx R_m)$	10^{7}	10^{3}	10^{14}	10^{14}
E_D, V/m	10^{1}	10^{3}	10^{-13}	10^{-2}
$E_A(= v_A B)$, V/m	10^{3}	10^{4}	10^{-2}	10^{5}
$E_{SP}(= E_A/\sqrt{R_{me}})$, V/m	10^{1}	10^{2}	10^{-9}	10^{-3}

The global plasma parameters here: L_e is the size of the plasma, n_e is the plasma density, T is the plasma temperature, B is the magnetic field. Following parameters can be calculated using the plasma global parameters: the Debye length λ_D, the ion gyro radius R_{gi}, the ion inertial length λ_i, the Coulomb logarithm $ln\Lambda$, the mean free path for electron-ion collisions λ_{mfp}, the plasma beta β, the Lundquist number L_u. The following fields are widely used in reconnection theory: the Dreiser electric field E_D, the convective electric field based on the Alfvén speed E_A, the Sweet-Parker electric field E_{SP}.

Appendix E

Relaxation times for a test electron in plasma

There are two basic types of collisions for electrons in fully ionized plasmas: electron-electron collisions (e-e) and electron-ion collisions (e-i). We consider three basic processes experienced by the test electron e passing through the field particles β (β denotes either electrons (e) or ions (i)): the momentum transfer, the particle deflection and the energy exchange [62]. Each process can be characterized by a relaxation time: τ_s, τ_d and τ_ϵ:

$$\tau_s^\beta = \frac{\tau_1^\beta}{\left(1 + \frac{m_e}{m_\beta}\right)\mu(x_\beta)},$$

$$\tau_d^\beta = \frac{\tau_1^\beta}{2\left(\mu(x_\beta) + \mu'(x_\beta) - \dfrac{\mu(x_\beta)}{2x_\beta}\right)},$$

$$\tau_\epsilon^\beta = \frac{\tau_1^\beta}{4\mu(x_\beta)/x_\beta},$$

where x_β is square of dimensionless velocity:

$$x_\beta = \frac{m_\beta v^2}{2T_\beta} = \frac{m_\beta}{m_e} \cdot \frac{\epsilon_e}{T_\beta},$$

$\mu(x_\beta)$ - Maxwell integral:

$$\mu(x_\beta) = \frac{2}{\sqrt{\pi}} \int_0^{x_\beta} e^{-t}\sqrt{t}dt,$$

and τ_1^β:

$$\tau_1^\beta = \frac{\sqrt{m_e}}{\pi\sqrt{2}e^2 e_\beta^2} \cdot \frac{\epsilon_e^{3/2}}{n_\beta ln\Lambda}.$$

The total relaxation time can be calculated as follows:

$$\frac{1}{\tau} = \frac{1}{\tau^e} + \frac{1}{\tau^i}$$

The formulas for the relaxation times are written in the CGS unit system.

In fig.E.1 the relaxation times calculated for the pure plasma (single charged ions) are plotted. For electrons moving with a velocity much higher than the mean thermal velocity, the "partial" relaxation times for the deflection are approximately equal for the $e-e$ and the $e-i$ collisions. The $e-e$ relaxation time is twice shorter than the $e-i$ one for the momentum transfer. The energy exchange due to the $e-e$ collisions is m_i/m_e times faster than due to the $e-i$ collisions, or in other words $e-i$ collisions are negligible in this context.

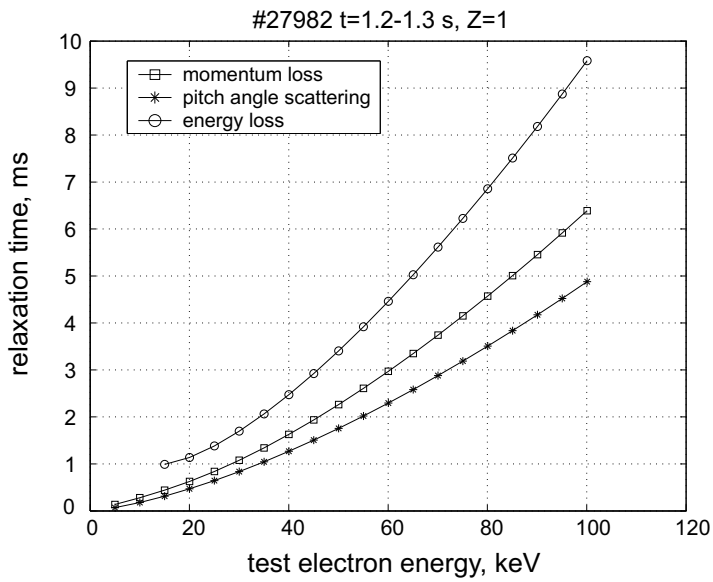

Figure E.1: *The relaxation times for the test electron ($Z_{eff} = 1$).*

In fig.E.2 the relaxation times for the plasma with impurities ($Z_{eff} = 4$) are shown. In this case $e-i$ collisions become more important than $e-e$ collisions for the momentum loss and the deflection. However, for the energy loss $e-i$ collisions are still negligible compared to the $e-e$ collisions ($m_i/m_e >> Z_{eff}^2$).

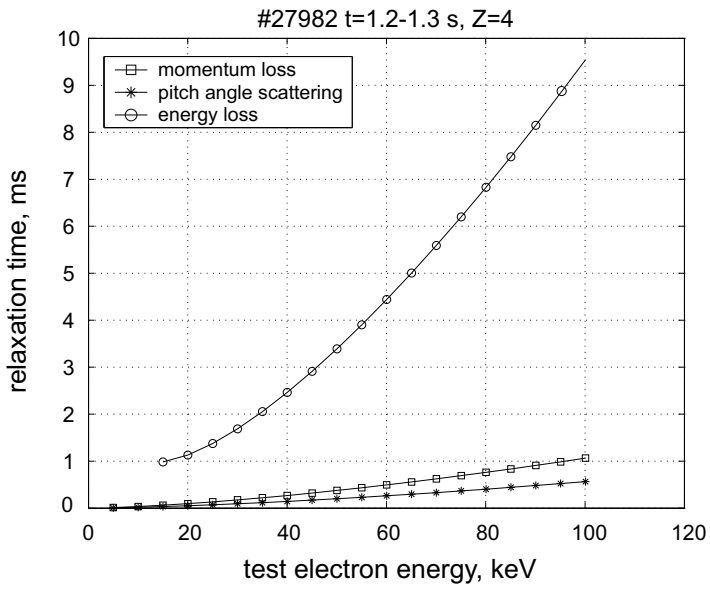

Figure E.2: *The relaxation times for the test electron ($Z_{eff} = 4$).*

Bibliography

[1] F.F. Chen. *Introduction to Plasma Physics.* Plenum Press, New York, 1974.

[2] J. Wesson. *Tokamaks.* Clarendon Press - Oxford, 2004.

[3] Y. Peysson, S. Coda, and F. Imbeaux. Hard X-ray CdTe tomography of tokamak fusion plasmas. *Nucl. Instrum. and Methods in Phys. Res.*, **458**(1):269, 2001.

[4] P. Blanchard, S. Alberti, S. Coda, H. Weisen, P. Nikkola, and I. Klimanov. High field side measurements of non-thermal electron cyclotron emission on TCV plasmas with ECH and ECCD. *Plasma Phys. Control. Fusion*, **44**(10):2231, 2002.

[5] F. Hoffman and G. Tonetti. Tokamak equilibrium reconstruction using Faraday rotation measurements. *Nucl. Fusion*, **28**:1871, 1988.

[6] T.P. Goodman, S. Alberti, M.A. Henderson, A. Pochelon, and M.Q. Tran. Design and installation of the electron cyclotron wave system for the TCV tokamak. *Proc. 19th Symposium on Fusion Technology, Lisbon, Portugal*, page 565, 1996.

[7] S. Alberti et al. European high-power CW gyrotron development for ECRH systems. *Fusion Engineering and Design*, **53**:387, 2001.

[8] J.-P. Hogge, S. Alberti, L. Porte, and G. Arnoux. Preliminary results of top launch third harmonic X-mode electron cyclotron heating in the TCV tokamak. *Nucl. Fusion*, **43**:1353, 2003.

[9] T. H. Stix. *The theory of plasma waves.* New York: McGraw-Hill, 1962.

[10] M. Brambilla. *Kinetic theory of plasma waves. Homogeneous plasmas.* Oxford University Press, 1998.

[11] G. Evans and C.W. McLeish. *RF radiometer handbook*. Artech house, Inc., 1977.

[12] H.J. Hartfuss, T. Geist, and M. Hirsch. Heterodyne methods in millimetre wave plasma diagnostics with applications to ECE, interferometry and reflectometry. *Plasma Phys. Control. Fusion*, **39**(11):1693, 1997.

[13] M. Bornatici, R. Cano, O. De Barbieri, and F. Engelmann. Electron cyclotron emission and absorption in fusion plasmas. *Nucl. Fusion*, **23**(9):1153, 1983.

[14] K. Chang. *Microwave Passive and Antenna Components*. Wiley Interscience, John Wiely & Sons, Inc., 1989.

[15] K. Uchino, D.V. Bartlett, A.E. Costley, and N.A. Salmon. A relative calibration method for the JET ECE heterodyne radiometer. *Proc. 7th Workshop on ECE and ECR-Heating, China (1989)*.

[16] S.V. Mirnov and I.B. Semenov. Investigation of the instabilities of the plasma string in the Tokamak-3 system by means of correlation method. *Soviet Atomic Energy*, **30**:22, 1971.

[17] I. Furno, C. Angioni, F. Porcelli, H. Weisen, R. Behn, T.P. Goodman, M.A. Henderson, Z.A. Pietrzyk, A. Pochelon, H. Reimerdes, and E. Rossi. Understanding sawtooth activity during intense electron cyclotron heating experiments on TCV. *Nucl. Fusion*, **41**:403, 2001.

[18] H.P. Laqua, H.J. Hartfuss, and W7-AS Team. Electron Bernstein Wave Emission from an Overdense Plasma at the W7-AS Stellarator. *Phys. Rev. Lett.*, **81**(10):2060, 1998.

[19] A. Mueck, H.P. Laqua, S. Coda, B. Duval, T.P. Goodman, I. Klimanov, Y. Martin, A. Pochelon, and L. Porte. O-X-B mode conversion in the TCV tokamak. In *Proc. of the 32th EPS conference on Plasma Phys. and Contr. Fusion, Vol. 29C*, Tarragona, Spain, 2005.

[20] A. Mueck, H.P. Laqua, S. Coda, B. Duval, T.P. Goodman, I. Klimanov, Y. Martin, A. Pochelon, and L. Porte. Electron Bernstein wave heating in the TCV tokamak. In *Bulletin of the APS, 47th annual meeting of the division of plasma physics, Vol. 50, No. 8*, page 126, Denver, Colorado, 2005.

[21] S. Preische, P.C. Efthimion, and S.M. Kaye. Oblique electron cyclotron emission for electron distribution studies. *Rev. Sci. Instrum.*, **68**(1):409, 1997.

[22] O. Tudisco, E. de la Luna, V. Krivensky, G. Giruzzi, P. Amadeo, A. Bruschi, F. Gandini, G. Granucci, V. Muzzini, A. Simonetto, FTU, and ECRH Group. Oblique ECE measurements during strong ECH at 140 GHz in FTU. In *Proc. 28th EPS conference on Plasma Phys. and Contr. Fusion*, page 1221, Funchal, Portugal, 2001.

[23] F. Volpe. Electron Bernstein emission diagnostic of electron temperature profile at W7-AS stellarator. *PhD thesis, IPP Garching and Greifswald, IPP Report 13/1*, 2003.

[24] K. Matsuda et al. Ray tracing study of electron cyclotron current drive in DIII-D using 60 GHz. *IEEE Transactions on Plasma Science*, **17**(1):6, 1989.

[25] G. Wentzel. Eine Verallgemeinerung der Quantenbedingungen fur die Zwecke der Wellenmechanik. *Zeits. f. Physik*, **38**:518, 1926.

[26] H. A. Kramers. Wellenmechanik und halbzahlige Quantisierung. *Zeits. f. Physik*, **39**:828, 1926.

[27] L. Brillouin. La mecanique ondulatoire de Schrodinger, une methode generale de resolution par approximations successives. *Comptes Rendus Acad.Sci.*, **183**:24, 1926.

[28] A. Einstein. Zur Quantumtheorie der Strahlung. *Phys. Zeit.*, **18**:121, 1917.

[29] G. Bekefi. *Radiation Processes in Plasmas.* John Wiely & Sons, Inc., 1966.

[30] M. Bornatici, F. Engelmann, C. Maroli, and V. Petrillo. Propagation and absorption of the exraordinary mode at frequencies around the second harmonic of the electron cyclotron frequency in a high density plasma. *Plasma Phys.*, **23**:89, 1981.

[31] Y.N. Dnestrovsky, D.P. Kostomarov, and N.V. Skrydlov. *Soviet physics. Technical physics*, (8):691, 1964.

[32] I. Weiss. Electromagnetic wave propagation in relativistic magnetized plasmas. *Journ. Comp. Phys.*, **61**:403, 1985.

[33] E. Nelson-Melby, S. Alberti, T. Goodman, M. Henderson, and P. Nikkola. A comparison of weakly relativistic electron cyclotron wave damping in the presence of high energy electrons. *Proc. 30th EPS Conference on Contr. Fusion and Plasma Phys., St.-Peterburg (2003).*

[34] S. Weinberg. Eikonal method in magnetohydrodynamics. *Phys. Rev.*, **126**:1899, 1962.

[35] R.W. Harvey and M.G. McCoy. In *Proc. IAEA TCM/Advances in Simulation and modeling in Thermonuclear Plasmas*, Montreal, Canada, 1992.

[36] F. Wagner et al. Regime of improved confinement and high beta in neutral beam heated divertor discharges in the ASDEX tokamak. *Phys. Rev. Lett.*, **49**(19):1408, 1982.

[37] T.N. Carlstorm. Transition physics and scaling overview. *Plasma Phys. Control. Fusion*, **38**(8):1149, 1996.

[38] Y.R. Martin, M.A. Henderson, et al. Accessibility and properties of ELMy H-mode and ITB plasmas in TCV. *Plasma Phys. Control. Fusion*, **45**(9):A351, 2003.

[39] J.W. Connor, T. Fukuda, X. Garbet, C. Gormezano, V. Mukhovatov, M. Wakatani, the ITB Database Group, the ITPA Topical Group on Transport, and Internal Barrier Physics. A review of internal transport barrier physics for steady-state operation of tokamaks. *Nucl. Fusion*, **44**:R1, 2004.

[40] R.C. Wolf. Internal transport barriers in tokamak plasmas. *Plasma Phys. Control. Fusion*, **45**:R1, 2003.

[41] M.A. Henderson, Y. Camenen, S. Coda, T.P. Goodman, P. Nikkola, A. Pochelon, O. Sauter, and TCV team. Rapid and localized electron internal-transport-barrier formation during shear inversion in fully non-inductive TCV discharges. *Phys. Rev. Lett.*, **93**(21):215001, 2004.

[42] S. Coda, S. Alberti, P. Blanchard, T.P. Goodman, M.A. Henderson, P. Nikkola, Y. Peysson, and O. Sauter. Electron cyclotron current drive and suprathermal electron dynamics in the TCV tokamak. *Nucl. Fusion*, **43**:1361, 2003.

[43] E. Priest and T. Forbes. *Magnetic reconnection: MHD Theory and applications.* Cambridge University Press, 2000.

[44] D. Biskamp. *Magnetic reconnection in plasmas.* Cambridge University Press, 2000.

[45] P.A. Sweet. The neutral point theory of solar flares. In *Electromagnetic Phenomena in Cosmical Physics*, page 123, IAU Symp.6, ed. B.Lehnert (Cambridge Univ. Press, London), 1958.

[46] P.A. Sweet. The production of the high energy particles in solar flares. *Nuovo Cimento Suppl.*, **8**, Ser. X:188, 1958.

[47] E.N. Parker. Sweet's mechanism for merging magnetic field lines in conducting fluids. *J. Geophys. Res.*, **62**:509, 1957.

[48] E.N. Parker. The solar flare phenomenon and theory of reconnection and annihilation of magnetic fields. *Astrophys. J. Supp.*, **8**:177, 1963.

[49] H. Dreicer. Electron and ion runaway in a fully ionized gas. I. *Phys. Rev.*, **115**(2):238, 1959.

[50] H. Dreicer. Electron and ion runaway in a fully ionized gas. II. *Phys. Rev.*, **117**(2):329, 1960.

[51] S. von Goeler, W. Stodiek, and N. Sauthoff. Studies of internal disruptions and m=1 oscillations in tokamak discharges with soft x-ray techniques. *Phys. Rev. Lett.*, **33**:1201, 1974.

[52] B.B. Kadomtsev. Disruptive instability in tokamaks. *Sov. J. Plasma Phys.*, **1**:389, 1975.

[53] D. Biskamp. *Nonlinear magnetohydrodynamics.* Cambridge University Press, 1993.

[54] W.J. Goedheer and E. Westerhof. Sawtooth, transport and cyclotron heating in T-10. *Nucl. Fusion*, **28**:565, 1988.

[55] J.A. Wesson. Sawtooth reconnection. *Nucl. Fusion*, **30**:2545, 1990.

[56] G. Fussman, W. Engelhardt, W. Feneberg, J. Gernhardt, E. Glock, F. Karger, S. Sesnic, and H.P. Zehrfeld. Investigation of modulated runaway losses and effects of a helical dipole field in Pulsator. In *Proc. 7th Conf. on Plas. Phys. & Contr. Nucl. Fus. Res.*, page 401, Innsbruck, Vienna, 1978.

[57] P.V. Savrukhin. Generation of suprathermal electrons during magnetic reconnection at the sawtooth crash and disruption instability in the T-10 tokamak. *Phys. Rev. Lett.*, **86**:3036, 2001.

[58] P.V. Savrukhin and I.V. Klimanov. Tangential x-ray imaging system for analysis of the small-scale modes in the T-10 tokamak. *Rev. Sci. Instrum.*, **72**:1668, 2001.

[59] Y. Peysson. Transport of fast electrons during LHCD in TS, JET and ASDEX. *Plasma Phys. Control. Fusion*, **35**:B253, 1993.

[60] V.S. Udintsev, M.J. van de Pol, A.J.H. Donné, J.W. Oosterbeek, and A. Kraemer-Flecken. New ECE diagnostics for the TEXTOR-94 tokamak. *Rev. Sci. Instrum.*, **72**:359, 2001.

[61] V.S. Udintsev, M. Goniche, G. Giruzzi, G.T.A. Huysmans, F. Imbeaux, P. Maget, X. Garbet, R. Sabot, J.L. Segui, F. Turco, T.P. Goodman, D. Molina, H. Weisen, and the Tore Supra team. Studies of high frequency hot ion instabilities by means of correlation ECE on Tore Supra. *Plasma Phys. Control. Fusion*, **48**:accepted, 2006.

[62] B.A. Trubnikov. *Reviews of plasma physics,* **1***: Particle interactions in a fully ionized plasma.* Consultants Bureau - New York, 1965.

Acknowledgments

First, I have to thank my thesis supervisor Prof. Ambrogio Fasoli. He has always been available and willing to help, despite the great amount of work that does here in Lausanne, but also in Oxford (JET) and Boston (MIT).

I am very grateful to Patrick Blanchard, Rysard Narkovic, Stefano Alberti and Laurie Porte, who helped me with microwave theory and techniques, which were new for me.

I deeply appreciate discussions with Tim Goodman and Stefano Coda, and their help with experiments.

The technical part of this thesis could not be done without help of many people. First I would like to thank people from the construction office, who were not only very efficient, but also very nice: head of the office Rene Chavan, designers Jean-Claude Magnin and Jean-Michel Mayor, technicians Claude Raggi (he always made me smile), Roger Niklaus, Jean-Pierre Baertschi, Francois Besancon, Robert Lasseur, Pierluigi Pagnoni, William Matthey-Doret and Andre Dubrit.

I am also indebted to Damien Fasel and Jean-Francois Mion from the electricity department of CRPP. A significant part of the work was related to the electronics. I appreciate the work done by Philippe Marmillod, Blaise Marletaz and Pierre Lavanchy and the lessons they taught me.

I am grateful to Xavier Llobet, Pierre-Francois Isoz and Pierre Etienne who always solved very quickly all problems related to IT.

I would like to thank Bernard Joye, Pascal Conti and Omar Bartolomeoli, who are responsible for vacuum on TCV. Their support made possible oblique ECE experiments.

For help with all things administrative, I want to thank our secretaries Edith Grueter and Paula Halter, as well as our financial director Pierre Paris.

I am very grateful to our director Minh Quang Tran, deputy director Kurt Appert and Henri Weisen for the opportunity to work in CRPP.

I want to thank my friends in CRPP Andrei Martynov, Pavel Popovich, Alexei Zabolotsky and Ilya Pavlov, my officemates Beat Schaerz, Edgar Scavino and Paolo Angelino, and all the young people in CRPP, who created a unique environment for working and living in Lausanne.

Last, but not least. I always felt support from Moscow. I want to thank all my family, especially my mother Galina and my best friend Alexei.

Thanks again!

KLIMANOV Igor

Nationalité : Russe
Etat civil : Célibataire
Né le 19 août 1977

CRPP-EPFL, Bâtiment PPB,
1015 Lausanne
Téléphone : +41 21 693.65.36
E-mail : igor.klimanov@epfl.ch

Formation

2001 - 2005	**Ecole Polytechnique Fédérale de Lausanne (EPFL)** **Lausanne, Suisse** **Doctorat** - *"Reconstruction of the electron distribution function during ECRH/ECCD and magnetic reconnection events in a tokamak plasma"*, Directeur de thèse Prof. A. Fasoli.
1994 - 2000	**Institut National d'Ingénerie et de Physique** **Moscou, Russie** **Diplôme** d'ingénieur physicien - *"Small-scale perturbations in the T-10 tokamak plasma"*, Responsable Dr. P. Savrukhin
1984 - 1994	Ecole primaire et secondaire N 820, Moscou, Russie Certificat d'études secondaires

Expérience

1998 - 2000	Centre Scientifique Russe **"Institut Kourtchatov"** **Moscou, Russie** Ingénieur

Récompenses

2000	Vainqueur du concours de jeunes scientifiques du ministere de la Science de Russie (le plasma et la fusion thermonucleaire)
2000	Laureat de prix annuel pour le meilleur travail des jeunes scientifiques, Centre Scientifique Russe "Institut Kourtchatov"
1999	Laureat de prix annuel " Soros Student " (Programme International de la Science et de l'Education de Soros).

Publications

[1] **I. Klimanov** et al., "ECE spectrometry on TCV". Review of Scientific Instruments 76, 093504 (2005)

[2] G Zhuang, et al.(including **I. Klimanov**), "Influence of non-Maxwellian velocity distributions during ECRH and ECCD on electron temperature measurements by Thomson scattering", 1539, Vol. 47, Plasma Physics and Controlled Fusion (2005)

[3] P. Blanchard et al.(including **I. Klimanov**), "High field side measurements of non-thermal electron cyclotron emission on TCV plasmas with electron cyclotron heating ", 2231, Vol. 44, Plasma Physics and Controlled Fusion (2002)

[4] D.A. Kislov et al. (including **I. Klimanov**), "Beta limits due to resistive tearing modes in T-10", 1619, Vol. 41, Nuclear Fusion (2001)

[5] P.V. Savrukhin and **I.V. Klimanov**, "Tangential x-ray system for analysis of the small-scale modes in the T-10 tokamak", 1668, Vol. 72(3), Review of Scientific Instruments (2001)

[6] P.V. Savrukhin et al. (including **I. Klimanov**), "Toroidal cartography of the high-m magnetic islands in tokamak plasma", 591, Vol. 70(1), Review of Scientific Instruments (1999)

[7] T.P. Goodman et al. (including **I. Klimanov**), "Safety factor profile requirements for electron ITB formation in TCV", B107, Vol. 47(12B), Plasma Physics and Controlled Fusion (2005)

[8] T.P. Goodman et al. (including **I. Klimanov**), "An overview of results from the TCV tokamak", 1619, Vol. 43(12), Nuclear Fusion (2003)

[9] Y.R. Martin et al. (including **I. Klimanov**), "Accessibility and properties of ELMy H-mode and ITB plasmas in TCV", A351, Vol. 45(12A), Plasma Physics and Controlled Fusion (2003)

[10] J.-M. Moret et al. (including **I. Klimanov**), "ECH physics and new operational regimes on TCV", B85, Vol. 44(12B), Plasma Physics and Controlled Fusion (2002)

[11] F. Hoffman et al. (including **I. Klimanov**), "Stability and energy confinement of highly elongated plasmas in TCV", A161, Vol. 43(12A),Plasma Physics and Controlled Fusion (2001)

Conférences

2005	American Physical Society Annual Meeting of the Division of the Plasma Physics, **Denver, Colorado**
2003	American Physical Society Annual Meeting of the Division of the Plasma Physics, **Albuquerque, New Mexico**
2002	European Physical Society Conference on Plasma Physics and Controlled Fusion, **Montreux, Switzerland**
2000	European Physical Society Conference on Plasma Physics and Controlled Fusion, **Budapest, Hungary**